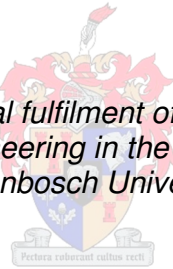# Design, Manufacture and Hydrodynamic Evaluation of a Prototype Trileaflet Mechanical Heart Valve for Aortic Valve Replacement

by
Elsmari Wium

Thesis presented in partial fulfilment of the requirements for the degree of Master of Engineering in the Faculty of Engineering at Stellenbosch University

Supervisor: Dr Jacobus H. Müller
Co-supervisor: Prof. Chris J. Meyer and Prof. Francis E. Smit

April 2020

DECLARATION

By submitting this thesis electronically, I declare that the entirety of the work contained therein is my own, original work, that I am the sole author thereof (save to the extent explicitly otherwise stated), that reproduction and publication thereof by Stellenbosch University will not infringe any third party rights and that I have not previously in its entirety or in part submitted it for obtaining any qualification.

Date: April 2020

ABSTRACT

A rigid trileaflet heart valve for aortic valve replacement was designed and prototypes were developed for testing purposes. Due to the prevalence of rheumatic heart disease in developing countries, a need for a mechanical heart valve replacement that does not elicit a negative biological response exists. Tests were conducted to evaluate the hydrodynamic performance of the valve and to compare the results to that of a commercial bileaflet valve. The aim was to determine whether the prototype valve displays an enhanced performance.

Design concepts were generated following a systematic approach. Concepts were evaluated analytically, and feasible concepts were developed using additive manufacturing techniques, well-knowing the limitations of this technology. Initial prototypes were subjected to a preliminary numerical and experimental assessment to determine whether the functional, material and manufacturing requirements are satisfied. Based on the outcome of the requirements evaluation, four trileaflet valve designs were selected for further investigation. Further investigation was required to determine whether the valves satisfy the performance requirements governed by regulatory bodies. Investigations included experimental and numerical evaluations of the trileaflet valves, a benchmark bileaflet valve and a commercial valve. The benchmark bileaflet valve, based on an existing commercial valve design, was manufactured using the same technique as the trileaflet valves, facilitating direct performance comparisons.

Flow tests, using a pulse duplicator, and motion analysis tests, using a high-speed camera, were conducted. Flow test measurements were analysed to calculate standard heart valve performance parameters. Three of the four trileaflet valves exhibited a performance comparable to or exceeding that of the bileaflet valve. The additive manufactured valves behaved similar to the commercial valve. The high-speed images were analysed to calculate valve opening and closing times and leaflet velocities. Cycle-to-cycle variation, leaflet flutter, incomplete opening and asynchronous leaflet motion were observed. Considering asymmetries and variations, the trileaflet valves showed comparable closing times to the bileaflet valve, with one valve showing a distinct improvement. However, the trileaflet valve profile height contributed to corresponding leaflet tip linear velocities between the bileaflet and trileaflet valves.

Steady state conditions were initially assumed for the numerical evaluation. The comparative study between trileaflet and bileaflet valves was extended and the effect of design variables was investigated. The results were used to formulate design recommendations and concurred that the valve identified in the experimental evaluation presented the best solution.

The recorded leaflet motion was specified as input to an unsteady computational evaluation. A high-fidelity transient model enables a more detailed analysis of the three-dimensional flow field. There was good comparison to the experimental results and to some published results. However, the results showed the development of high shear stresses in some areas, inducing coagulation and haemolysis.

A prosthetic heart valve design, evaluation and optimisation method was developed. The study demonstrated the feasibility of the concept but highlighted critical design and manufacturing aspects that require additional consideration. It also showed that prescribed kinematics computational fluid dynamics analyses offer an alternative solution for capturing asymmetrical valve and flow behaviour, without the computational expense of direct numerical simulations.

UITTREKSEL

'n Rigiede drie-seil hartklep vir aortaklepvervanging is ontwerp en prototipes is vir toetsdoeleindes geproduseer. As gevolg van die hoë voorkoms van rheumatiese hartsiekte in ontwikkelende lande, is daar 'n behoefte vir 'n kunshartklep met 'n gunstige biologiese werking. Verskeie toetse is uitgevoer om die hidrodinamiese werking van hierdie klep met 'n kommersiële twee-seilklep te vergelyk.

Nadat 'n sistematiese benadering gevolg is, is verskeie ontwerpskonsepte geproduseer. Hierdie konsepte was analities geëvalueer en uitvoerbare ontwerpe is met laagvervaardiging, met al sy beperkings in ag geneem, ontwikkel. Die inisiële prototipes is aan voorlopige numeriese en eksperimentele toetse onderwerp om te bevestig of die voorgestelde hartklep aan die funksionele, materiaal en vervaardiging vereistes voldoen. Vier drie-seil hartkleppe is, gebaseer op die uitkoms van die evaluering van vereistes, vir verdere toetse geselekteer om te bepaal of hierdie kleppe aan regulatoriese prestasie-vereistes voldoen. Die daaropvolgende toetse van die prototipe drie-seil hartkleppe, in vergelyking met 'n twee-seilklep as standaard, vervaardig in dieselfde wyse as die toetskleppe, en 'n kommersiële klep, het eksperimentele en numeriese evaluasies ingesluit.

Vloeitoetse, deur gebruik te maak van 'n polsdupliseerder en bewegingsanalise-toetse, met die gebruik van 'n hoë-spoed kamera, is uitgevoer. Die metings van die vloeitoetse is geanaliseer om te bepaal of die kleppe aan die regulatoriese vereistes voldoen. Drie van die vier drie-seilkhartkleppe het vergelykbare of selfs 'n beter werking as die toets twee-seilhartklep, getoon. Die laagvervaardigde kleppe het bewys om dieselfde eienskappe as die kommersiële klep te hê. Die beelde van die hoë-spoed klepbeweging is gebruik om die openings - en sluitingstye en seil-snelhede te bereken. Siklus-tot-siklus variasie, seilfladder, onvolledige oopmaak en ongesinchroniseerde beweging is opgemerk. Met die asimmetrie van die klepseile en die groot siklusvariasie in ag genome, het die drie-seilkleppe vergelykbare, en die een klep selfs beter, sluitingstye as die twee-seilklep getoon. Alhoewel die drie-seilhartklep langer neem om te sluit, is die lineêre snelheid van die seilpunte, as gevolg van die klepprofiel-hoogte, vergelykbaar met die van die twee-seilklep.

Gestadigde vloeidinamiese simulasies is inisiëel uitgevoer. Die resultate van dié simulasies is gebruik om die vergelykbare studie tussen die drie-seilklep en twee-seilklep uit te brei en om die effek van ontwerpsveranderinge te evalueer. Die uitkoms van hierdie studie is gebruik om ontwerpsaanbevelings te maak. Die drie-seilklep, wat tydens die ekperimentele toetse as die bes ontwerpte klep geidentifiseer is, het ook positiewe numeriese gedrag getoon.

Die opnames van die seilbewegings is gebruik om insetvoorwaardes vir 'n transiënte simulasie te definieer. 'n Betroubare berekeningsvloeidinamika model laat 'n meer gedetaileerde analise van die driedimensionele vloeiveld toe. Die numeriese resultate is met die eksperimentele resultate en sekere gepubliseerde resultate vergelykbaar. Areas van hoë skuifspanning, wat stolling en hemolise veroorsaak, is waargeneem.

'n Kunshartklep ontwerps-, evaluerings- en optimaliseringsmetode is ontwikkel. Die studie het die haalbaarheid van die drie-seilklep konsep gedemonstreer, maar het ook kritiese ontwerp- en vervaardigingsaspekte, wat bykomend in ag geneem moet word, beklemtoon. Dit het ook aangedui dat voorgeskrewe-kinematika berekeningsvloeidinamika ontledings 'n alternatiewe oplossing bied om asimmetriese klep- en vloeigedrag vas te lê, sonder die berekeningskoste van direkte numeriese simulasies.

ACKNOWLEDGEMENTS

CONTENTS

LIST OF FIGURES

LIST OF TABLES

NOMENCLATURE

Abbreviations

ABS	Acrylonitrile butadiene styrene
AM	Additive manufacturing
bpm	Beats per minute
C1	Concept 1
C2	Concept 2
CFD	Computational fluid dynamics
CFL	Courant-Friedrichs-Lewy
CHPC	Centre for High Performance Computing
CNC	Computer numerical control
CO	Cardiac output
CPD	Cardiac pulse duplicator
CPU	Central processing unit
CRPM	Centre for Rapid Prototyping and Manufacturing
CT	Computed tomography
CUT	Central University of Technology
D	Diameter
DLP	Digital light processing
DMLS	Direct metal laser-sintering
DNS	Direct numerical simulation
DPH	Diamond pyramid hardness
EOA	Effective orifice area
Exp	Experiment
FDM	Fused deposition modelling
FEA	Finite element analysis
FEM	Finite element method
FMECA	Failure Modes, Effects and Criticality Analysis
fps	Frames per second
FSI	Fluid-structure interaction
HSV	High speed video
HVR	Heart valve replacement
HVS	Heart Valve Society

IB	InfiniBand
ISO	International Organization for Standardization
L	Length
LES	Large eddy simulation
LDV	Laser Doppler velocimetry
LTI	Low temperature isotropic
MAP	Mean arterial pressure
MSST	Maximum shear stress theory
No.	Number
PEEK	Polyether ether ketone
PIV	Particle image velocimetry
RAM	Random-access memory
RANS	Reynolds-averaged Navier-Stokes
RHD	Rheumatic heart disease
RMS	Root mean square
RNS	Reynolds normal stress
RSS	Reynolds shear stress
SJM	St. Jude Medical
SLA	Stereolithography
S/N	Stress / life
S/N	Serial number
SST	Shear stress transport
SU	Stellenbosch University
SV	Stroke volume
UFS	University of the Free State
US FDA	United States Food and Drug Administration
VIA	Viscoelastic impedance adapter
WSS	Wall shear stress
2D	Two-dimensional
3D	Three-dimensional

Symbols

I	Moment of inertia
i, j	Direction
k-ω	K-omega turbulence model
P	Pressure
q	Volumetric flow rate
R_{ij}	Reynolds stress tensor
T	Torque
t	Time
u	Instantaneous velocity
u'	Fluctuating velocity
$\bar{u}$	Average velocity
V	Volume
x	Displacement
x, y, z	Direction
y^+	Wall y^+ value
α	Angular acceleration
ρ	Density
τ	Shear stress
τ_{ij}	Viscous stress tensor
μ	Dynamic viscosity

1   INTRODUCTION

1.1   Background and Motivation

Prosthetic heart valves have been used since the 1960s to replace dysfunctional valves to prevent heart failure [1]. Despite design and material advancements, the performances of both categories of heart valve implants, namely mechanical and biological, are not equivalent to their native counterparts. Mechanical heart valve replacements (HVRs) are durable, but they carry a concomitant thromboembolic risk due to non-physiological flow patterns and the introduction of foreign materials to the human body. Mechanical HVR recipients must adhere to a carefully monitored lifelong anticoagulation regimen. The long-term use of coumarin anticoagulants is riddled with pitfalls, including lack of compliance, intensive monitoring and various medicine and food interactions resulting in either under- or overdosing. Complications related to under- and over-dosage are thrombo-embolism and bleeding respectively. Conversely, biological valves do not pose a thromboembolic risk due to a superior hydrodynamic performance, but they lack durability. A study was conducted over 20 years on 2 533 patients with either mechanical or biological HVRs [2]. The results showed similar outcomes for both valves and no significant difference in recipient survival rate. The differences were that mechanical valve recipients were exposed to a higher risk of anticoagulant-related haemorrhage and biological valve recipients were exposed to a higher risk of reoperation. Currently, an ideal HVR does not exist [3].

Rheumatic heart disease (RHD) is one of the major causes of heart valve damage that warrants HVR in South Africa and the rest of the developing world [4 – 6]. In developing countries, the management of anticoagulation is also challenging owing to the lack of appropriate facilities. Generally, patients who require HVR due to RHD are considerably younger than those who require HVR due to age-related degenerative heart valve disease [7]. The age of the recipient governs the valve's durability requirement. Younger patients (less than 65 years of age) require longer-lasting implants. Biological valves are not preferred in these cases. Bileaflet valves are the most commonly implanted mechanical HVRs [8]. These valves are durable and have an added cost benefit over biological valves; however, they pose a safety risk in the form of coagulation. Therefore, there is a need to design, manufacture and test a valve for younger patients that incorporates the durability associated with mechanical valves and possesses haemodynamic characteristics so that the need for anticoagulants is reduced or eliminated. The development of such a valve has the potential to improve the quality of life of thousands of people.

1.2   Research Aims

The goals of this study were as follows:

   i.   To investigate the complex interaction between heart valves and blood and to improve the understanding of the mechanisms of red blood cell injury and platelet activation in commercial bileaflet valves.
   ii. To design a mechanical HVR that improves on the hydrodynamic performance of commercial alternatives, using the knowledge gained in (i).

iii.   To manufacture a prototype valve for pilot experimental testing.

iv.   To evaluate the hydrodynamic performance of the prototype valve through experimental and computational methods.

v.   To compare the performance of the prototype valve to a benchmark bileaflet valve and to make recommendations for design improvements.

vi.   To support the Robert W. M. Frater Cardiovascular Research Centre's long-term vision of becoming a developer of prosthetic heart valves by contributing to and integrating existing capabilities and knowledge at the Department of Cardiothoracic Surgery at the University of the Free State (UFS), the Department of Mechanical and Mechatronic Engineering at Stellenbosch University (SU) and the Centre for Rapid Prototyping and Manufacturing (CRPM) at the Central University of Technology (CUT).

1.3   Overview

The layout of this report is shown schematically in Figure 1. The scope of the research project was limited to prototype development.
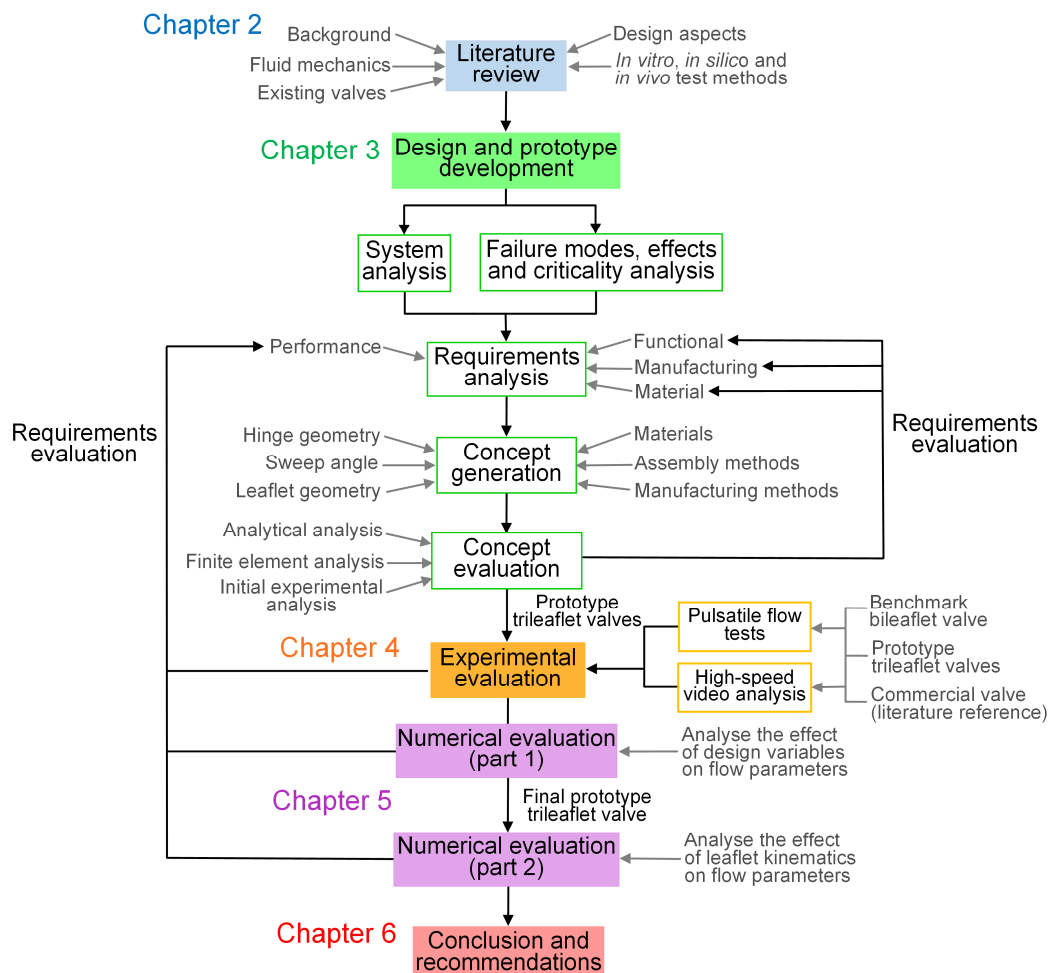
Figure 1:   Schematic overview of thesis

2 LITERATURE REVIEW

The following literature study offers a brief anatomical explanation of heart valves, the associated fluid mechanics, characteristics of existing HVRs and the principles of valve design and testing. The author's views are discussed in greater detail in [9].

2.1 Anatomy and Physiology

The heart has two atrioventricular valves and two semilunar valves that form an integral part of the circulatory system [10]. The atrioventricular valves regulate unidirectional blood flow from the atria to the ventricles during diastole, with the bicuspid valve on the right side of the heart and the tricuspid valve, or mitral valve, on the left. Similarly, the semilunar valves regulate unidirectional blood flow from the ventricles to either the lungs on the right side or to the rest of the body on the left during systole, with the pulmonary and aortic valves respectively. The valves are shown in Figure 2 (reproduced from [11]).
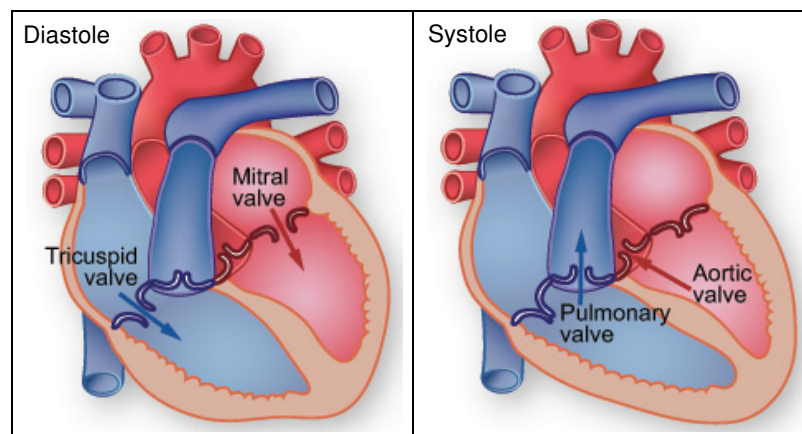
Figure 2:   Cross-section indicating the valves of the heart [11]

The aortic and mitral valves are subjected to higher pressures than the tricuspid and pulmonary valves and are therefore more susceptible to structural damage and degeneration [4, 12]. Degenerative heart disease in the elderly, which is increasing due to an overall increase in life expectancy worldwide, affects the aortic valve more commonly than the mitral valve [4, 13]. RHD affects both the aortic and mitral valves. Recognising the similarities between the functions and flow characteristics of aortic and mitral valves, this study focuses on the development of an aortic mechanical HVR.

The aortic valve comprises three semilunar cusps, known as leaflets. The leaflets are attached to the aortic wall, forming an annular ring. The aortic sinuses, which can be described as three bulges, two of which form the origins of the coronary arteries, are located superior to the annulus [14]. Together, these structures form the aortic root [15]. Figure 3a shows the anatomy of the aortic root (adapted from [16]).
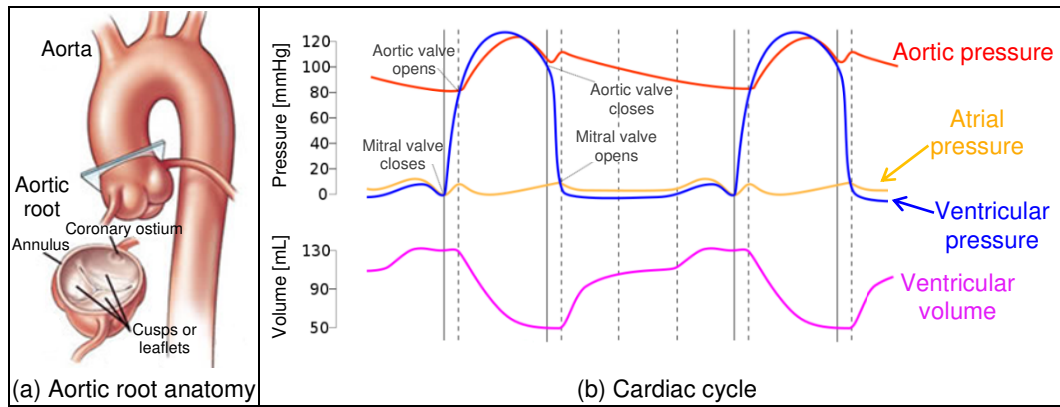
Figure 3: Anatomy and physiology of the heart [16, 17]

The aortic valve opens during systole, permitting blood flow into the aorta, and closes during diastole to prevent backflow. As the leaflets open and close, the annulus expands and contracts respectively [14]. On average, the cardiac cycle, shown in Figure 3b (adapted from [17]), is repeated 40 million times per year and 3.2 billion times in a lifetime [10].

Systole constitutes approximately a third of the cardiac cycle [14]. The start of systole is marked by isochoric contraction of the ventricles. This causes a sudden rise in pressure within the ventricles. Normal blood pressure during systole ranges from 100 mmHg to 130 mmHg (13.3 – 17.3 kPa) [3]. Isochoric ventricular contraction is followed by blood rushing through the opening semilunar valves. This is the start of the forward flow phase and is known as the systolic acceleration phase. Once the valves are fully open, maximum fluid velocity is attained. Blood flow through the aortic valve reaches a velocity of 1.35 ± 0.35 m/s, with a Reynolds number (Re) ranging from 4 000 to 6 000 [10]. After the peak velocity has been reached, blood flow starts to decelerate due to an adverse pressure gradient, which is known as the systolic deceleration phase. As blood flow slows down, vortices develop in the sinuses. At the end of the deceleration phase, the aortic valve closes with a backflow of less than 5% (or less than 5 mL) [13, 14]. Closing of the valve is initiated by the vortices applying pressure to the upper surfaces of the cusps. Blood flow eventually reverses direction, marking the end of the forward flow phase. During diastole, the aortic valve remains closed while the ventricle relaxes and refills. Normal blood pressure during diastole ranges from 65 mmHg to 85 mmHg (8.7 – 11.3 kPa) [3]. The functioning of the valve is driven by pressure differences across the valve. The rapid and efficient closure of the valve is aided by the vortices that develop in the sinuses [4, 14].

2.2 Heart Valve Disease

The functioning of any of the valves can be compromised by various congenital or acquired pathologies. Common pathological conditions of native heart valves are stenosis, referring to the narrowing of the valve opening, such as by calcification, and resultant restricted flow, and regurgitation, referring to incomplete valve closure and resultant leakage [4, 14]. Heart valve disease is defined as the presence of either stenosis or regurgitation, which impairs the cardiovascular system and reduces the efficiency of the heart, forcing it to work much harder than

typically required [4]. Although severe heart valve disease can be managed, it remains a mechanical problem that inevitably requires surgical valve replacement.

The acquired conditions that cause heart valve disease are mainly age-related, such as degenerative aortic valve disease, and RHD in the younger age group [5]. With a growing world population and an increase in life expectancy, particularly in developed countries, the occurrence of heart valve disease is increasing. Subsequently, the number of patients requiring HVR is on the rise [18]. Although the incidence of RHD has declined in high-income countries, it is the most common acquired heart disease among children and young adults in low- to middle-income countries, affecting an estimated 33 million people globally [4 – 6]. RHD is linked to socioeconomic factors such as poor living conditions, malnutrition, inadequate sanitation and limited access to healthcare.

It is important to highlight the distinction between the requirements of HVRs in developed and developing countries. In developed countries, HVR surgeries are primarily performed on older patients, due to degenerative valve disease. In developing countries, including South Africa, HVRs are performed on patients ranging from very young, due to the prevalence of RHD, to old. This phenomenon is illustrated in Figure 4 (adapted from [7]). HVRs in young patients must be durable to last until the end of the patient's life; therefore, mechanical valves are normally used. All patients with mechanical HVRs require lifelong anticoagulation therapy, which places them under an increased risk of haemorrhage related to anticoagulation therapy [19] or thrombosis due to inadequate effective anticoagulation programmes. In developing countries, factors such as poor healthcare services, lack of infrastructure and illiteracy exacerbate the problem by posing major challenges to the administration and regulation of anticoagulants.
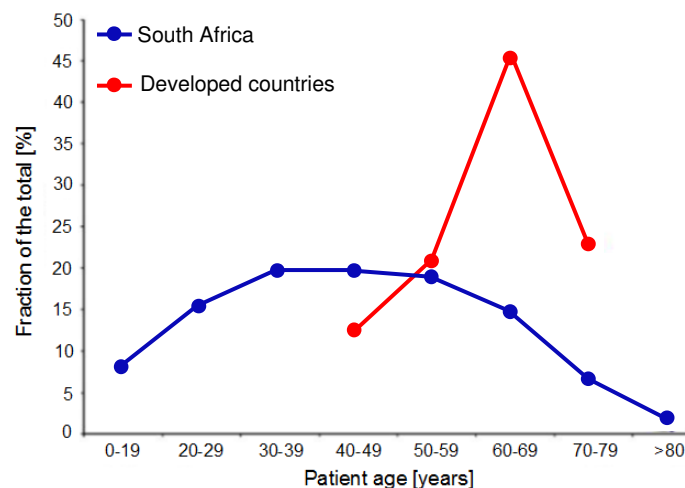
Figure 4:   **HVR recipient ages in South Africa and developed countries [7]**

A data set for HVR surgeries was obtained from Bestmed Medical Scheme, South Africa's fourth largest open medical scheme [20], for the period January 2015 to April 2019 [21]. The results are presented in Figure 5 and Table 1. The results reflect that 31% of the HVRs funded by Bestmed on behalf of its beneficiaries were mechanical valves. Note the differences in patient ages (mean age of

71.4 ± 8.5 years for biological and 51.3 ± 14.8 years for mechanical valves) and valve cost (mean cost of R34 879 ± 6 071for biological and R19 111 ± 4 630 for mechanical valves). This emphasises the need for a durable, more affordable HVR, even in the private health sector, in South Africa.
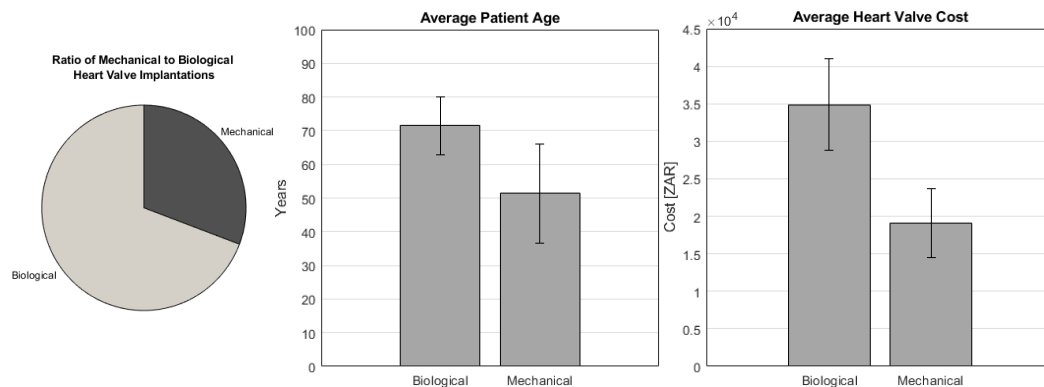
Figure 5:   Bestmed HVR data analysis

Table 1: Bestmed incidence rates per year per 1 000 beneficiaries

Age band [years]	Female	Male	Age band [years]	Female	Male
$0-10$	0.00000	0.00000	$40<-60$	0.14122	0.26588
$10<-20$	0.00000	0.02685	$60<-80$	1.11608	1.30036
$20<-40$	0.02359	0.09463	>80	1.87931	3.52162

2.3   Fluid Mechanics

Parameters exist that are used to assess the fluid mechanics and hydrodynamic performance of a valve and to gauge its level of stenosis or regurgitation. The relevant performance indicators are discussed in the following section.

2.3.1   Pressure Differential

The pressure difference (defined in Equation 1), or pressure drop, refers to the difference in pressure across a valve during the forward flow phase [3]. For an aortic valve, this is the difference in pressure between the aortic root and the left ventricle. A large pressure drop implies that the valve is resisting fluid flow and requires a higher ventricular pressure to induce and sustain blood flow through the valve [14]. This increases cardiac workload.

$$\Delta P = \frac{1}{t_2 - t_1} \int_{t_1}^{t_2} (P_{ventricle}(t) - P_{aorta}(t))dt \qquad (1)$$

ΔP = Mean pressure drop during the foward flow phase [mmHg or kPa]
t_1, t_2 = Time duration for $\Delta P > 0$ [s]
$P_{ventricle}, P_{aorta}$ = Ventricular and aortic pressure [mmHg or kPa]

2.3.2 Effective Orifice Area

The effective orifice area (EOA) is an indication of the open cross-sectional area of the valve during forward flow, calculated using Equation 2 [3].

$$\text{EOA} = \frac{q_{rms}}{51.6\sqrt{\Delta P/\rho}} \qquad (2)$$

$\text{EOA} = \text{Effective orifice area } [cm^2]$
$q_{rms} = \text{Root mean square flow rate for } \Delta P > 0 \text{ Pa } [cm^3/s]$
$\Delta P = \text{Mean pressure drop during the foward flow phase } [mmHg]$
$\rho = \text{Density of the test fluid } [g/cm^3]$

A small EOA indicates greater obstruction to flow and corresponds to a larger pressure drop across the valve [14]. A large EOA is imperative; EOAs that are too small have shown to increase the risk of heart failure by up to 80% [22]. EOA requirements for aortic valves, listed in Table 2, are prescribed by ISO 5840:2015 – Cardiovascular Implants – Cardiac Valve Prosthesis [3]. The performance requirements apply to test conditions of 70 cycles/min, cardiac output (CO) of 5.0 L/min, 100 mmHg mean arterial pressure (MAP) and systolic duration of 35%.

Table 2: Minimum ISO 5840 EOA requirements for aortic valves

Valve size [mm]	19	21	23	25	27	29	31
EOA [cm²]	0.70	0.85	1.00	1.20	1.40	1.60	1.80

2.3.3 Regurgitant Volume

Regurgitant volume refers to the total volume of retrograde flow, including the closing and leakage volumes [3]. The closing volume is the volume of fluid that is forced backwards by the closing action of the valve. The leakage volume is the volume of fluid that flows through the valve into the ventricle while the valve is closed; in other words, fluid that leaks through any gaps. Figure 6 (adapted from [3]) shows the regurgitant volume and its constituents. Total regurgitation is defined by Equation 3. A high regurgitant volume increases the load on the heart.

$$RV = \int_{t_1}^{t_2} q(t)\,dt \qquad (3)$$

$RV = \text{Regurgitant volume } [cm^3]$
$t_1 = \text{Start of backward flow phase } [s]$
$t_2 = \text{End of cardiac cycle } [s]$
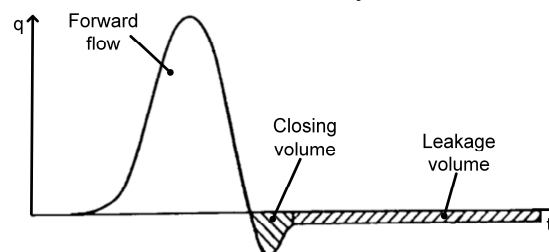
Figure 6:   Regurgitant volume [3]

The regurgitant volume can be expressed as a fraction of the stroke volume (SV), known as the regurgitant fraction. SV is defined as the volume of fluid that passes through the valve in the forward direction during one cycle [3]. Maximum regurgitant requirements, listed in Table 3, are prescribed by ISO 5840 [3]. These requirements apply to test conditions of 70 cycles/min, a CO of 5 L/min, 100 mmHg MAP and systolic duration of 35%.

Table 3: Maximum ISO 5840 regurgitant requirements for aortic valves

Valve size [mm]	19	21	23	25	27	29	31
Regurgitant fraction [%]	10	10	10	15	15	20	20

2.3.4 Flow Patterns and Turbulent Shear Stress

Flow through and around heart valves is important to consider when assessing the performance of a valve. Shear stress acting on blood cells and platelets can cause haemolysis and platelet activation if a minimum stress level is exceeded [8]. Haemolysis refers to the destruction of red blood cells (or erythrocytes) and platelet activation refers to the process whereby platelets are triggered to undergo a change in shape and chemical release that activates more platelets [23]. Activated platelets bind together, known as platelet aggregation, and start to form a blood clot. Aggregated platelets initiate the coagulation cascade, which is a complex chemical chain reaction resulting in the stabilisation and reinforcement of the clot. This process progresses at an exponential rate; more platelets are continuously stimulated by previously activated platelets.

There are several mechanisms of platelet activation and aggregation:

i. Shear forces acting on platelets activate platelets, causing aggregation and clumping. Forces are generated by friction, turbulence or direct mechanical trauma (impact or rapid closing of valves).

ii. Foreign material in contact with blood [24].

iii. Increased contact time between activated platelets, promoting aggregation. This occurs in recirculating and stagnant regions [25].

iv. Increased exposure to shear stress, which also occurs in recirculating and stagnant regions. Previous research has proven that platelets can be activated by stresses lower than the threshold value if the platelets are subjected to the stress for an extended period of time [26 – 30].

In summary, areas of high velocity and large velocity gradients cause haemolysis and platelet activation. Areas of low velocity and recirculation prolong exposure time and promote clot formation as well as tissue overgrowth [8, 14].

In the laminar flow regime, viscous forces dominate. Laminar flow is characterised by orderly, layered flow [31]. Newton's law of viscosity (Equation 4), states that viscous stress is proportional to the instantaneous velocity gradients in the fluid. The diagonal elements of the symmetric viscous stress tensor denote the normal viscous stresses and the off-diagonal elements denote the viscous shear stresses. The maximum shear stress is calculated from the principal stresses.

$$\tau_{ij} = \mu \left(\frac{\partial u_i}{\partial x_j} + \frac{\partial u_j}{\partial x_i} \right) \tag{4}$$

τ_{ij} = Viscous stress tensor [Pa]
μ = Dynamic viscosity [Pa·s]
u_i = Instantaneous velocity [m/s]
x_i = Displacement [m]
$i, j = 1, 2, 3$

Flow around mechanical HVRs is not laminar at all times and locations. In turbulent flow, inertial forces dominate. Flow transitions from orderly to disorderly. Turbulent flow is characterised by rapid fluid velocity fluctuations [31]. Due to turbulent flow's unpredictability, statistical methods, such as Reynolds averaging, are generally employed to model flow fluctuations [32]. The Reynolds-averaged Navier-Stokes (RANS) equations are derived by applying Reynolds decomposition to the flow variables. It is assumed that flow properties can be separated into a time-averaged component and a fluctuating component. As a result, the total stress tensor for turbulent flow (Equation 5) consists of two parts; the time-averaged viscous stress tensor and the Reynolds stress tensor (Equation 6), which arises due to velocity fluctuations. Typically, the viscous stresses are lower than the Reynolds stresses in the bulk flow and are considered the laminar component of the total stress tensor. Reynolds stresses are regarded as the turbulent component [31]. Maximum Reynolds shear stress (RSS) is calculated from the principal stresses.

$$\tau_{ij} = \mu \left(\frac{\partial \bar{u}_i}{\partial x_j} + \frac{\partial \bar{u}_j}{\partial x_i} \right) - \rho \overline{u_i' u_j'} \tag{5}$$

$$R_{ij} = -\rho \overline{u_i' u_j'} \tag{6}$$

$$\text{with } u_i' = u_i - \bar{u}_i$$

R_{ij} = Reynolds stress tensor [Pa]
ρ = Density [kg/m^3]
u_i' = Fluctuating velocity [m/s]
$\overline{(\cdot)}$ = Reynolds averaging operation

Experimental and numerical studies have been conducted to investigate the response of erythrocytes and platelets to shear stress to determine the maximum tolerable stress. Different researchers have analysed different types of shear stress and, as a result, a wide range of values is reported in literature [29, 30]. Turbulent shear stress levels from as low as 10 Pa to 100 Pa are considered the threshold stress level for platelet activation [8, 30]. The distinction between viscous shear stress, RSS and total shear stress is not always made in literature, which has created some uncertainty regarding which type of stress the threshold values refer to [30]. A threshold value for the Reynolds normal stress (RNS) does not exist, although studies have shown that the normal stress components can be larger than the shear stress components [32]. Hellums criterion is another common method used to determine platelet activation. The criterion takes the magnitude of the stress as well as the time duration into account and states that platelets are activated if the product exceeds 3.5 Pa·s [8]. The RSS threshold for haemolysis is greater than the platelet activation threshold, with reported values between 400 Pa

and 600 Pa [33 – 35]. A comprehensive list of shear stresses at various exposure times for the onset of haemolysis is tabulated in [29].

RSS has been regarded as one of the major HVR performance indicators [7, 8, 30, 33 – 35]. It is argued in [30] that it should not be used as a performance metric because it is a quantity that arises after applying Reynolds decomposition to the Navier-Stokes equations and does not a represent real stress. Although RSS is not the actual stress applied to blood constituents, it represents the real state of the fluid and experiments have shown that platelet activation and haemolysis are proportional to RSS [36].

Cavitation, which is mainly caused by high velocity jets [7], results in structural damage to the valve in the form of erosion or pitting [14]. This can lead to crack formation and failure and can alter the haemocompatibility of the material.

2.4   Types of Heart Valves

HVRs can be classified as either biological or mechanical. Biological valves, also known as bioprosthetic or tissue valves, are manufactured from chemically treated biological tissue. Although tissue HVRs are more biocompatible and have better hydrodynamic characteristics in comparison to mechanical HVRs, they are less durable, due to tissue degradation, and prone to calcification [8]. Bioprosthetic valves require replacement after approximately ten to fifteen years [8]. In younger patients, an accelerated failure rate has been observed and nearly all bioprosthetic valves implanted in patients below the age of 35 fail within five years [37]. They are generally not recommended for implantation in young patients and will not be considered further in this study.

Mechanical HVRs are manufactured from non-biological materials (e.g. polymers, carbon, ceramics or metal) [11]. Mechanical HVRs are durable, but the induced irregular flow patterns cause serious problems [8]. Mechanical HVRs can further be classified as rigid or flexible. Rigid valves are non-flexible under physiological conditions.

Three main types of rigid mechanical HVRs exist, namely the ball-and-cage, tilting disc and bileaflet valves. The ball-and-cage design is one of the earliest HVR designs and the bileaflet design is the most recent [8]. Each valve aimed to improve on the performance of its predecessor. All three types of rigid valves are still in use.

2.4.1   Ball-and-Cage Valve

The ball-and-cage valve consists of a rigid occluder confined in a cage-like structure, as shown schematically in Figure 7a (adapted from [8, 38]). These valves exhibit poor hydrodynamic performances due to turbulence and recirculation [8, 13]. During forward flow, the blood flows around the ball, reaching a velocity of 2.2 m/s at peak systole, for a 27 mm aortic valve tested at a heart rate of 70 beats per minute (bpm) and 6 L/min CO [14]. At the aortic wall and at the occluder, it is estimated that the turbulent shear stress is 350 Pa. During forward flow, flow separation occurs (refer to Figure 7b).

Some valve performance characteristics of HVRs are summarised in Table 4 [7, 8, 14]. The values listed are the average of experimentally tested 25 mm aortic valves tested at 70 bpm and ~ 5 L/min CO.
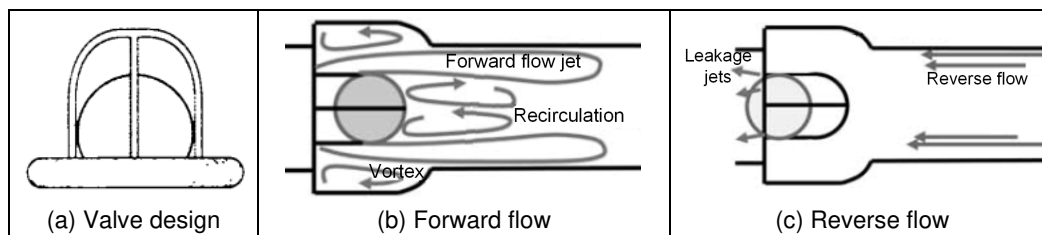
Figure 7:   Ball-and-cage valve design and flow patterns [8, 38]

Table 4: Summary of the characteristics of existing valves

Performance indicator	Ball-and-cage valve	Tilting disc valve	Bileaflet valve	Stented biological valve
EOA [cm^2]	1.62	2.3 – 3.07	2.39 – 3.97	1.52 – 3.25
Regurgitant volume [mL/beat]	4.3	7.3 – 8.4	6.1 – 11.2	< 2
Valve profile	High	Low	Low	Low

2.4.2   Tilting Disc Valve

The tilting disc (or monoleaflet) valve consists of a rigid disc-shaped occluder pivoting about an off-centre axis creating two different sized orifices, shown in Figure 8a (adapted from [8, 38]). Tilting disc valves exhibit poor hydrodynamic performances [13]. Two jets of differing speeds originate from the orifices, which result in recirculating flow (Figure 8b) [14]. A stagnation region downstream of the minor orifice during systole is observed. For a 27 mm aortic valve tested at 70 bpm and 6 L/min CO, a velocity of 2.1 m/s was measured at peak systole in the major orifice, 7 mm downstream of the valve [14]. Turbulent shear stress ranged from 120 – 150 Pa (7 – 13 mm downstream) [14]. During diastole, leakage through the gap between the disc and the housing forms high velocity jets, known as leakage jets [14]. The large pressure difference across the valve is the cause of the high-speed jets. Leakage jets are viewed as the main contributing factor to cavitation. Turbulent shear stresses during diastole are much larger than during systole. Valve performance characteristics are listed in Table 4.
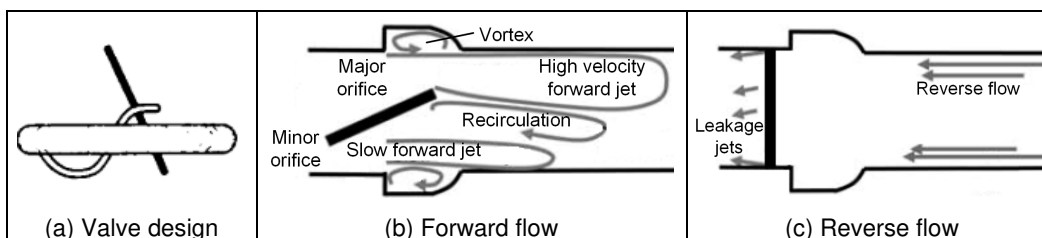
Figure 8:   Tilting disc valve design and flow patterns [8, 38]

2.4.3 Bileaflet Valve

Bileaflet valves consist of two semi-circular occluders, called leaflets, pivoting independently of each other by means of a hinge mechanism, shown in Figure 9a (adapted from [8, 38]). The leaflets divide the cross-section into one central and two lateral orifices, forming a triple jet pattern. Differences in velocity between the three jets can cause flow circulation and high turbulent shear stresses develop as a result of the velocity gradients. Other shortcomings of the bileaflet design include significant leakage, high-speed leakage jets and cavitation [13]. A 27 mm *St. Jude Medical* (*SJM*) aortic valve was tested at 70 bpm and 6 L/min CO [14, 39]. Velocities of 2.2 m/s were measured at peak systole in the lateral orifice, 8 – 13 mm downstream of the valve. Turbulent shear stress levels of 115 – 150 Pa were measured 8 – 13 mm downstream of the valve, noting that higher shear stresses probably developed closer to the valve, but were not measured. During diastole, leakage jets with average velocities of 2 – 3 m/s and turbulent shear stress exceeding 300 Pa were recorded 1 mm upstream of the valve, with much higher velocities and stresses occurring at the hinges. The hinge mechanism of the bileaflet valve, discussed in detail in §2.5.1.2, is one of the valve's most important features. Valve performance characteristics are listed in Table 4.
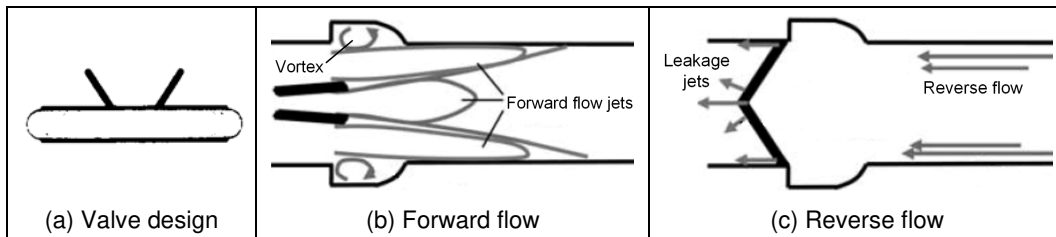
Figure 9: **Bileaflet valve design and flow patterns [8, 38]**

2.4.4 Trileaflet Valve

The trileaflet valve, shown in Figure 10 (reproduced from ([40, 41]), is similar to the bileaflet valve; however, it consists of three leaflets instead of two, as the name implies. Mechanical trileaflet valves have previously been investigated [40 – 45] and there are existing patents [46 – 51], but they are not being used in practice. French company, *Novostia SA*, has been developing a trileaflet heart valve, the *Lapeyre-Triflo* valve (Figure 10a), since 1980 (patent [51]). They have evaluated their design numerically and experimentally and it is stated that the results show that the valve exhibits superior hydrodynamic and kinematic performances compared to other mechanical HVRs [40]. However, the results are not published. Animal trials, with published results [44, 52 – 56], have been conducted. The results are promising and showed that the valve resulted in a smaller pressure drop, larger EOA, minimal downstream flow disruption, a higher cavitation threshold and did not activate the coagulation system [44]. The *Tricardiks* valve (Figure 10b) of the Russian company, *Roscardioinvest*, has been in development since 2001 [41]. *Roscardioinvest* states that they have been conducting successful clinical trials since 2007; however no *in silico*, *in vitro* or *in vivo* test results are publicly available. It is believed that further optimisation of trileaflet valves will provide younger patients with a durable HVR solution and a reduced dependency on anticoagulation therapy [57].

| (a) *Lapeyre-Triflo* valve | (b) *Tricardiks* valve |
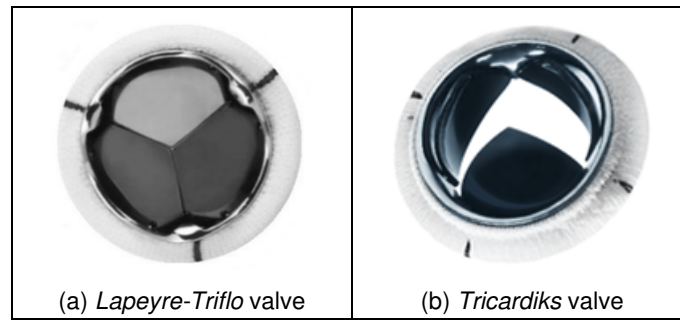
Figure 10:   Examples of rigid trileaflet heart valves [40, 41]

The improved performance of trileaflet valves compared to bileaflet valves is directly attributed to the leaflet configuration, which resembles the native tricuspid valve. The opening action of the valve also mimics a native valve, resulting in a more physiologically representative flow pattern. It is postulated that the mechanism of closure of trileaflet valves is the same as that of native valves. The closing action of bileaflet valves, as well as all other mechanical valves, is driven by reverse flow. Bileaflet valves only start to close during reverse flow, and because flow is accelerating in that direction, the leaflets close rapidly, and the closing volume is large. It is believed that trileaflet valves start to close during the deceleration phase due to the vortices that develop in the sinuses [45]. If this is true, it is speculated that the closing action of trileaflet valves is slower and gentler, with a smaller closing volume. The geometry of the leaflet can also contribute to a superior performance. The moment of inertia about the leaflet's rotational axis can be altered such that the leaflet has a smaller angular acceleration than bileaflet valves. Depending on the valve profile, the rotational arm can be shorter in comparison to a bileaflet valve, resulting in lower linear velocities at the leaflet tip. Each leaflet has a smooth, pointed shape at the trailing edge, which could reduce flow separation. The force that is exerted onto each leaflet pivot at closure is smaller compared to bileaflet valves, making the leaflets less susceptible to fatigue fractures. As a result, the thickness of the leaflets can be reduced, causing less obstruction to the flow.

Flexible types of mechanical trileaflet valves that represent the native semilunar valves more accurately, in terms of geometry and motion, have also been developed. They exhibit a similar haemodynamic performance to natural heart valves [13]. Flexible mechanical trileaflet valves are manufactured from polymers, such as polyurethane or silicon rubber [1, 13]. However, these materials have shown to have low durability and reliability. Polymer valves are not presently being used for implantation due to their poor performance [1, 7, 58]. Research into novel flexible materials with good mechanical properties that are biocompatible, affordable and manufacturable is ongoing [1, 58]. For now, the manufacturing of flexible trileaflet valves is limited to biological materials.

Trileaflet bioprostheses create a physiological flow pattern during systole, which consists of a single central jet. The regurgitant volume of bioprosthetic valves is small, due to a small closing volume and almost no leakage. However, the pressure drop tends to be greater than mechanical HVRs [14]. The larger pressure drop is as a result of several contributing factors, which include restricted leaflet motion by the stent and leaflet material stiffness as a result of the treatment procedures of

the biological tissue. For a 27 mm aortic valve tested at a heart rate of 70 bpm and 6 L/min CO, maximum velocities ranging from 2 – 3 m/s at peak systole were measured with turbulent shear stresses ranging from 100 – 450 Pa. The maximum stress occurs at the edge of the central flow jet. Valve performance characteristics are listed in Table 4.

2.5 Design Considerations

Designing an artificial heart valve that is comparable to a native heart valve is a challenging task. All aortic and mitral prosthetic valves (mechanical and biological) that have previously been studied, generate mean turbulent shear stresses greater than 20 Pa during systole and diastole, which can activate platelets [14]. Heart valves have to endure cyclic loading, flexing, bending, shear force, wear at the hinge mechanisms and wear due to cavitation in a harsh, corrosive environment [24]. Ideally, an artificial heart valve should be wear-resistant, biocompatible and have acceptable hydrodynamic characteristics such that it does not cause clotting or haemolysis [3, 14]. This implies that it should have a small pressure gradient, large EOA, small regurgitant volume and not induce high shear stress, turbulence, flow separation, stagnation or cavitation. It must be implantable, manufacturable and affordable. Once implanted, it should remain in place and not generate excessive noise [3]. The performance requirements depend on elements of the valve design such as geometry, shape, configuration and material. The key factors that must be considered are geometry and materials [13].

2.5.1 Geometry

A mechanical HVR assembly typically consists of the housing, occluder, retaining system and sewing ring [3, 13]. The housing, or orifice ring, holds the occluder; the occluder is the component(s) that opens and closes the orifice, allowing or restricting blood flow. The housing is encased in an outer ring or flange that serves as a means of structural reinforcement. The retaining system refers to the mechanism that holds the occluder within the housing, such as the cage of a ball-and-cage valve or hinges of bileaflet valves. The sewing ring facilitates implantation. The geometry of the valve assembly affects the flow and the motion of the occluder. Smooth, streamlined geometries for structural parts are associated with an improved haemodynamic performance [26]. The dynamics of rigid heart valves and the bulk flow characteristics are governed by large-scale geometry and pulsatile flow conditions [59]. Small-scale geometrical features, which include the occluder / leaflet edge or tip, leaflet articulating points, hinge recess geometry or subtle variations in leaflet curvature or gaps, have localised effects on microflow structures [59, 60].

2.5.1.1 Housing

The *On-X Life Technologies* bileaflet aortic valve is the only mechanical aortic valve with approval from the United States Food and Drug Administration (US FDA) for reduced anticoagulation therapy [61, 62]. The manufacturer claims to have optimised the length-to-diameter ratio of the housing, which is larger compared to other HVRs but comparable to native heart valves [8]. The housing inlet is tapered,

which has demonstrated to promote laminar flow, reducing the pressure gradient and increasing the EOA [7, 63, 64]. The longer-length housing also prevents the leaflets from being obstructed by overgrown tissue.

2.5.1.2 Hinge Mechanism

The hinge region is regarded as one of the most important features of bileaflet HVRs. Hinges are susceptible to wear and have been identified as sources of high velocities and shear stresses, particularly at the leakage jets, flow recirculation and stagnation. Turbulent shear stresses of up to 720 Pa have been measured within the hinge region of a 25 mm *SJM* bileaflet valve (standard model; unspecified test conditions) [14]. There is some belief that the leakage jets can be beneficial by dislodging clots within the hinges and preventing flow stasis [8]. However, the damage caused by the shear stress as a result of the velocity gradients outweighs the potential benefits of these jets [65]. Flow patterns around the hinges have been studied previously [25, 26, 66 – 72]. Flow within the hinge region remains difficult to visualise and compute (analytically, experimentally and computationally) due to limited optical access, leaflet dynamics and small geometrical features.

There are two main types of hinge configurations in bileaflet valves; male and female. Most hinge designs are based on the male configuration, where a small protrusion of the leaflet, referred to as the leaflet ear, rotates within a recess in the housing. The flow patterns within the hinge region for various male-configuration valves are shown schematically in Figure 11 (reproduced from [8]).
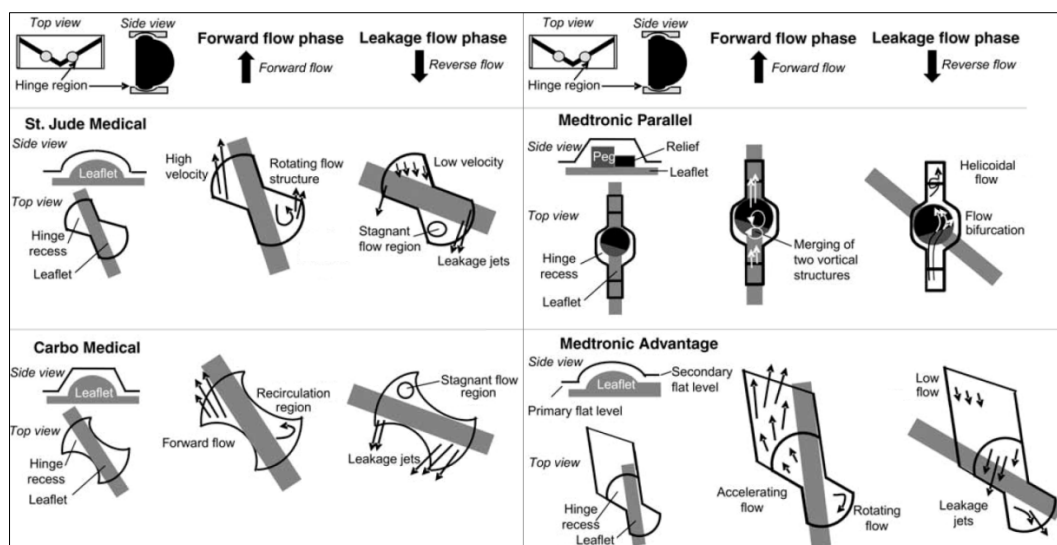
Figure 11:   Hinge geometries of some commercial bileaflet valves [8]

The leakage jet velocities and maximum shear stress around the hinges of three different *SJM* valves, a *CarboMedics* valve and the *Medtronic* Parallel valve are compared in [14]. The *SJM* Regent model (shown in Figure 11) had the lowest reported velocities and shear stresses, by a significant margin. The *Medtronic* Parallel valve (also shown in Figure 11) was discontinued due to poor performance, which is solely attributed to the hinge design [8]. In another study [70], the flow

within the hinge regions of the *On-X*, *SJM* and *Medtronic* Parallel valves are compared. Vortices and stagnant regions were observed in the *Medtronic* valve, but not in the *On-X* or *SJM* valves. Abrupt changes in the geometry at the pivot have shown to cause recirculating flow, stagnation and excessive flow disturbance [25, 26]. This refers to steps or sharp corners, compared to smooth geometry transitions. Considerable attention is given to the hinge mechanism to optimise the design, aiming to create a streamlined geometry with an improved fluid interaction.

Regarding the operation of the female hinge configuration, protrusions in the housing articulate with indentations in the leaflets. A two-dimensional (2D) computational study was conducted to investigate the difference in flow fields between the two hinge configurations [71]. It was found that the female configuration had a better haemodynamic performance during valve closure regarding maximum shear stress and exposure time. The limitation of this study is that three-dimensional (3D) effects were not considered.

The hinge geometry also influences the speed at which leaflets open and close. If the leaflets open and close rapidly, not only does this result in large velocity gradients, but the leaflets tend to rebound at the hinge stops before coming to rest. This causes physical damage to erythrocytes and platelets and additional flow disturbances. Increased leaflet closing velocities can also contribute to cavitation [7, 45, 73]. *On-X Life Technologies* alleges to have designed a hinge that facilitates gradual, smooth motion of the leaflets with a "soft landing" [63].

2.5.1.3   Leaflets

Large-scale leaflet curvature of bileaflet valves has been investigated experimentally using flow visualisation methods [74, 75]. In valves with flat leaflets (i.e. non-curved), flow through the lateral orifices is faster than flow through the central orifice. To promote flow through the central region, leaflets are designed with a convex curvature (with respect to the valve's axis). This has a positive effect on the convex side of the leaflet; the central orifice is widened, and smooth flow is promoted. However, on the concave side of the leaflet, the leaflet curvature has a negative effect on the flow. The flow is unstable and turbulent [75].

The maximum open angle of the leaflets is also important. As the maximum opening angle increases, there is less obstruction to the flow during peak systole. Therefore, the flow becomes more uniform, the size of the wake of the leaflets decreases, eddies around the leaflet trailing edges become less pronounced and the pressure drop decreases [7, 67, 72]. Flow separation and vortex shedding at the trailing edge of leaflets can further be reduced by reducing the thickness of the leaflets and streamlining the shape of the leaflets.

Some design features of commercial bileaflet valves are listed in Table 5 [76].

Table 5: Leaflet and hinge design features of major bileaflet valves

Feature	SJM	Carbo-Medics	Tekna	Bi-carbon	Med-tronic	On-X	Mira
Leaflet shape	Flat	Flat	Curved	Curved	Flat	Flat	Curved
Opening angle [°]	85	80	77 / 73	80	85	90	80
Sweep angle [°]	55 – 60	55	62 / 58	60	60	50	60
Leaflet pivot	Male	Male	Male	Male	Female	Male	Male
Core material	Graphite	Pyrolytic carbon	Pyrolytic carbon	Titanium	Pyrolytic carbon	Graphite	Titanium
Coating material	Pyrolytic carbon	None	None	Pyrolytic carbon	None	Pyrolytic carbon	Pyrolytic carbon

2.5.1.4 Gap Widths

Leakage flow is normally incorporated in the valve design to flush the hinge region and to prevent flow stasis [26, 66]. This is achieved by means of a geometrical clearance gap between the leaflets and the housing. This clears the hinge area of any blood clots or coagulation factors [77]. The clearance gap between the leaflets and the housing within the hinge region has been investigated to determine the effect on peak stresses, platelet activation and regurgitant volume. In [66], the clearance gap of a 27 mm *SJM* mitral valve (standard model) was evaluated experimentally by varying the gap size between 50 µm, 100 µm and 200 µm. Leakage increased with an increase in clearance gap size. The same trend was observed for the RSS and the converse was observed for the viscous shear stresses. The RSS for all three valves exceeded the platelet activation and haemolysis thresholds. It was concluded that the 100 µm gap size valve had the best overall performance. Similar results were obtained for the same valve in a separate study and confirmed the assumption that an optimal gap length exists between small and large gaps [25]. It was postulated that increasing the leakage by enlarging the gap, increases the number of cells exposed to the stress experienced during leakage and can also result in stagnation if the hinge recess is too deep [66]. The study also showed that the hinge gap clearance had a greater effect on platelet activation than the actual hinge geometry, which was corroborated by the 2D computational findings [67].

The gap clearance of a *Medtronic* Open Pivot bileaflet valve was investigated computationally [67]. The standard gap length of 38 µm was increased to 130 µm and 250 µm. It was computed that the smallest gap length produces the strongest, fastest jets and the longest platelet exposure time due to circulating flow. Therefore, stress accumulation for the smallest gap size was the largest. Regurgitant flow was the highest for the largest gap length. It was concluded that the optimal gap length has an intermediate value, which resulted in the same conclusion as the above-mentioned studies.

2.5.2   Materials

The biological compatibility of all materials used in medical devices must be evaluated according to the guidelines given in ISO 10993:2009 – Biological Evaluation of Medical Devices [78]. If the material has the same chemical composition of a material already used in commercial medical devices for the same application and has undergone the same manufacturing and sterilisation processes, then the material does not require re-evaluation. New materials must undergo material characterisation tests, which include tests for toxicity, reactivity, carcinogenicity, haemocompatibility and biodegradation [78].

The material must be biocompatible, thereby not causing haemolysis, thrombosis, infection, inflammation, calcification or elicit any other type of chemical or biological reaction [13]. The material should not degrade in its environment or emit any form of particles [13]. Regarding the mechanical properties of the material, it should be strong, hard and resistant (comparable to the properties listed in Table 6). The accessibility, cost and manufacturability of the material and the potential for mass production are also important considerations [19].

There are only a few engineering materials that meet these requirements. The flange (or outer ring) is typically manufactured from a titanium alloy, cobalt-chromium alloy or stainless steel [13, 24]. The housing material of various commercial bileaflet valves is listed in Table 5 [76]. Leaflets or disc type occluders are manufactured from pyrolytic carbon coated graphite or titanium or pure pyrolytic carbon [13, 24, 76]. Ball-type occluders are manufactured from silicon rubber or polyacetal (Delrin). The sewing cuff is made from a polypropylene, polytetrafluoroethylene (Teflon) or polyester (Dacron) fabric [13].

Pyrolytic carbon is a low temperature isotropic (LTI) carbon that was developed in the late 1960s and was first used for heart valves in clinical applications in 1968 [79]. Since then, it is estimated that approximately 95% of all mechanical HVRs have at least one pyrolytic carbon component. Pyrolytic carbon is produced by the thermal decomposition of a hydrocarbon without the presence of oxygen [79]. The hydrocarbon is heated to its decomposition temperature within a fluidised-bed reactor and, through a complex reaction, the hydrocarbon starts to crystallise on a substrate material. The substrate can be machined away, but in the case of prosthetic heart valves, the component is often manufactured from graphite and coated with pyrolytic carbon.

Pyrolytic carbon owes its success as a biomaterial to its haemocompatibility, durability and good mechanical properties (refer to Table 6) [24, 79, 80]. Pyrolytic carbon valves have lifetimes exceeding the expected lifetime of recipients [79]. However, alternative materials and manufacturing methods that are cheaper, faster and more accessible are sought.

Table 6: Mechanical properties of pyrolytic carbon and alumina

Property	Pure pyrolytic carbon	Silicon-alloy pyrolytic carbon	Single crystal alumina	Poly-crystalline alumina
Tensile strength [MPa]	200	> 200	637	274
Flexural strength [MPa]	493.7 ± 12	407.7 ± 14.1	1 274	490
Young's modulus [GPa]	29.4 ± 0.4	30.5 ± 0.65	392	372
Strain to failure [%]	1.58 ± 0.03	1.28 ± 0.03	0.1	0.1 – 0.7
Fracture toughness [MPa$\sqrt{m}$]	1.68 ± 0.05	1.17 ± 0.17	2.0 – 6.0	~ 3
Hardness (500 g load) [DPH]	235.9 ± 3.3	287 ± 10	-	-
Vickers hardness [GPa]	1.5 – 2.4	-	20.6	17.6
Density [kg/m^3]	1 930 ± 100	2 120 ± 100	3 970	3 920
Coefficient of thermal expansion [10^{-6} / K]	6.5	6.1	7.2 – 9.0	~ 5
Silicon content [%]	0	6.58 ± 0.32	-	-

Due to differences in thermal properties between the underlying substrate material and the coating, the production process creates residual stress in the components. Pyrolytic carbon has a larger coefficient of thermal expansion compared to graphite, so for pyrolytic carbon coated graphite parts a tensile residual stress is created in the coating. Depending on the production temperature, these stresses can reach up to 60 MPa, with the maximum stress occurring at the surface of the coating. Together with the operational stress, this can lead to premature fracture of the coating [24]. Other types of coatings are being investigated [81 – 83]; however, their use in long-term clinical applications is still under evaluation.

There is interest in ceramics as alternative materials for HVRs due to their inertness, strength and hardness. Alumina, zirconia and zirconia-toughened alumina are the most commonly used ceramics for other biomedical applications [84]. Alumina's mechanical properties are listed in Table 6 [24, 80, 85 – 88].

Alumina is stronger and harder than pyrolytic carbon. Therefore, without compromising the structural integrity, it should be possible to reduce the thickness of leaflets if a ceramic is used [80]. This will reduce flow obstruction. In [80], a tilting disc heart valve was developed with single crystal alumina. The thrombogenicity was investigated during *in vivo* testing. Post-explantation of the valves, it was observed that the discs showed no signs of platelet aggregation or clot formation. The valves were also subjected to fatigue tests. The ceramic valve survived 91 000 cycles at elevated pressures (1750 mmHg or 233.3 kPa). Three other valves (*SJM*, *Bjork-Shiley* and *Hall-Kaster*) were also tested and all failed within 80 880 cycles and at lower pressures. Ceramics with homogeneous microstructures or very fine grain single-phase ceramics demonstrate a better response to cyclic loading [85].

The structural parts of the valve should have low porosity and smooth surfaces so as not to damage erythrocytes or the endothelial tissue of nearby anatomical structures and to facilitate smooth motion [13]. Platelets adhere to rough surfaces, leading to clot formation [24]. Furthermore, rough surfaces can increase contact time of activated platelets. Absorption by a porous material can cause structural changes to platelets, triggering clotting [79]. A maximum surface roughness of 1 μm is recommended [80]. Surface defects can cause premature material failure and reduce the lifetime of mechanical HVRs by locally amplifying the applied stress. In [13] it was predicted that the lifetime of a pyrolytic carbon specimen with a surface defect in the form of a crack with an initial length of 40 μm is ~ 2.3×10^9 cycles (~ 63 years). However, if the initial crack length is 170 μm, the lifetime reduces to 0.9×10^8 cycles (~ 2.5 years). The blood-material interaction and the exact mechanisms of injury are not well understood. Thus, finding or developing alternative materials for heart valve applications remains a challenge [79].

2.5.3 Manufacturing Methods

Mechanical HVR components are manufactured using computer numerical control (CNC) machines, with accuracies of the order of a few microns [89]. The typical fabrication process consists of machining and forming, post-machining procedures, coating and polishing. Some parts are machined from stock (i.e. the outer ring) or cut / stamped from plate (i.e. flat leaflets). Figure 12 and Figure 13 are photographs showing the hinge detail on the housings of two different commercial valves. It was deduced that some sort of forming process most likely created these precise geometries.

| (a) Interior | (b) Exterior |
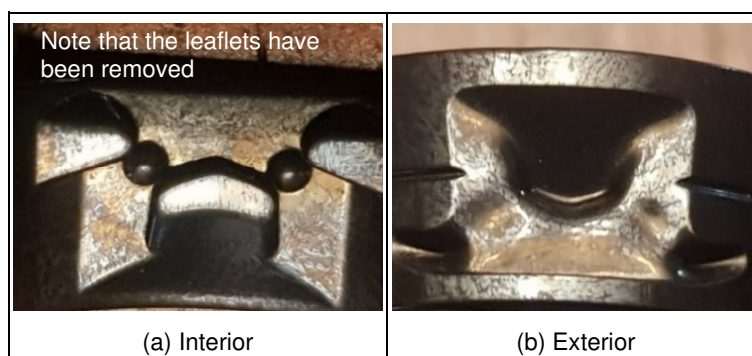
Figure 12:   Pivot mechanism of a typical female hinge configuration

Figure 13:   Pivot mechanism of a typical male hinge configuration

Additive manufacturing (AM) has previously been used for rapid prototyping and design optimisation of rigid heart valves [90, 91]. In [90], prototype rigid heart valves were manufactured using acrylonitrile butadiene styrene (ABS) on a machine with 0.1 mm accuracy. Various prototypes were developed and tested to obtain an optimised design. In [91], a rigid plastic trileaflet valve was developed for prototyping purposes. The model was scaled up by a factor of three. Problems were reported regarding the accuracy of the AM procedures and the surface finish of the parts, which resulted in excessive friction at the hinges. AM has not been considered for final product development for mechanical HVRs.

2.6 Experimental Validation Methods

Verification tests for prosthetic heart valves are described in ISO 5840. The tests include hydrodynamic performance tests and structural performance tests. Some standardised test methods exist, but other design-specific tests may be required depending on the outcome of a risk analysis that must be conducted [3]. Design-specific tests include leaflet escape force, leaflet impingement force, leaflet kinematics, cavitation and tests pertaining to the sewing ring. Exact test methods are not defined in ISO 5840, merely guidelines. It is specified that, where applicable, the test fluid used for *in vitro* tests must be saline, blood or a fluid with properties representative of blood. The test environment of heart valves is described in ISO 5840.

2.6.1 Pulsatile Flow Tests

Pulsatile flow tests are conducted to assess the hydrodynamic performance of heart valves under simulated physiological flow conditions [3]. The tests are conducted using an apparatus called a pulse duplicator [1, 4, 7]. A pulse duplicator is a simplified representation of the circulatory system with sensors to record time-dependent flow parameters, namely pressure and velocity [92]. The flow field in the region around the valve can be visualised by incorporating imaging techniques such as particle image velocimetry (PIV) or high-speed cameras.

The pulse duplication system, shown in Figure 14, comprises a computer-controlled pump, a physical model of the left side of the heart, sensors and a data acquisition system [92, 93]. The model of the heart consists of the atrium, mitral valve, ventricle, aortic valve, aortic root and a simplified arterial system that closes the flow circuit by connecting the aorta to the atrium. The pulse duplicator is designed to allow the user to adjust the compliance and resistance of the system. For the system shown in Figure 14, the compliance of the ventricle and aortic root are adjustable, and the resistance as well as the compliance of the arterial system are adjustable. Compliance is adjusted with the use of compliance chambers, which are sealed chambers that contain a mixture of air and fluid. The volume of air is controlled by using a syringe to inject or extract air.
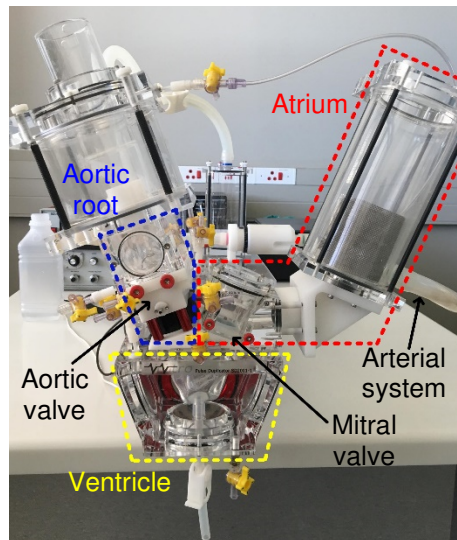
Figure 14:   Labelled photograph of the *ViVitro* pulse duplicator

Resistance refers to the total resistance of the arterial system, influenced by blood vessel length, diameter and fluid properties (i.e. viscosity). Compliance refers to the relationship between the change in volume and change in pressure within a heart chamber or blood vessel [94]. The higher the compliance, the greater the degree of vessel expansion due to an increase in internal pressure. Compliance is not linear; as the vessel expands, the stiffness increases and compliance decreases. It also depends on patient-specific factors like muscle and vascular wall thickness, orientation of muscle fibres and connective tissue [95]. Simulating compliance accurately is not trivial. Compliance also acts as a form of damping to reduce peaks and high frequency pressure and flow oscillations and creates more physiologically representative waveforms [96, 97].

Compliance is described mathematically in ISO 5840 [3]. However, the values needed to compute compliance according to ISO 5840 cannot be measured accurately, repeatedly or instantaneously in the physical test setup. Therefore, in this study, compliance is quantified in terms of volume of air in the compliance chambers. Lower compliance is deemed valid for simulating normal aortic conditions in adults and higher compliance is valid for simulating normal aortic conditions in children. Exact compliance conditions are not specified in ISO 5840. Some pulse duplicators are completely rigid with zero compliance.

Other test conditions that must be specified for pulsatile flow tests are heart rate, CO (i.e. net fluid forward flow volume per minute), SV and MAP. The measured data can be used to calculate flow rate, forward flow phase duration, EOA and regurgitant volume, calculated as the average of at least 10 cycles. Due to the unsteady nature of the flow and the influence of experimental parameters, specifically compliance and resistance, experimental variation is observed [92, 98].

In general, a pulse duplicator is used as a comparative evaluation tool rather than as a means of direct evaluation. The hydrodynamic performance of the test valve is compared to the hydrodynamic performance of a benchmark valve under identical test conditions. By comparison, it can be determined whether the test

valve outperforms the benchmark valve. For this reason, less consideration can be given to the exact test conditions, as long as the conditions remain constant.

2.6.2 Imaging Techniques

Flow visualisation methods exist that can be employed to observe the flow field and leaflet kinematics, including PIV, laser Doppler velocimetry (LDV) and high-speed cameras.

PIV is a flow visualisation tool that is used to track fluid flow through a pulse duplicator and characterise the flow field [7, 29]. The fluid is seeded with foreign particles that should have similar fluid properties to the test fluid. The flow through the pulse duplicator is recorded at a high frame rate, under laser light to illuminate the particles. The instantaneous velocity of the particles is calculated based on consecutive images, which is used to calculate the shear stress. PIV can be used to extract the 3D flow field; however, most setups accommodate 2D visualisation.

Leaflet motion analysis is conducted during pulsatile flow testing with the use of high-speed cameras [93, 99 – 102]. Frame rates for heart valve applications vary from 500 fps [99] to 12 000 fps [102]. The motion of the leaflet is tracked over the leaflet trajectory to determine the size of the open orifice, calculate opening / closing velocities and observe and quantify leaflet flutter and asymmetry. The recorded motion can be used to validate computational analyses or to specify input conditions. Several sources of uncertainty related to HSV motion analysis are identified in [103]. The total uncertainty error is the root sum square of each contributing factor. The following factors contribute to the total uncertainty:

i. Calibration uncertainty – refers to reference dimension measurement errors and large distances between the calibration and motion planes.
ii. Gamma angle (γ) uncertainty – refers to the difference between the angle of the camera and the experimental setup. If the axis of the camera is perpendicular to the setup, γ uncertainty is zero.
iii. Motion blur uncertainty – refers to blurring of the image such that the target cannot be located accurately. It was interpreted that this source of uncertainty also refers to any other target tracking errors.
iv. Perspective error – refers to the inherent image distortion, which increases towards the outer edges of the image and is minimal at the centre.
v. The accuracy of the camera's chronometer.

2.6.3 Durability Tests

Durability tests must be performed to ensure that the heart valve remains operational for at least 400 million cycles for rigid HVRs [3]. "Operational" means that the regurgitant volume and pressure difference across the valve remain stable throughout testing, although some structural damage is acceptable. Excessive structural degradation, such as fragmentation, fracture or delamination, is classified as valve failure. The differential pressure across an aortic valve replacement must be maintained at the normotensive pressure stipulated in

ISO 5840 for at least 95% of the duration of the test. For the other 5%, the pressure should be equal to or greater than the specified pressure.

2.6.4   Fatigue Tests

Fatigue tests are conducted to determine the structural lifetime of the valve [3]. This refers to the duration for which the valve can withstand maximum loading. A stress / life (S/N) analysis or a damage-tolerance analysis can be conducted.

For S/N analysis, smooth or notched material specimens are cycled to failure at a range of stress levels. The lifetime is estimated based on the number of cycles to crack initiation and propagation, after accounting for various adjustment factors. The damage-tolerance approach is a more conservative test, which is favoured for high-risk applications [24]. The approach is based on the assumption that the parts have existing defects and the minimum safe structural life is determined by the time it takes for the existing defects to result in failure [24]. The test should be performed following a worst-case approach and focus on the most critical and highly stressed locations.

2.7   Numerical Validation Methods

High-fidelity computational fluid dynamics (CFD) simulations can be used to improve the understanding of the interaction of blood with rigid heart valves. CFD also allows for the observation and analysis of a continuous 3D flow field in high resolution, which is not possible with discrete 2D flow visualisation methods. CFD has been used since the 1970s for heart valve applications. Initially investigations were limited to 2D models, with 3D models being developed much later [93].

Developing accurate computational models of prosthetic heart valves in the operating environment is a challenge. Factors contributing to the complexity are fluid-structure interaction (FSI), pulsatile flow, turbulence and complex geometries with small- and large-scale geometrical features (typical dimensional differences of up to three orders of magnitude). For rigid HVRs, the rapid opening and closing of the leaflets (~ 10 – 20 ms closing time) due to the small leaflet moment of inertia and the solid-solid contact with friction at the hinges add to the complexity. For the most accurate results, high spatial and temporal resolution models are required to solve the Kolmogorov length and time scales or the Taylor microscale [30].

During the cardiac cycle, flow through a prosthetic heart valve transitions from laminar to turbulent. Ideally, all the temporal and spatial scales of turbulence should be solved exactly by direct numerical simulation (DNS). Due to the computational cost, DNS is not feasible and turbulence models, such as large eddy simulation (LES) or RANS models, are employed. RANS models with special near-wall treatment are often used. However, RANS models were developed for fully turbulent flow and can introduce errors in non-turbulent regions. LES or hybrid models have limited applications also due to their computational expense [104].

Numerical investigations of bileaflet HVRs are conducted following three main approaches. In the first approach, the interaction between the fluid and the

structure is ignored. The leaflets are fixed in position and steady state conditions are often assumed [67, 72, 105 – 110]. A model with stationary leaflets was used to investigate the assumption of symmetry, which is frequently made based on the geometrical symmetry of heart valves [111]. The problem was solved by DNS and the results indicate that the flow has a complex 3D nature and questions the validity of studies where symmetry is assumed.

In the second approach, the interaction between the fluid and the structure is accounted for by employing a coupled physics solver. Studies following the FSI approach often assume laminar flow [65, 112 – 115]. However, in heart valve applications Re = 0 - 10^4 [116]. Simulations with pulsatile inlet flow conditions where laminar flow was not assumed have been solved by DNS [93, 100, 117]. However, other trade-offs were made to simplify the problem. In [93], the smallest scales were not resolved (i.e. LES and not DNS) and in [117] the hinge geometry was ignored. In [100] the hinge geometry was neglected, gaps were increased and leaflet rotation was restricted such that the leaflets did not close completely. It is reported that numerical instabilities often arise in FSI analyses due to the small moment of inertia of the leaflets [100]. In [45], the FSI problem was solved with a RANS solver. The results were compared to experimental results. The CFD model overestimated the maximum leaflet closing velocity and maximum fluid velocity. This is discussed further in §4.2.4.

The third approach can be classified as a hybrid approach. Leaflet motion is not ignored; however, instead of computing the interaction between the fluid and the solid, the motion is defined by the user as input. The motion of the leaflets affects the fluid, but the converse is not true [104]. The first validated 3D DNS analysis of a bileaflet valve with pulsatile flow conditions was developed in 2007 following this approach [59]. The model was simplified by neglecting hinges and leakage jets. Leaflet motion was specified based on *in vitro* HSV analysis. The tests revealed that the motion of the leaflets is complex; large accelerations, leaflet flutter and asynchronous motion were observed. The authors speculate that the asymmetrical leaflet behaviour is attributed to small differences in manufacturing tolerances at the hinge regions, which affect the leakage jets and consequently the motion of the leaflets. Significant variation in leaflet motion between cycles was also observed, especially during the closing phase. Therefore, the average motion recorded over multiple cycles was defined as input. The prescribed kinematics approach has been employed in other studies [33, 60, 116, 118 – 120].

Whether the FSI or hybrid approach is followed, simplifications are generally required to solve the unsteady CFD problem. This includes scaling or modifying leaflet geometry to increase gap widths [45, 65, 93, 114, 120, 121] or ignoring / simplifying the hinges [59, 113, 114, 116, 117]. In doing so, complex micro-scale flow structures generated by small geometrical features are ignored.

Many HVR numerical studies based on boundary fitted methods, which are commonly used for rigid heart valves, are summarised in [122]. The assumption of laminar flow was made in 66% of the studies and, for the remainder of the studies, turbulence was treated using either RANS models (20%), unsteady RANS (5%), LES (2%) or DNS (7%). In 23% of the studies, the analyses were simplified to 2D. For the 3D studies, no distinction is made between full or symmetrical 3D models.

RANS models are suitable for analysing large-scale fluid mechanics [8, 116, 123]. They offer the advantage of being the least computationally expensive while still being able to compute the bulk flow field. However, to analyse small-scale flow features, such as in the hinge regions or leaflet gaps, more accurate methods, such as DNS or LES, are required. A multi-scale approach is recommended in [8], where a large-scale solver is coupled to a highly resolved small-scale solver. The small-scale solver should ideally model blood down to the cellular level (i.e. not as a single-phase Newtonian fluid) that can track individual particles to compute shear stress accumulation and exposure times. Although advancements in this field have been made [67, 68, 119, 124], a fully coupled multi-scale simulation that includes transient flow conditions, FSI and accurate modelling of blood, has not yet been solved. To study the hinge flow, experimental investigations using transparent housings are rather conducted [26, 66, 69, 77, 125, 126].

There is some literature available on the numerical investigation of rigid trileaflet HVRs. The opening and closing motion of a trileaflet valve (*TRI* valve, patent [46]) was analysed with the use of *ANSYS Fluent* [45]. The FSI approach was followed, with a RANS turbulence model and 1/3rd symmetry assumption. The *Triflo* valve was studied numerically in [120], also using *ANSYS Fluent*. Leaflet kinematics were prescribed and 1/6th symmetry was assumed. Due to numerical instabilities, the study consisted of 32 individual simulations; each simulation modelling three degrees of rotation. The authors report wall y^+ values ranging between 2 and 11. At low wall y^+ values ($y^+ < 1$), the boundary layer is explicitly solved, which requires fine meshes at the boundaries. At high wall y^+ values ($y^+ > 30$), the boundary layer is modelled. The reported wall y^+ values do not fit into either category. The numerical code does not know whether the boundary layer should be solved or modelled. This is especially relevant when looking at results affected by the boundary layer, such as shear forces. It questions the accuracy of the results if a wall y^+ sensitivity analysis was not performed. Finally, a CFD analysis was conducted on a prototype trileaflet heart valve in [127, 128] (patent [49]). Steady flow, low Re and symmetry were assumed. Leaflets were stationary and fully open. The investigation showed that leaflets that are aligned to the direction of flow when open result in more uniform flow, smaller pressure drop and lower shear stress.

2.8   Animal Studies

Before proceeding with the clinical investigation of a novel heart valve, animal testing is required [3]. The *in vivo* reaction to the HVR and the replacement's performance must be assessed using an appropriate large animal model. However, it is necessary to consider the limitations of large animal models. Different animal orders and species respond uniquely to prostheses and pharmaceuticals based on their genetic makeup [129 – 131]. For heart valve applications, this refers to the animal's response in terms of platelet behaviour, coagulation and calcification. Caution should be exercised when extrapolating preclinical *in vivo* test results to humans. Although successful animal studies can provide immensely useful data concerning the safety of prosthetic heart valves, they are not a substitute for a thorough review of relevant literature, a sensible design approach and *in vitro* and *in silico* HVR design evaluations.

3 DESIGN AND PROTOTYPE DEVELOPMENT

Figure 15 is a schematic of the generic product development process. The portion highlighted in red relates to prototype development, which was the focus of this research project. Aspects of the design that are associated with the final product development, which include preclinical and clinical trials, sterilisation, packaging, labelling, storage etc., are not within the scope of the project.
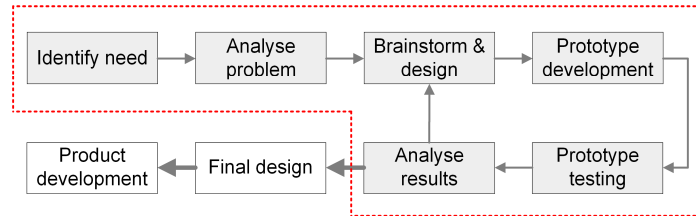
Figure 15: **Product development process**

3.1 Requirements Analysis

Despite the perceived simplicity of mechanical heart valve design, combining design and function with biological interaction becomes quite complex. This is set out schematically in Figure 16 and Figure 17. A systems approach was followed to analyse the problem, identify the relationships between the variables and extract system requirements. The approach was tailored to suit the problem.

3.1.1 Systems Analysis

Figure 16 shows the system block diagram, with the physical interfaces of the system, as well as the context diagram in blue. The context diagram shows the entities related to the system. The entities / actors are external stakeholders, processes or systems that directly interact with the system. "Other" refers to the final product related entities that have not been considered. A modified functional diagram, Figure 17, was created to identify the relationships between the elements of the system and the actors. A description of Figure 17 follows.
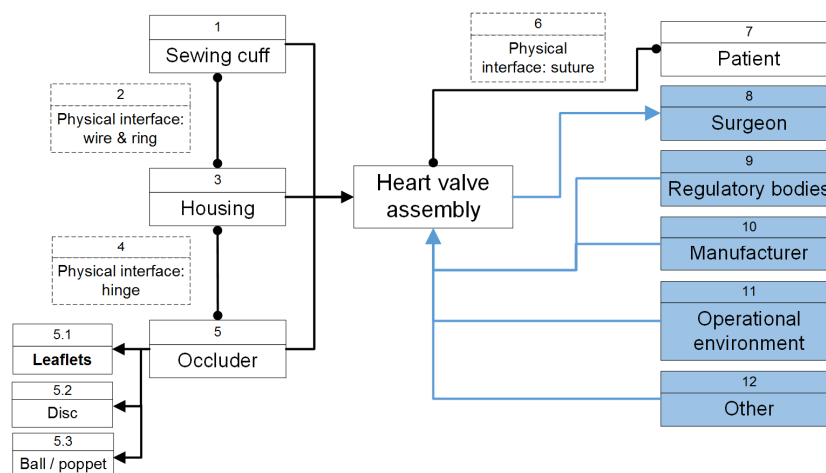
Figure 16: **System block and context diagram**
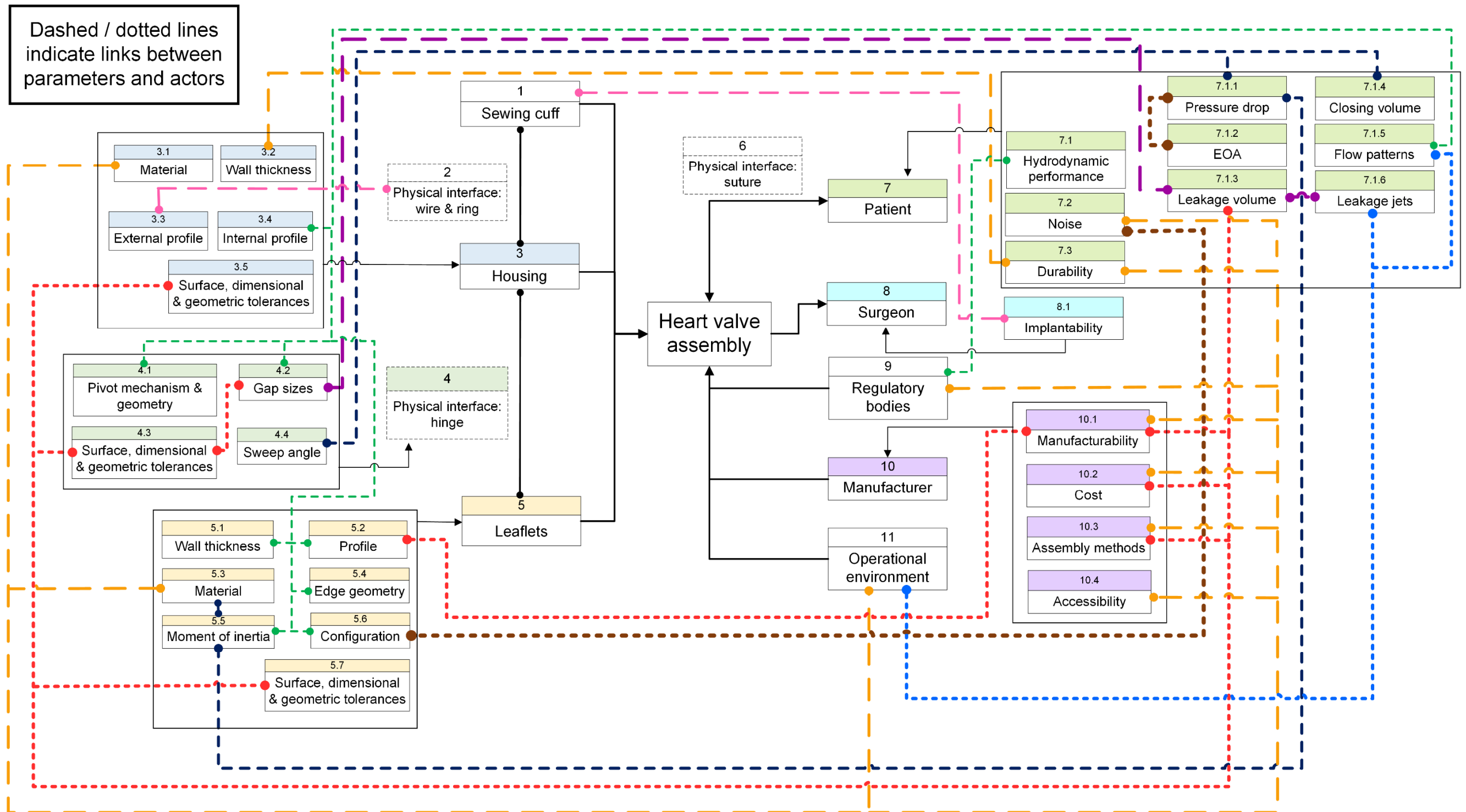
Figure 17: Functional diagram

In Figure 17, each element of the system, in terms of its physical parameters, and the demands of the actors on the system were expanded. The intricacy of the interconnected features of mechanical HVRs are emphasised. Every feature of the valve has an impact on the overall functioning and performance.

3.1.2 Failure Modes, Effects and Criticality Analysis

A tailored Failure Modes, Effects and Criticality Analysis (FMECA) was performed to identify the potential mechanisms of failure of each component of the system and to determine the impact of failure on the system. In doing so, actions can be implemented to prevent the potential failure and techniques to verify the design can be developed. The analysis is presented in Appendix A.1 (Table 18). Only failure modes pertaining to prototype development have been considered. Failure modes of the sewing cuff and outer stiffening ring, which are relatively standard parts, have not been considered. Although other failure modes are not applicable to prototype development, they should be kept in mind.

3.1.3 Requirements

The prototype valve's requirements were considered. Although material and manufacturing requirements have been included, they are not essential for prototype development and proof of concept purposes. From the onset of this project, it was accepted that, for cost and scheduling purposes, the required manufacturing tolerances will most likely not be achieved.

3.1.3.1 Functional Requirements

i.   The HVR must open and close during systole and diastole respectively.
ii. The housing must allow for physical interfacing with relevant anatomical structures and remain fixed once implanted.
iii. Motion of the occluder(s) must be constrained such that it does not physically interact with any anatomical structures.

3.1.3.2 Performance Requirements

i.   The valve must be tested *in vitro* according to the guidelines given in ISO 5840 and demonstrate functional capability.
ii. The EOA must equal or exceed 1.2 cm^2; tested at 70 bpm, CO of 5.0 L/min, 100 mmHg MAP and systolic duration of 35%.
iii. The pressure drop of the prototype valve should be less than that of a similar-sized reference valve, which must be measured experimentally under identical test conditions.
iv. The maximum regurgitant fraction must be 0.15; tested at 70 bpm, CO of 5.0 L/min, 100 mmHg MAP and 35% systolic duration.
v.   The regurgitant volume of the prototype valve should be less than the regurgitant volume of the reference valve. The regurgitant volume of each valve must be determined experimentally under identical test conditions.
vi. The closing speed of the prototype valve must be less than the closing speed of a reference valve. The closing speed of each valve must be determined experimentally under identical test conditions.

vii. The valve must be functional for 400 million cycles tested as per ISO 5840.
viii. The performance characteristics obtained experimentally and numerically should ideally improve on the performance characteristics of bileaflet valves cited in literature. The *in vitro* hydrodynamic performance characteristics of the prototype valve should match or exceed those summarised in Table 4. The numerical results should match or exceed those summarised in §2.4.3.

3.1.3.3 Material Requirements

i. The material must be biocompatible, demonstrated by meeting the requirements of ISO 10993-1.
ii. The mechanical properties of the material should be comparable to the mechanical properties of pyrolytic carbon (listed in Table 6). Deviations must be substantiated.
iii. The material must behave rigidly under operating conditions.

3.1.3.4 Manufacturing Requirements

i. The parts must have smooth, non-porous surfaces with a surface tolerance of 1 µm (or better).
ii. Dimensional tolerances vary from 5 µm for critical dimensions to a maximum tolerance of 0.1 mm. A suitable precision manufacturing method must be specified. Dimensional and geometric tolerances are indicated in Appendix B.

3.2 Prototype Design

Solid models were created using *Autodesk Inventor* 2018.0.2. The FMECA highlighted the hinge and leaflets as priority design features. Tolerances, accuracy of manufacturing processes and surface finish are also critical design aspects.

3.2.1 Bileaflet Valve Design

The *On-X* aortic valve is shown in Figure 18 (adapted from [132, 133]). The main features of the *On-X* valve were incorporated in the trileaflet valve design, considering the valve has demonstrated good performance characteristics [61, 62].
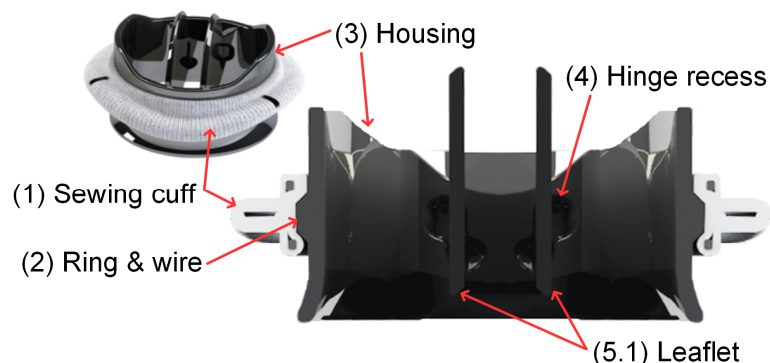
Figure 18: *On-X* bileaflet aortic valve [132, 133]

A custom bileaflet valve, replicating the *On-X* valve, was designed. Figure 19 shows the custom bileaflet valve. The hinge geometry of the *On-X* valve was modified such that the leaflets only have one degree of freedom, namely rotation. The purpose of designing a custom bileaflet valve was to manufacture a reference bileaflet valve using the same methods and materials as the trileaflet valve so that only valve performance is compared during testing.
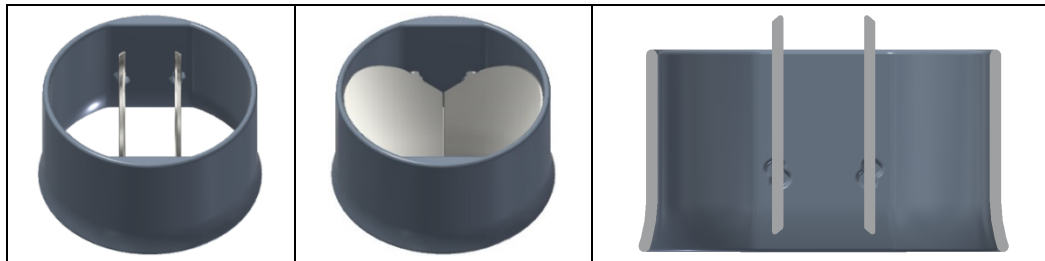
Figure 19:   Simplified replica of the *On-X* bileaflet aortic valve

3.2.2   Trileaflet Valve Design

3.2.2.1   Housing

The housing design was based on the *On-X* valve's housing, with a larger length-to-diameter (L:D) ratio and a flared inlet. In bileaflet valves, tissue overgrowth can obstruct valve closure [7, 8]. A longer length housing can resolve this problem by restricting tissue overgrowth in the vicinity of the leaflets. Trileaflet valves close with the leaflet tip moving towards the centreline; therefore, the closing is unlikely to be affected by tissue overgrowth. However, opening can be affected. It is acknowledged that the optimised L:D ratio for bileaflet valves might not be applicable for trileaflet valves. The outer ring and sewing cuff were considered standard components.

3.2.2.2   Hinge Mechanism

Two hinge concepts were considered. The first concept is a male-type hinge (protruding leaflet; recessed hinge), based on the *On-X* valve design. Concept 1 (C1) is shown in Figure 20. The second concept is a female-type hinge (recessed leaflet; protruding hinge), based on the *Medtronic* Open Pivot valve design. Concept 2 (C2) is shown in Figure 21. C1 is a simpler design; improving the manufacturability and reducing the associated time and cost of manufacturing. The gap width within the hinge region of the C1 type valve is 100 µm.
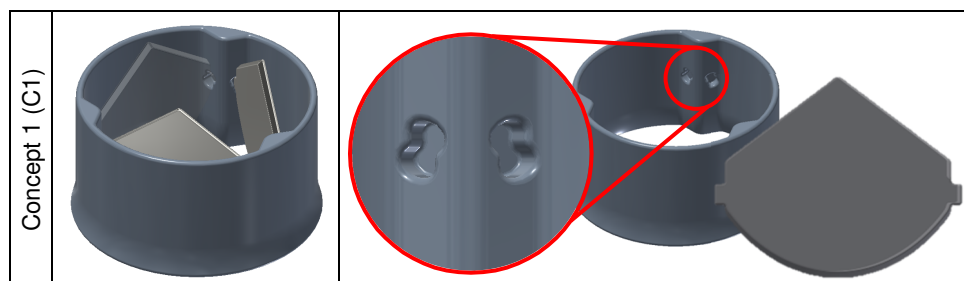
Figure 20:   C1 type valve hinge and leaflet geometries
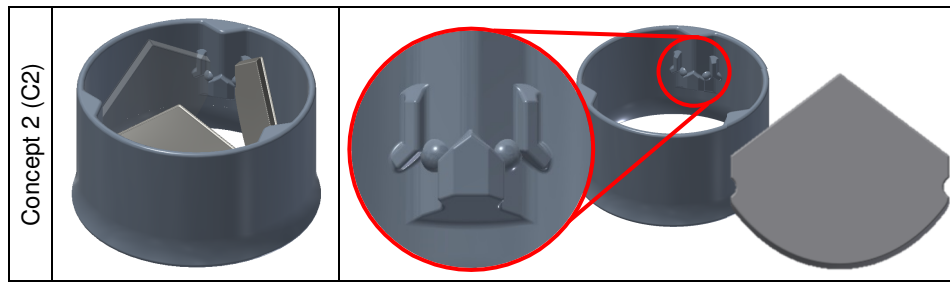
Figure 21:   C2 type valve hinge and leaflet geometries

3.2.2.3   Sweep Angle

The *On-X* valve is designed to close at 40° to the horizontal axis and open to 90°. The 50° sweep angle results in a smaller closing volume compared to other bileaflet valves (~ 60° sweep angles; refer to Table 5). An open angle of 90° ensures maximum flow through the valve and reduces turbulence. However, studies have shown that the leaflets do not open to 90° in operation [99, 134]. Open angles of 78.6° in the aortic position have been reported. The 40° to 90° design formed the basis of the trileaflet hinge design. Two additional closed angles, 20° and 30°, and open angles, 80° and 85°, were investigated. The maximum open angle was reduced from 90° if the valve does not close as expected, relying on reverse flow instead. The valve assemblies in the closed and open positions are shown in Figure 22 and Figure 23.
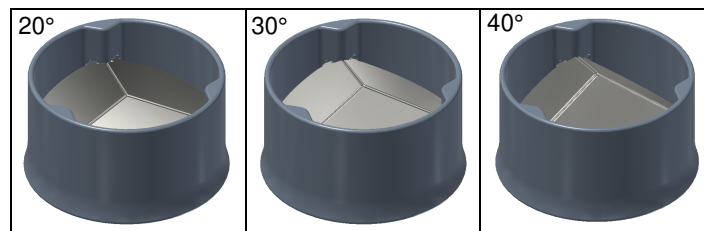
Figure 22:   Isometric view of the valve assembly in the closed position
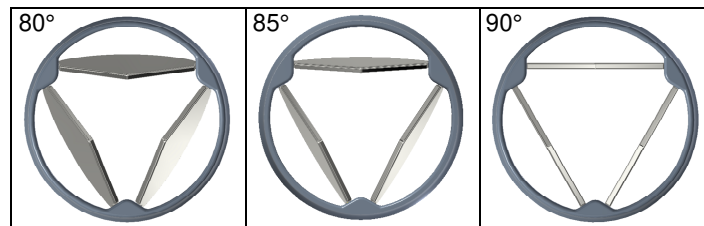
Figure 23:   Top view of the valve assembly in the fully open position

3.2.2.4   Leaflets

The forces acting on the leaflets during systole are indicated schematically in Figure 24. It was assumed that the pressure force is the dominant force (neglecting shear force, gravity and friction) and that the pressure does not vary over the surface of the leaflet. A constant pressure was assumed, which was simplified to equivalent point loads acting through the centroids above and below the leaflet's rotational axis. The torque acting on the leaflet is equal to the sum of moments about the axis of rotation as a result of the net pressure forces.
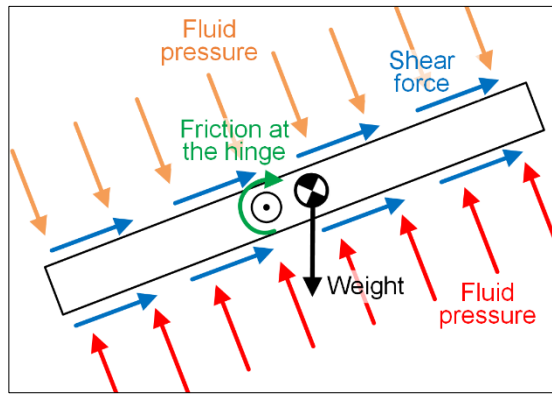
Figure 24:   Free body diagram of a leaflet (during systole)

Flat and curved leaflets were considered. Flat leaflets are easy to manufacture whereas complex geometries reduce the ease of manufacture, particularly if AM methods are not used. Leaflets with varying radii and direction of curvature were considered. The closed angle of the curved leaflet design ranged from 30° to 50° (low to high profile). The trileaflet valves with the various leaflet designs are shown in Figure 25 and Figure 26 (only C1 is shown).

	Concave 1	Concave 2	Convex
30° - 90° flat	30° - 90°curved	30° - 90° curved	30° - 90° curved
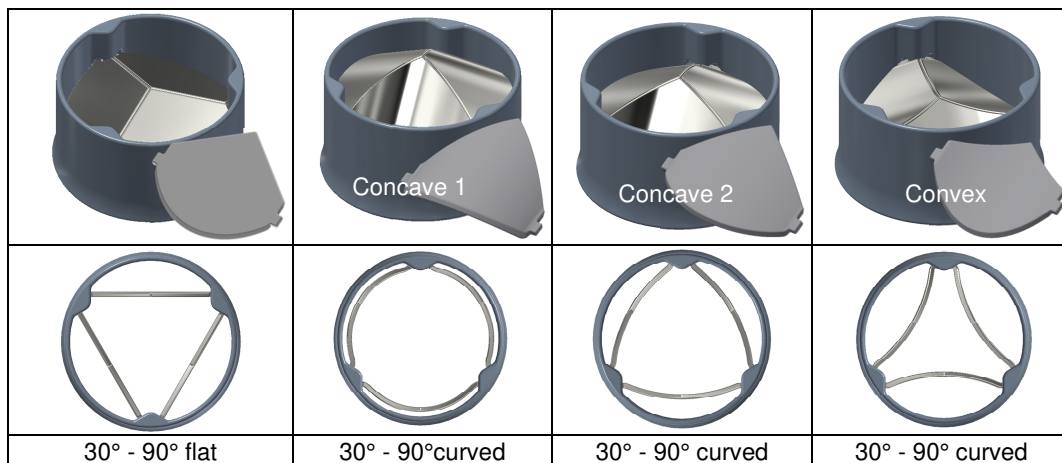
Figure 25:   Leaflet designs and configurations (1)

Concave 1	Concave 2	Concave 1	Concave 2	Concave 3
40° - 90° curved	40° - 90° curved	50° - 90° curved	50° - 90° curved	50° - 90° curved
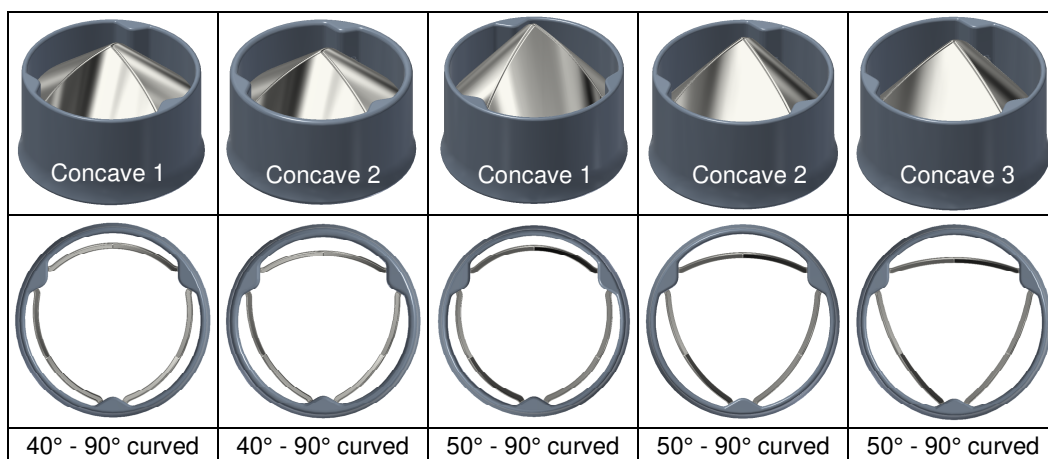
Figure 26:   Leaflet designs and configurations (2)

To address the leakage problem identified as a critical aspect in the FMECA, the use of a flexible synthetic material is suggested. If the leaflet edges are lined with a biocompatible elastomer or if the entire leaflet is covered, which could also improve the surface finish, a better seal will form upon closure. However, a durable and biocompatible flexible synthetic material does not currently exist. The silicone rubber of the occluder of a poppet valve, which is based on a similar concept as the ball-in-cage valve (§2.4.1), showed significant wear at the rigid-flexible material interface [7]. The combination of rigid and flexible materials in one valve was not investigated further in this study. Quality control and correct tolerance specifications are also necessary to reduce leakage.

3.2.2.5   Assembly

In industry, bileaflet valves are assembled by elastically deforming the housing, just enough to locate the leaflets in place. Assembly by deformation as well as two additional assembly methods were investigated. Figure 27 shows the alternative assembly methods, which are adequate for proof of concept purposes.

| Assembly method 1 | Assembly method 2 |
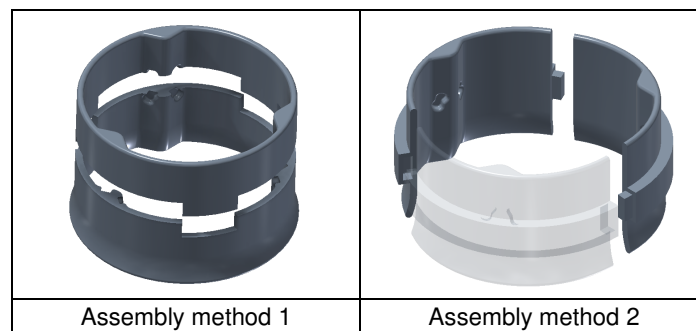
Figure 27:   Exploded view of alternative housing assembly methods

3.2.2.6   Materials

For prototype development, various materials and manufacturing methods were investigated. This is detailed in Appendix A.2. The limitations of AM in terms of dimensional accuracy and surface roughness were considered and deemed acceptable for prototyping. For the sake of reproducibility, cost- and time-efficiency, prototypes were developed using laser-based stereolithography (SLA) and titanium-based direct metal laser-sintering (DMLS). The test pieces are shown in Figure 28. The SLA parts were manufactured at *Build Volume* using a *Formlabs* Form 2 resin printer. The printer is capable of printing 20 µm layers. The density of the resin printed parts is approximately 1 270 kg/m^3, roughly half that of pyrolytic carbon. The DMLS parts were manufactured at CRPM. The density of the titanium parts is approximately 4 590 kg/m^3, roughly double that of pyrolytic carbon. Metal additive manufactured parts have very rough surfaces, therefore more extensive post-processing is required. For final product development, pyrolytic carbon, titanium and ceramic, were considered. The results are presented in §3.3.2.
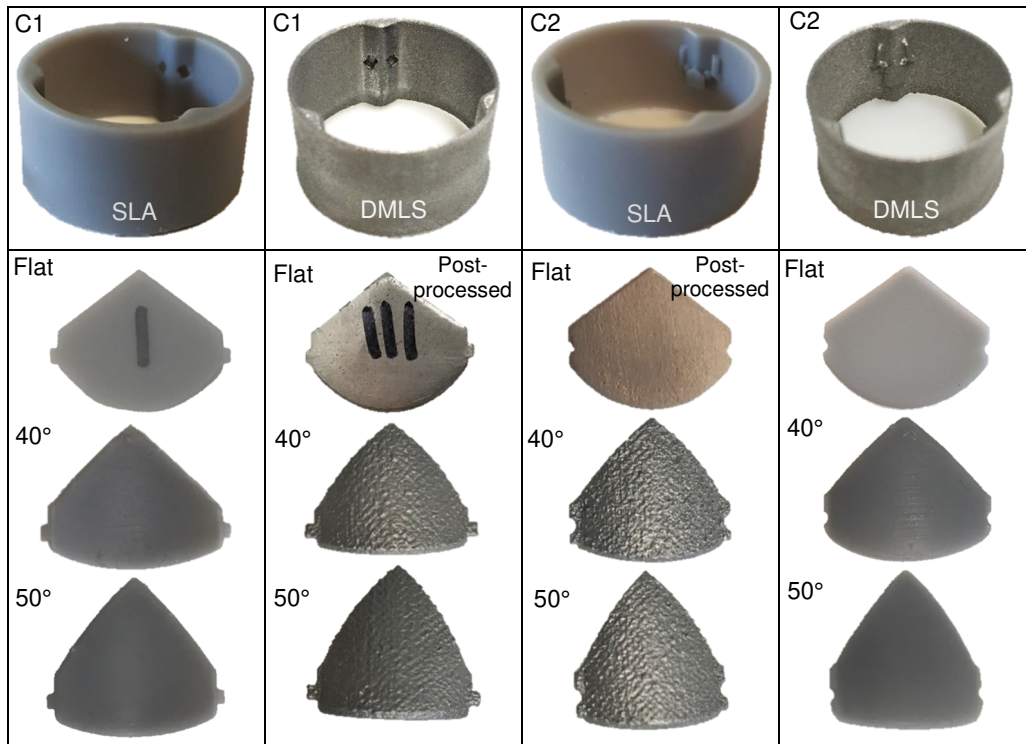
Figure 28:   SLA and DMLS test pieces

3.3   Concept Evaluation

3.3.1   Analytical Evaluation

First order calculations were performed to investigate the shear of the leaflet at the pivot ear under the diastolic backpressure as well as the impact force during closure (average closing times were taken from literature [45]). Large safety factors up to two orders of magnitude were calculated, even with conservative stress concentration factors. This indicates that the main mode of failure will more likely be as a result of leaflet fracture due to the presence of surface defects or material impurities that reduce the fatigue life. Calculations were corroborated with finite element methods (FEM).

Varying leaflet curvature, closed angle and hinge mechanism, resulted in 23 design configurations. Leaflet mass, geometry and dynamic properties were analysed and compared, relative to the bileaflet valve. The results are presented in Figure 29.

The mass of the leaflets of the trileaflet configuration is less than that of the bileaflet configuration. The lengths of the leaflet rotational arm (from the axis of rotation to the leaflet tip) are compared in Figure 29a, the moment of inertia (I) about the axis of rotation is shown in Figure 29b, torque (T) applied to the leaflets is shown in Figure 29c and the angular acceleration is shown in Figure 29d (calculations are based on Figure 24). Curvature modifies leaflet size and therefore affects the mass, length of the rotational arm and dynamic properties. Flat leaflets (indicated in cyan) are smaller and lighter and have a smaller moment of inertia. A smaller moment of inertia results in a faster moving leaflet if the magnitude of the applied

force remains constant. If the material of the trileaflet valve is changed to ceramic or titanium (from pyrolytic carbon), the moment of inertia will approximately double. Concavity (indicated in red) increases the valve profile height. The larger the radius of rotation, the higher the linear velocity of the leaflet tip. The torque applied to the concave curved leaflets with smaller radii of curvature is the greatest. The torque acting on the convex leaflets (indicated in green) will result in rotation in the wrong direction. Reducing the closed angle reduces the leaflet profile and overall size. Applied torque decreases as the leaflet's closed angle decreases. The trileaflet configurations result in a reduction in angular acceleration, with flat leaflets resulting in the greatest reduction. However, the centroid of the flat leaflets is close to the axis of rotation and the torque is small.

(a) Leaflet rotational arm

(b) Moment of inertia

(c) Torque $(T = \Sigma(PAn) \times r)$

(d) Angular acceleration $(\alpha = T/I)$

1	Bileaflet	9	40° - 90° concave 2; C1	17	30° - 90° convex; C2
2	20° - 90° flat; C1	10	50° - 90° concave 1; C1	18	40° - 90° flat; C2
3	30° - 90° flat; C1	11	50° - 90° concave 2; C1	19	40° - 90° concave 1; C2
4	30° - 90° concave 1; C1	12	50° - 90° concave 3; C1	20	40° - 90° concave 2; C2
5	30° - 90° concave 2; C1	13	20° - 90° flat; C2	21	50° - 90° concave 1; C2
6	30° - 90° convex; C1	14	30° - 90° flat; C2	22	50° - 90° concave 2; C2
7	40° - 90° flat; C1	15	30° - 90° concave 1; C2	23	50° - 90° concave 3; C2
8	40° - 90° concave 1; C1	16	30° - 90° concave 2; C2		

Figure 29: **Comparison of the physical and dynamic properties of leaflets**

3.3.2 Numerical Evaluation

A first order linear static finite element analysis (FEA) was conducted on a single leaflet to verify the structural integrity of the leaflet under the backpressure load during diastole. The analysis was conducted with the use of *MSC Patran* 2018.0.3 and *Nastran* 2018.1. The assumption of linearity is valid for closed leaflets where the structure is rigid enough such that only small deformations are expected under the working load. The leaflet configurations that were modelled are the 40° - 90° flat, 40° - 90° concave 1 and 50° - 90° concave 1 with the C1 type hinge. The C1 type hinge is at greater risk of fracture than the C2 type hinge.

Leaflet geometries were simplified by omitting rounds and fillets, except at the leaflet ears. Eight-noded hexagonal elements (average size of 0.1 mm) were used to model the geometry. The total number of elements ranged from 150 000 – 200 000. The leaflets were constrained in all degrees of freedom at the leaflet ears, on the surface in contact with the hinge stop. A uniform pressure of 120 mmHg (16 kPa) was applied to the downstream surface. Figure 30 shows the FEA model, loads and boundary conditions.

Uniform pressure
(120 mmHg)

Fixed
constraint

| (a) Discretised FEA model | (b) Boundary conditions |
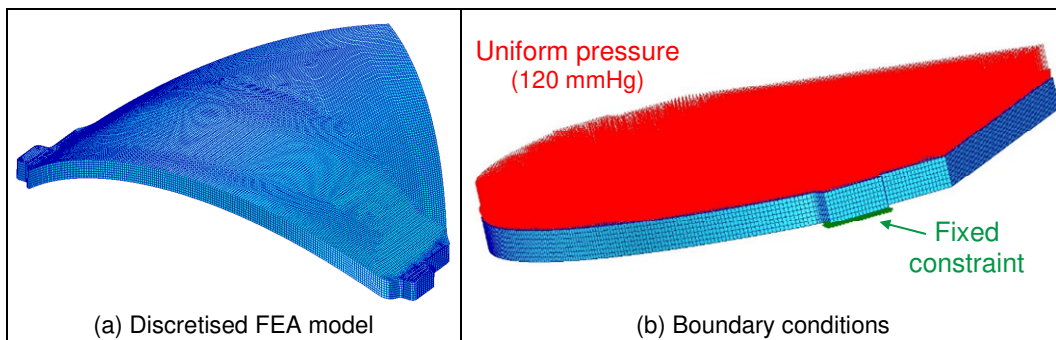
Figure 30:   3D FEA model of the leaflets

The material was modelled as an isotropic linear elastic material. Material properties of pyrolytic carbon, alumina and titanium (specifications from CRPM) are listed in Table 7.

Table 7: FEA material properties

Property	Pyrolytic carbon	Alumina (Al_2O_3)	Titanium (Ti)
Young's modulus [GPa]	30	392	110
Poisson's ratio	0.2	0.22	0.33
Tensile strength [MPa]	200	637	929
Flexural strength [MPa]	494	1274	-
Yield strength [MPa]	-	-	763

The results are summarised in Table 8. The maximum leaflet tip deflection (δ), von Mises stress (σ_v), major (σ_1) and minor (σ_2) principal stresses and the maximum shear stress theory (MSST) results are listed. In Figure 31, only the von Mises stress results are presented (note the units are Pascal). These results are the most

conservative, but the other stresses showed similar stress contour patterns. Maximum stress occurs at the top corner of the leaflet ear on the upstream surface.

Table 8: Summary of FEA results

Leaflet design	No. of elements	δ [mm]	σ_v [MPa]	σ_1 [MPa]	σ_2 [MPa]	MSST [MPa]
40° - 90° Flat	147 560	0.02	94	24	4	49
40° - 90° Curved	164 336	0.02	131	86	10	70
50° - 90° Curved	198 752	0.04	212	156	21	114

(a) 40° - 90° Curved leaflet   (b) 50° - 90° Curved leaflet
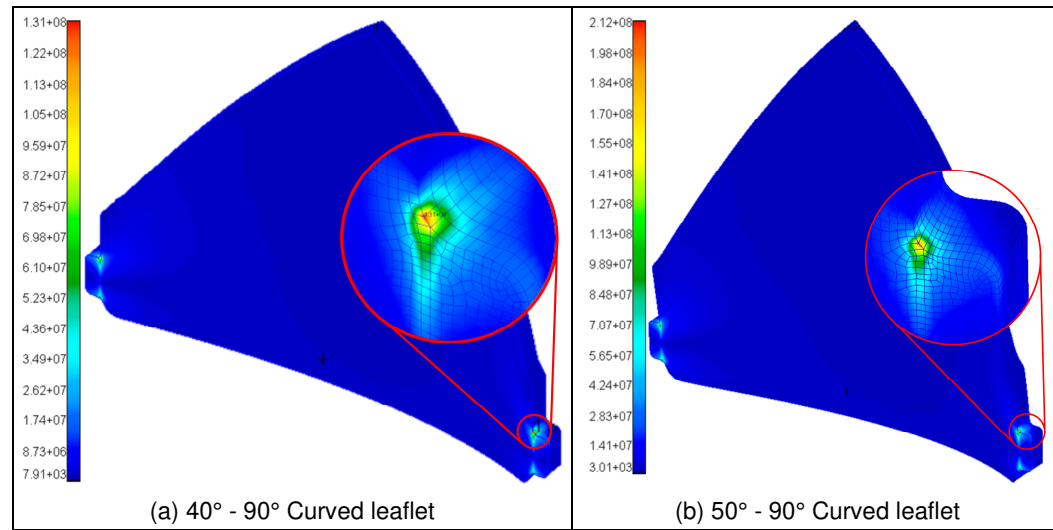
Figure 31: FEA von Mises stress results

The results show that the maximum principal stresses are below the tensile strength of the brittle materials. The safety factors for pyrolytic carbon leaflets range from 8.3 for the flat leaflet to 1.3 for the 50° curved leaflet. The safety factors for alumina leaflets range from 26.5 for the flat leaflet to 4.1 for the 50° curved leaflet. This implies that the material will not fracture. If the von Mises stress failure criterion is used, the peak stress results indicate that pyrolytic carbon is not strong enough. The safety factor for the flat leaflet is 2.1 and the von Mises stress of the 50° curved leaflet exceeds the tensile strength of the material. However, the findings indicate that alumina or titanium will result in much higher safety factors. The stress results are conservative considering the peak stress occurs at a single node, which skews the results. Calculating the average high stress over the cross-sectional area might be more realistic / less conservative. However, even without averaging, alumina or titanium meet the safety requirements. The maximum leaflet deflection is acceptable. Based on the literature review and FEA results, either biocompatible alumina or titanium is recommended for product development. The strength of these materials could ultimately lead to a decrease in leaflet thickness resulting in less obstruction to the flow.

3.3.3 Initial Experimental Evaluation

Preliminary pulsatile flow tests were conducted to evaluate whether the design concepts meet the functional requirements listed in §3.1.3.1. The test results were used to determine which valve configuration(s) should be selected for final prototype testing to evaluate whether the valves meet the performance requirements listed in §3.1.3.2. Final prototype testing is explained in §4, which includes a detailed description of the test setup. The secondary aim was to assess the manufacturing methods and whether the material and manufacturing requirements (listed in §3.1.3.3 and §3.1.3.4 respectively) for prototype development purposes are satisfied. The SLA and DMLS manufactured valves and a combination of the AM methods (e.g. SLA housing with DMLS leaflets) were tested. All the leaflet configurations and various housings were tested. This refers to SLA housings fabricated with different resins, DMLS housings, housings with through and blind holes at the C1 type hinges, shorter housings (with reduced downstream length) and the 80°, 85° and 90° maximum open angle configurations. The observations of the preliminary experimental evaluation are summarised Table 9.

Table 9: Prototype evaluation results

Description	Image	Comments	Description	Image	Comments
19 mm Commercial bileaflet valve		Considerable flutter.	50° - 90° concave 1; C1		SLA valve. Larger opening than flat leaflets and 40° - 90° curved.
25 mm Commercial bileaflet valve		Less flutter than the 19 mm valve.	50° - 90° concave 2; C1		SLA valve. Less opening than 50° - 90° concave 1; C1.
Bileaflet		SLA valve. Some flutter.	50° - 90° concave 3; C1		Smaller opening than 50° - 90° concave 2; C1.
Bileaflet		SLA valve. Through holes at hinges. Partial opening.	20° - 90° flat; C2		SLA valve. Partial opening. Similar results for DMLS valve.
Bileaflet		DMLS valve. Considerable flutter. Leaflets opening > 90°. Closing failure.	30° - 90° flat; C2		SLA valve. Partial opening. Similar results for DMLS valve.
20° - 90° flat; C1		SLA valve. Partial opening.	30° - 90° concave 2; C2		SLA valve. Partial opening; more than flat leaflets. Various housings tested.

Table 9: Prototype evaluation results (continued)

Description	Image	Comments	Description	Image	Comments
30° - 90° flat; C1		SLA valve. Partial opening; more than 20° - 90° flat; C1.	40° - 90° flat; C2		SLA valve. Partial opening more than 30° - 90° flat; C2.
30° - 90° concave 1; C1		SLA valve. Partial opening; more than flat leaflets.	40° - 90° flat; C2		DMLS valve. Partial opening.
30° - 90° concave 2; C1		SLA valve. Similar results to 30° - 90° concave 1; C1. Various housings tested.	40° - 90° concave 1; C2		SLA valve. Larger opening than flat leaflets.
40° - 90° flat; C1		SLA valve. Partial opening; more than 30° - 90° flat; C1.	40° - 90° concave 2; C2		SLA valve. Less opening than 40° - 90° concave 1; C2.
40° - 90° flat; C1		DMLS valve. Partial opening. Various housings and SLA leaflets tested.	50° - 90° concave 1; C2		SLA valve. Larger opening.
40° - 90° concave 1; C1		SLA valve. Larger opening. Various housings and DMLS leaflets tested.	50° - 90° concave 2; C2		SLA valve. Less opening than 50° - 90° concave 1; C2.
40° - 90° concave 2; C1		SLA valve. Less opening 40° - 90° concave 1; C1. Various housings and DMLS leaflets tested.	50° - 90° concave 3; C2		SLA valve. Less opening 50° - 90° concave 2; C2.

The main conclusions were:

- Larger closed angles and leaflet curvature promoted opening, corresponding with Figure 29.
- SLA valves performed better than DMLS valves, largely due to the imprecision of the DMLS manufacturing method. The limitations of the method resulted in rough surfaces and out of bound tolerances. This either resulted in loose fits, with excessive leaflet flutter, over-opening / closing, leaflet misalignment and leaflet escape, or very tight fits. Quality control and repeatability of manual post-processing methods were poor.
- Differences in results between C1 and C2 type hinges were not observed.
- Leaflet flutter and asymmetrical leaflet motion were observed. The motion of each individual leaflet was influenced by the other leaflets.
- Valve orientation in the physical test setup did not influence the results.
- The leaflets were able to close with the 90° open angle design.

3.4 Prototype Development

The results of the simplified systems approach were used to analyse the initial test results to select the final trileaflet prototype design(s). Table 10 shows whether the test valves satisfy the functional, material and manufacturing requirements.

Table 10: Requirements analysis and evaluation (1)

Legend:
- ✔ (green) Full compliance
- ✔ (orange) Partial compliance
- ✗ (red) No compliance

Description	Requirement		
Functional requirements (§3.1.3.1)	**i**	**ii**	**iii**
20° - 90° flat; C1	✗ (red)	✔ (green)	✔ (green)
30° - 90° flat; C1	✗ (red)	✔ (green)	✔ (green)
30° - 90° concave 1; C1	✔ (orange)	✔ (green)	✔ (green)
30° - 90° concave 2; C1	✔ (orange)	✔ (green)	✔ (green)
40° - 90° flat; C1	✗ (red)	✔ (green)	✔ (green)
40° - 90° concave 1; C1	✗ (red)	✔ (green)	✔ (green)
40° - 90° concave 2; C1	✔ (orange)	✔ (green)	✔ (green)
50° - 90° concave 1; C1	✔ (green)	✔ (green)	✔ (orange)
50° - 90° concave 2; C1	✔ (orange)	✔ (green)	✔ (orange)
50° - 90° concave 3; C1	✔ (orange)	✔ (green)	✔ (orange)
20° - 90° flat; C2	✗ (red)	✔ (green)	✔ (green)
30° - 90° flat; C2	✗ (red)	✔ (green)	✔ (green)
30° - 90° concave 1; C2	✔ (orange)	✔ (green)	✔ (green)
30° - 90° concave 2; C2	✔ (orange)	✔ (green)	✔ (green)
40° - 90° flat; C2	✗ (red)	✔ (green)	✔ (green)
40° - 90° concave 1; C2	✔ (green)	✔ (green)	✔ (green)
40° - 90° concave 2; C2	✔ (orange)	✔ (green)	✔ (green)
50° - 90° concave 1; C2	✔ (green)	✔ (green)	✔ (orange)
50° - 90° concave 2; C2	✔ (orange)	✔ (green)	✔ (orange)
50° - 90° concave 3; C2	✔ (orange)	✔ (green)	✔ (orange)
80° maximum opening hinge	✗ (red)	✔ (green)	✔ (green)
85° maximum opening hinge	✗ (red)	✔ (green)	✔ (green)
C1 through hole	✗ (red)	✔ (green)	✔ (green)
C1 blind hole	✔ (green)	✔ (green)	✔ (green)
Material requirements (§3.1.3.3)	**i**	**ii**	**iii**
Titanium	✔ (orange)	✔ (green)	✔ (green)
Plastic	✗ (red)	✗ (red)	✔ (green)
Manufacturing requirements (§3.1.3.4)	**i**	**ii**	**-**
DMLS	✗ (red)	✗ (red)	
SLA	✔ (orange)	✔ (orange)	

Table 10 indicates that the curved leaflets meet the functional requirements, specifically leaflets with a smaller radius of curvature. Valves with flat leaflets do not meet all the functional requirements. The SLA fabricated valves are suitable for prototyping purposes, both in terms of material and manufacturing requirements. Although the manufacturing requirements are only partially satisfied, SLA offered a better solution than DMLS.

Because a difference between the C1 and C2 type hinges was not observed, final prototypes of both hinge mechanisms were developed. The valve's ability to open is a critical functional requirement. The greater the extent of opening, the less the flow obstruction and the larger the EOA. The 50° concave 1 valves showed the best performance in this regard. The sweep angle of these valves is small, resulting in a smaller closing volume. However, these are high profile valves. The leaflets could interfere with nearby anatomical structures and, due to the larger surface area, the total wall shear stress and platelet exposure time to stress will be greater. The 30° concave 1 leaflets are small, but they do not open fully and have a larger sweep angle.

Based on Table 10, the following prototype valves were manufactured (shown in Figure 32):

- 40° - 90° concave 1; C1 valve (referred to as 40° trileaflet 1).
- 40° - 90° concave 1; C2 valve (referred to as 40° trileaflet 2).
- 50° - 90° concave 1; C1 valve (referred to as 50° trileaflet 1).
- 50° - 90° concave 1; C2 valve (referred to as 50° trileaflet 2).
- Reference / benchmark bileaflet valve for more accurate comparisons.

(a) 40° Trileaflet 1	(b) 40° Trileaflet 2	(c) 50° Trileaflet 1	(d) 50° Trileaflet 2	(e) Bileaflet
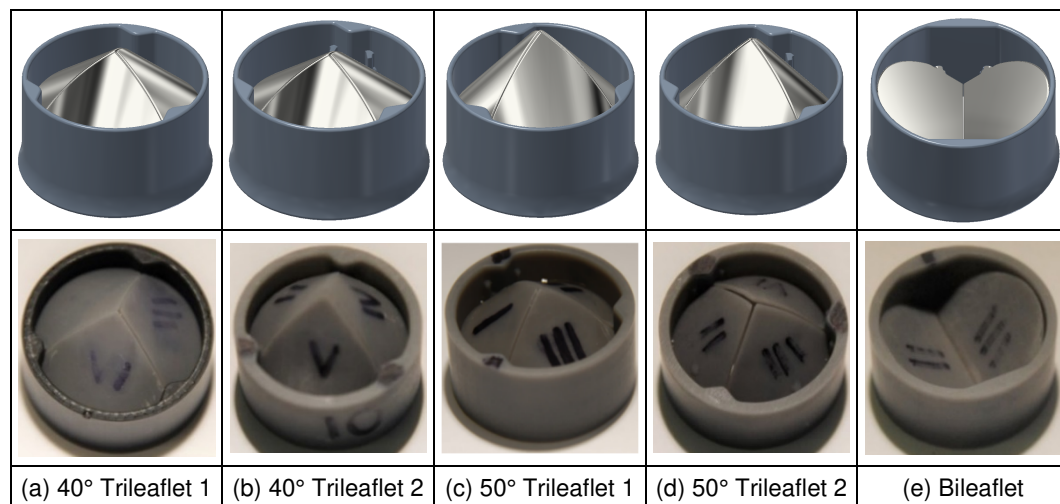
Figure 32:   Final prototype valves

4   EXPERIMENTAL EVALUATION

The hydrodynamic characteristics of the prototype heart valves were studied experimentally to analyse and compare the various designs. In addition to the five valves shown in Figure 32, a 24 mm supra-annular *Medtronic* Open Pivot AP360 aortic bileaflet valve (S/N 648430) [135] was tested. The valve has an internal diameter of 22.8 mm^2, similar to that of the prototype valves, and a sweep angle of 60° (25° - 85°). The valve has pyrolytic carbon coated graphite leaflets. The commercial valve is the only valve that can accurately be compared to published results. The commercial valve results were used to confirm the test methodology and valve behaviour.

4.1   Pulsatile Flow Tests

The tests were conducted using a commercial *Vivitro Labs Inc*. Cardiac Pulse Duplicator (CPD). *Mathworks Matlab* R2018a was used for post-processing.

4.1.1   Experimental Setup

The experimental setup is displayed in Figure 33. The setup consisted of the CPD left heart model (S/N 4060), a viscoelastic impedance adapter (VIA) (S/N 7028), an electronically controlled pump and a data acquisition system. A flexible silicone membrane simulates the ventricle and silicone rubber tubes represent the arterial system. All the other components of the system are rigid (acrylic plastic).
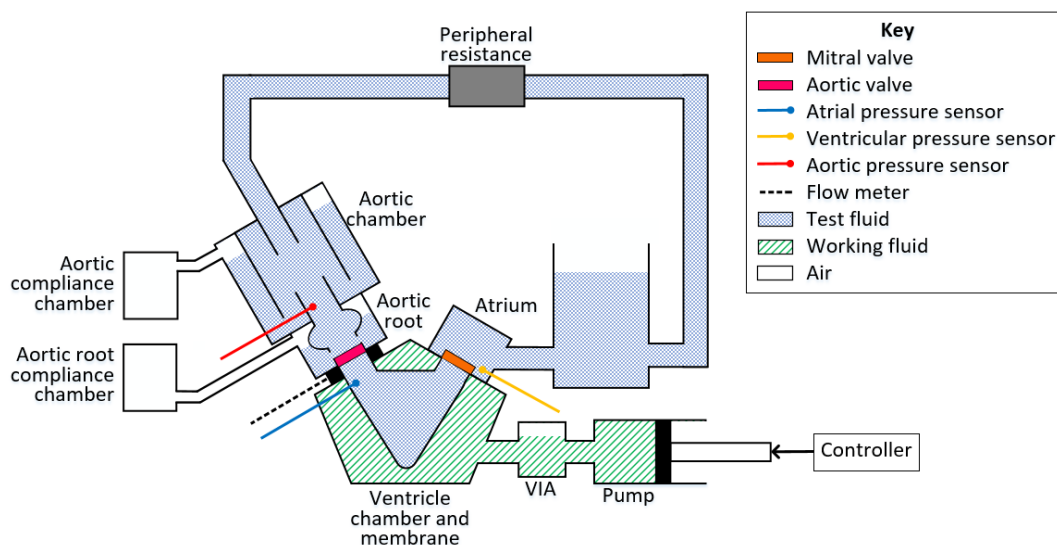
Figure 33:   Schematic of the CPD experimental test setup

The VIA regulates the preload. The aortic- and aortic root compliance chambers and peripheral resistance setting regulate the afterload [136]. Preload affects the ventricle's ability to expand as the internal pressure increases [92], which is simulated in the experimental setup with the use of the VIA's compliance chambers. Afterload refers to the resistance that must be overcome to eject blood from the ventricle.

Preload and afterload conditions are not explicitly defined in ISO 5840. A study was conducted to investigate the effect of preload on CPD test results. The results of the study were presented in a poster format at the Heart Valve Society's (HVS) annual scientific meeting in Spain in April 2019 [137]. It was observed that preload mainly affects the regurgitant volume. A second poster was also exhibited at the conference [138]. Further CPD studies have been embarked on to improve the understanding of the physical test setup and whether a numerical model can be used to replicate the results. The work conducted has contributed to an abstract that has been accepted for a plenary presentation [139].

4.1.2 Experimental Procedure

The test protocol was based on the ISO 5840 guidelines [3].

i. The pressure sensors were calibrated prior to testing and the pulse duplicator's pump was used to validate the flow meter. The pump was calibrated by *Vivitro Labs* upon acquisition.

ii. The test valves were mounted in the aortic position with a non-tilting disc valve in the mitral position.

iii. The tests were conducted at room temperature.

iv. The test fluid was a 0.9% saline-glycerine solution (3:2 mass ratio), with a density of 1 090 kg/m^3 and viscosity of 3.58 cP [110, 140 – 142].

v. A waveform (supplied by *Vivitro Labs*), mimicking a physiological cardiac waveform with a systolic duration of 35% was specified as input to the pump.

vi. The valves were tested at five operating conditions, listed in Table 11, based on conditions described in [7]. The net CO cannot directly be controlled in the physical setup; therefore, some variation exists (standard deviation is indicated).

Table 11: CPD test conditions

Test no.	Heart rate [bpm]	Piston SV [mL]	Net CO [L/min]	Quantity	Physiological State
1	60	80	3.28 ± 0.47	20	Resting
2	70	90	4.40 ± 0.51	20	Minimal effort
3	80	100	5.70 ± 0.44	20	Moderate effort
4	100	105	7.41 ± 0.22	20	Exercise
5	120	110	9.31 ± 0.27	20	High intensity sustained effort

vii. The valves were tested under normotensive conditions. Systolic and diastolic pressures were set to 120/80 ± 5 mmHg by adjusting the afterload. MAP was 100 ± 5 mmHg.

viii. A VIA was installed at the pump-ventricle chamber interface. The VIA source compliance chamber contained 60 mL air and the output compliance chamber contained 45 mL air. The working fluid section of the test setup was otherwise de-aerated.

ix. For each test condition, measurements were recorded over 20 cardiac cycles, at a frequency of 256 samples per cycle. The average results were used to calculate the performance indicators.

4.1.3   Results

Figure 34 shows the typical ventricular and aortic pressure and aortic flow rate waveforms. Waveforms for all the tests are displayed in Appendix C.1 (Figure 87 to Figure 93). The measured average output parameters are shown in Appendix C.1 (Figure 94). The output parameters confirm that the tests were conducted under approximately equivalent cardiac conditions and within the ISO 5840 specifications.

(a) Bileaflet valve   (b) 40° Trileaflet 1 valve
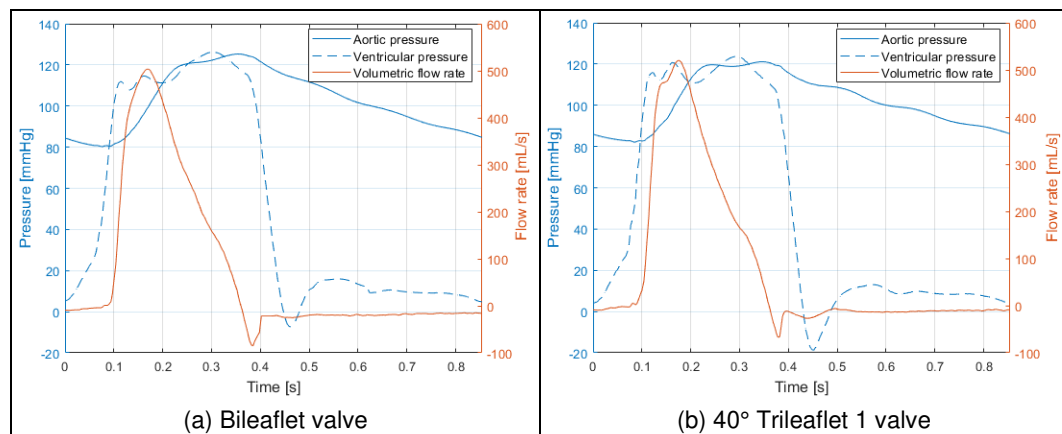
Figure 34:   Pressure and flow waveforms for Test 2 (CO ≈ 5 L/min)

Key performance parameters are plotted in Figure 35 and Figure 36. As the flow rate (Q_{rms}) and CO increased, the transvalvular pressure drop increased. The relationship is linear up to the highest flow rate, where a significant increase is observed. EOA is expected to remain relatively constant. A small increase in EOA is seen as CO increased. At the highest flow rate there was a sudden decrease in EOA, which is as a result of the inverse relationship between the pressure gradient and EOA. The regurgitant fraction decreased as CO increased.

(a) Pressure drop   (b) Q_{rms}
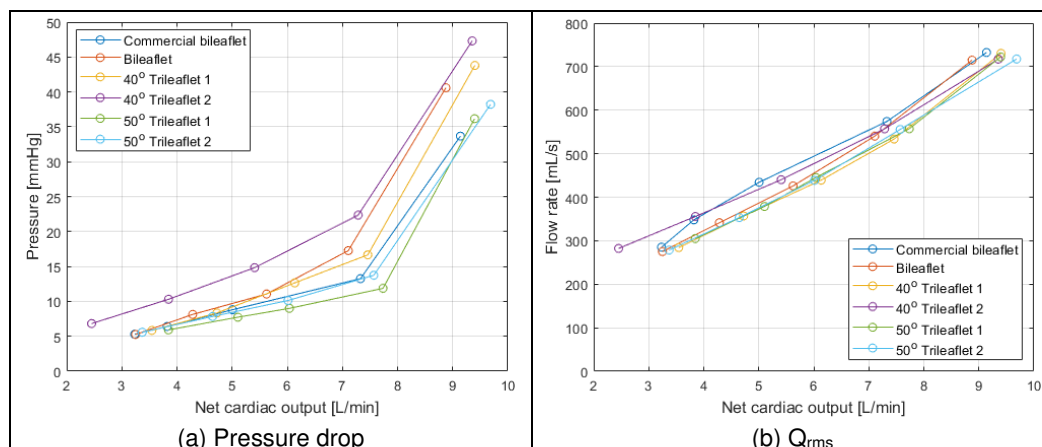
Figure 35:   Average test performance indicators as a function of CO (1)
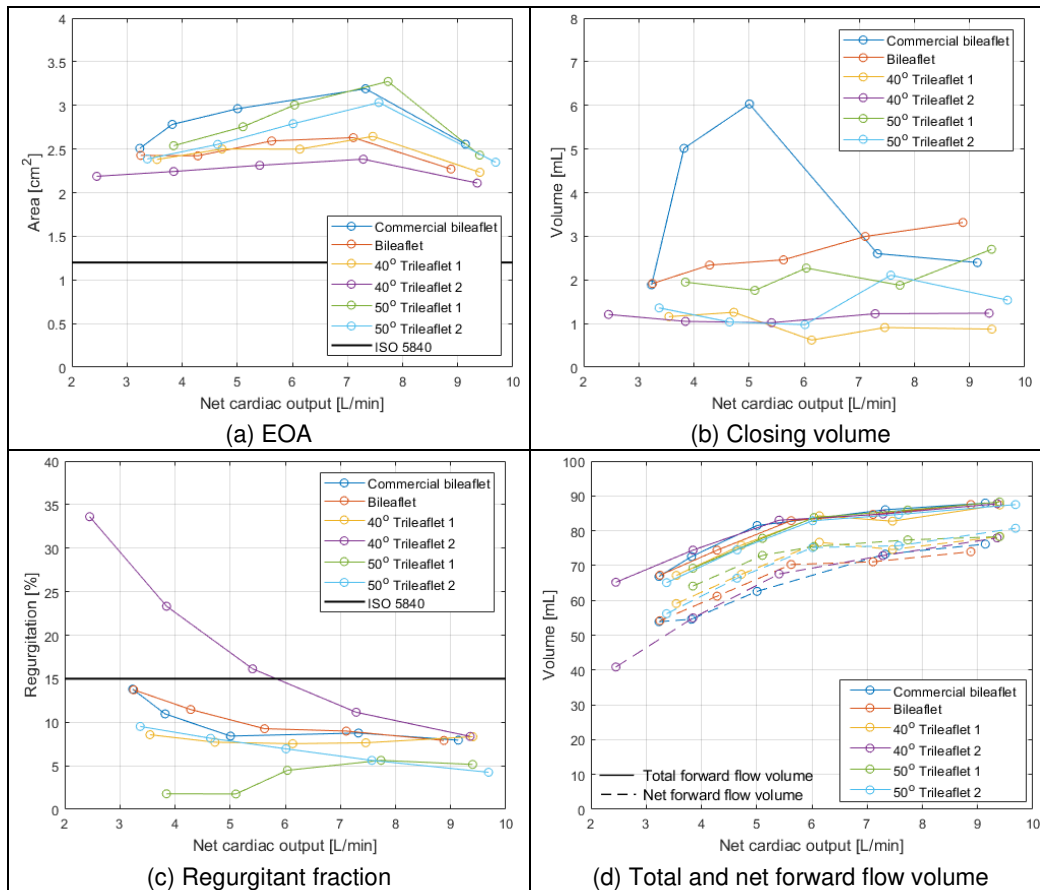
Figure 36: Average test performance indicators as a function of CO (2)

4.1.4 Discussion

Figure 35 and Figure 36 confirm that the test valves had comparable outcomes to the commercial valve. The only difference observed was a greater closing volume for the commercial valve, due to a larger sweep angle.

The pressure drop across the valves increased with CO (Figure 35a). The trileaflet valves, except the 40° trileaflet 2 valve, performed better than the benchmark bileaflet valve. The 50° trileaflet valves had the lowest pressure drop. The 40° trileaflet 2 valve had the highest pressure drop, especially at low flow rates. At higher flow rates, the pressure drop is comparable to that of the benchmark valve (3% difference at the highest flow rate). The larger pressure drop at lower flow rates is attributed to the large regurgitant fraction at low flow rates (Figure 36c). Figure 36b shows that the closing volume of the 40° trileaflet 2 valve was similar for all flow rates, but Figure 36d shows a large difference between the total and net flow rates. This implies that at low flow rates, the valve had more leakage. This is also evident in the flow waveform results in Appendix C.1. Due to leakage, the 40° trileaflet 2 valve had a lower net CO compared to the other valves despite operating at the same conditions.

Rigid mechanical HVRs result in larger pressure gradients than native valves [143]. Native heart valves allow for aortic expansion during systole, which reduces the pressure drop [14]. Rigid HVRs change the anatomy of the aortic root and constrain vessel motion, affecting the normal physiology. The experimentally measured pressure drop increased with CO because the valve was mounted in a rigid system that did not allow for any expansion or pressure relief at higher flow rates. The clinically measured pressure drop of the commercial valve is 11.1 ± 0.8 mmHg, with values ranging from 3.2 – 26.0 mmHg [144]. The cardiac condition at which the pressure drop was measured is not specified; however, the range is large. Except for the highest CO, the measured values fall within this range. The *in vitro* pressure gradients of various 25 mm aortic bileaflet valves are listed in [145]. The average pressure drop at ~ 5 L/min CO is 7 mmHg. In [98], the *in vitro* pressure drop of a 25 mm *SJM* bileaflet valve is specified as 5.0 ± 2.8 mmHg at 5 L/min CO and 5.2 ± 3.8 mmHg at 7 L/min CO. In [118], average experimental pressure drops of 18 – 20 mmHg at 7 L/min CO were measured for 21 mm bileaflet valves. Although smaller valves result in larger pressure gradients, a wide range of experimentally measured values is reported in literature. The experimental results from this study are comparable to some of the literature sources or fall within the reported range. The values from literature highlight the variation in CPD test results and reaffirm the necessity of a reference valve.

The large increase in the pressure gradient at the highest CO can be explained by the pressure waveforms and the pressure gradient calculation. The pressure drop is the average pressure difference across the valve during forward flow, for the duration that the pressure difference is positive. The 40° trileaflet 1 valve is shown as an example in Figure 37; the other valves exhibited similar behaviours. At low flow rates, the duration for which the pressure difference was positive was ~ 200 ms (indicated in red in Figure 37a). At high flow rates, the duration was much shorter, ~ 100 ms (indicated in red in Figure 37b). The pressure difference is larger because it is averaged over a shorter period. The ventricular pressure waveform in Figure 37b shows that the valve closed later (indicated in green in Figure 37b). Despite the initial drop, the ventricle maintained a lower pressure, which signifies that the total open angle of the valve decreased, but the valve remained open for ~ 150 ms. It may be more accurate to calculate the average pressure drop over the longer period, but this is not how pressure drop is defined in ISO 5840.

(a) 40° Trileaflet 1 (CO ≈ 5 L/min)　　　(b) 40° Trileaflet 1 (CO ≈ 9.5 L/min)
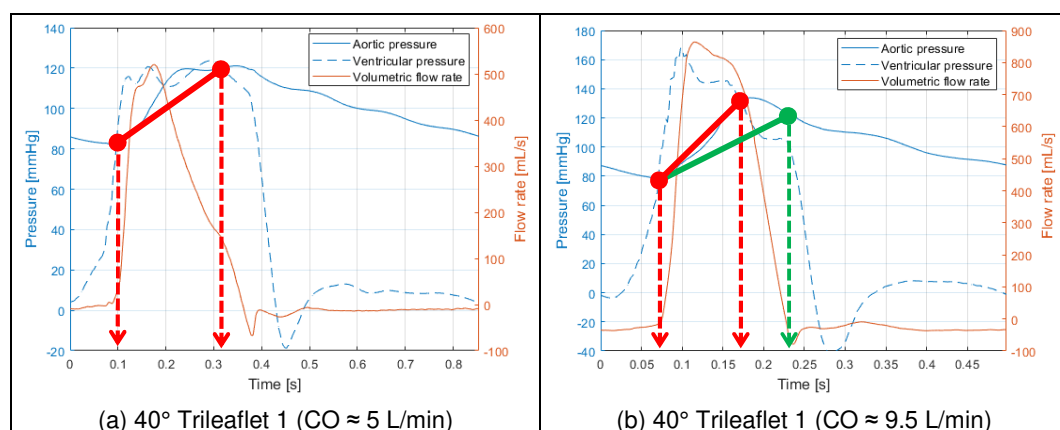
Figure 37:　　Difference in pressure drop at low and high flow rates

The EOAs of all the valves at all flow rates exceed the minimum ISO 5840 requirement of 1.2 cm^2 (Figure 36a). The EOA of the 50° trileaflet valves is larger than the benchmark bileaflet valve. The EOA of the 40° trileaflet 1 valve closely matches that of the bileaflet valve. The 40° trileaflet 2 valve has the lowest EOA. The EOA results correspond with the pressure drop results. EOAs of 1.98 – 2.5 cm^2 for 25 mm mechanical HVRs are considered normal [22]. The clinically measured EOA of the commercial valve is 2.1 ± 0.1 cm^2, with values ranging from 1.0 – 4.9 cm^2 [144]. The *in vitro* results agree with the clinical results. The EOA results also correlate with the results of a series of *in vitro* tests conducted on a 25 mm bileaflet valve [98]. EOAs ranging from 2.2 – 3 cm^2 are reported in the study. Other values from literature based on *in vitro* studies are listed in Table 4. The measured EOA values fall within the bileaflet range, with the lower profile valves on the lower end and the higher profile valves on the higher end.

The valves generally did not have large closing volumes (Figure 36b). However, the bileaflet valve had a larger closing volume than the trileaflet valves. The valves demonstrate similar trends as CO increased.

All the valves, except the 40° trileaflet 2 valve, meet the ISO 5840 specification of 15% maximum regurgitation at all flow rates (Figure 36c). The 40° trileaflet 2 valve had more leakage at lower flow rates. The likely causes are leaflet misalignment or incomplete closure at low flow rates due to manufacturing inaccuracies. However, at higher flow rates, the ISO 5840 requirement is satisfied. The regurgitant fraction results of the other trileaflet valves were lower than that of the bileaflet valves. Figure 36d shows the total regurgitation. At CO ≈ 5 L/min, the 40° trileaflet 2 valve has the largest regurgitation of 18.4 mL/beat. The commercial bileaflet valve and the benchmark bileaflet valve have regurgitant volumes of 13.0 mL/beat and 10.9 mL/beat respectively. The other three trileaflet valves have 3.1 – 7.1 mL/beat regurgitation. The regurgitant volume of the bileaflet valves compares well with the *in vitro* values reported in literature (refer to Table 4). The prototype trileaflet valves compare favourably with the bileaflet results reported in literature and correspond with the regurgitation of native heart valves.

There was not a distinct effect of the hinge mechanism on the overall valve performance. In some cases, it was observed that the C1 type valves slightly outperformed the C2 type valves. The 50° trileaflet valves generally outperformed the 40° trileaflet valves, at least in terms of the parameters measurable with the CPD. The poor performance of the 40° trileaflet 2 valve is more likely as a result of manufacturing inaccuracies than poor design. This is deduced from the fact that the leaflet design is the same as the 40° trileaflet 1 valve and the hinge design is the same as the 50° trileaflet 2 valve. Both the 40° trileaflet 1 and the 50° trileaflet 2 valves performed well. Besides the 40° trileaflet 2 valve, the prototype trileaflet valves performed better than the benchmark bileaflet valve. The performance of the valves is even comparable to the commercial valve, despite the manufacturing and quality control shortfalls.

During testing, another observation was made that is not reflected in the performance indicators. Leaflets of the bileaflet valve fractured at the pivot point (refer to Figure 38), mainly at higher flow rates. It is acknowledged that the test valves were fabricated using a less rigid material, resulting in more deformation

than what commercial valves would experience. None of the leaflets of the trileaflet valves fractured, suggesting that trileaflet valves are less susceptible to fatigue failure regardless of the material. A longer leaflet fatigue life implies that the thickness can be reduced without comprising safety. This will present less obstruction to flow, increasing the EOA.

Figure 38:   Photographs of the fractured bileaflet valve leaflets

4.2   Imaging Techniques – High-Speed Video

The flow tests were combined with high-speed video (HSV) analysis for two of the test conditions (conditions two and five listed in Table 11). The videos were analysed to determine the leaflet motion and to calculate the opening and closing speeds. The aim was to determine whether the prototype trileaflet valves have slower closing velocities than the bileaflet valve and to specify the recorded leaflet motion as input to the prescribed kinematics CFD analysis. The test results were analysed using an open source video analysis tool, *Tracker* 5.1.0 [146].

4.2.1 Experimental Setup

A high-speed camera system was added to the existing experimental setup. Essentially, the setup and procedure remained identical to that described in §4.1. The complete setup, shown in Figure 39, consisted of the *Vivitro* CPD, an *Olympus i-SPEED TR* high-speed camera (S/N 13000291) and additional lighting.
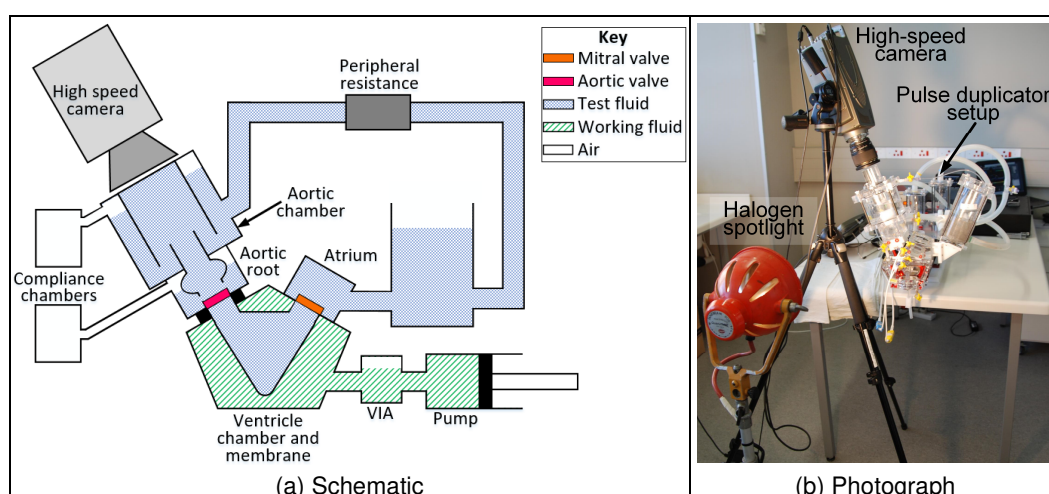
Figure 39:   Experimental HSV test setup

4.2.2 Experimental Procedure

The same test protocol as described in §4.1.2 was followed. Additional test parameters are defined below.

i. The camera captured 1 000 frames per second (fps) at a resolution of 1280 × 1024 pixels. The camera was positioned with its axis perpendicular to the horizontal plane of the valve.

ii. The tests are summarised in Table 12. Videos were recorded for 10 cycles at each test condition. The average results were used for post-processing.

Table 12: HSV test conditions

Test no.	Heart rate [bpm]	Piston SV [mL]	Net CO [L/min]	Quantity	Physiological State
1	70	90	4.40 ± 0.51	10	Minimal effort
2	120	110	9.31 ± 0.27	10	High intensity sustained effort

iii. Leaflet tips were selected as the target for motion tracking. The tips and edges were marked to enhance contrast and assist in locating the target.

iv. Velocity was calculated during post-processing. The target was manually located in each consecutive frame. The distance (in pixels) between the initial location of the target and the instantaneous location was determined.

v. A calibration factor was calculated to convert pixels to physical units using reference lengths with known dimensions. Several reference dimensions were used to reduce the error of the calibration factor. Reference dimensions included valve diameter, leaflet edge length, leaflet hinge-to-hinge width and diameter of the pulse duplicator interface. Calibration was done in the plane of the valve, with the maximum vertical difference between the calibration plane and plane of motion occurring when the leaflets were in the fully open position.

vi. Using the calibration factor, the target's position, displacement and velocity were calculated (only for the systolic portion of the cardiac cycle).

4.2.3 Results

The procedure described in §2.6.2 was followed to quantify the maximum experimental uncertainty error. Dimensional calibration errors were estimated to be 2 pixels and 0.5 mm. The vertical out-of-plane error was specified as the height of the leaflet tips of the 50° trileaflet valves in the open position. A conservative γ error of 10° was assumed. During post-processing, motion blur was not identified as a problem. Motion blur was observed in some cases, but it did not obscure the target. A motion blur error of 1 pixel was assumed. The valve was located at the centre of the image and the valve's axis was aligned with the camera's axis; distortion was not observed. The precision of the camera's chronometer could not be determined. The same uncertainty error specified in [103] was used as the chronometer uncertainty so as not to neglect its contribution to the total error. For this experiment, the main sources of uncertainty error were the calibration and γ uncertainties. With conservative uncertainty estimates, the total error is 6.4%.

The HSV results are presented in Figure 40 to Figure 44. The motion of the trileaflet valves is compared to that of the bileaflet valve, in terms of maximum open orifice and leaflet velocity. The average displacement over 10 cycles is indicated with a solid line; standard deviation is indicated with dashed lines. Images of the trileaflet valves, corresponding to the times indicated with vertical lines, are also shown (representative cycles were selected for rendering).

(a) Bileaflet vs 40° trileaflet 1 (CO ≈ 5 L/min)   (b) Bileaflet vs 40° trileaflet 1 (CO ≈ 9.5 L/min)
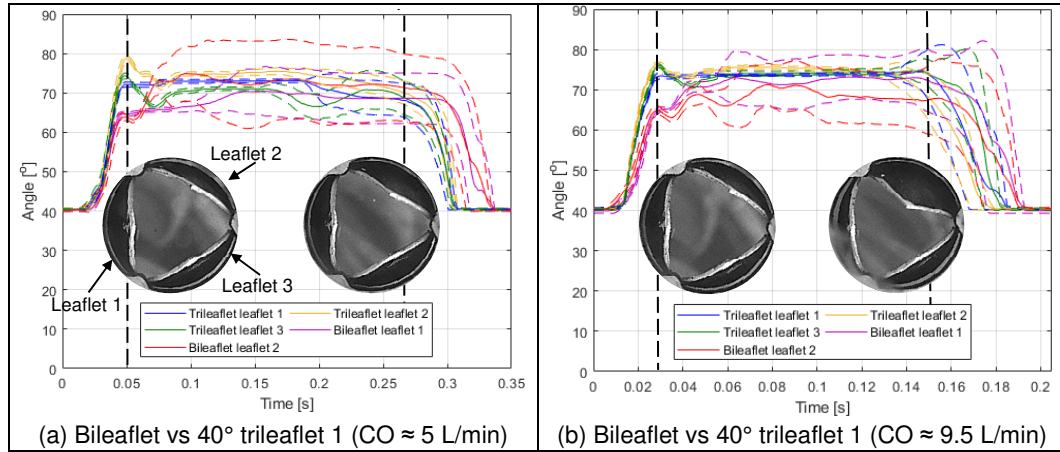
Figure 40:   Comparison between bileaflet and 40° trileaflet 1 valve motion

(a) Bileaflet vs 40° trileaflet 2 (CO ≈ 5 L/min)   (b) Bileaflet vs 40° trileaflet 2 (CO ≈ 9.5 L/min)
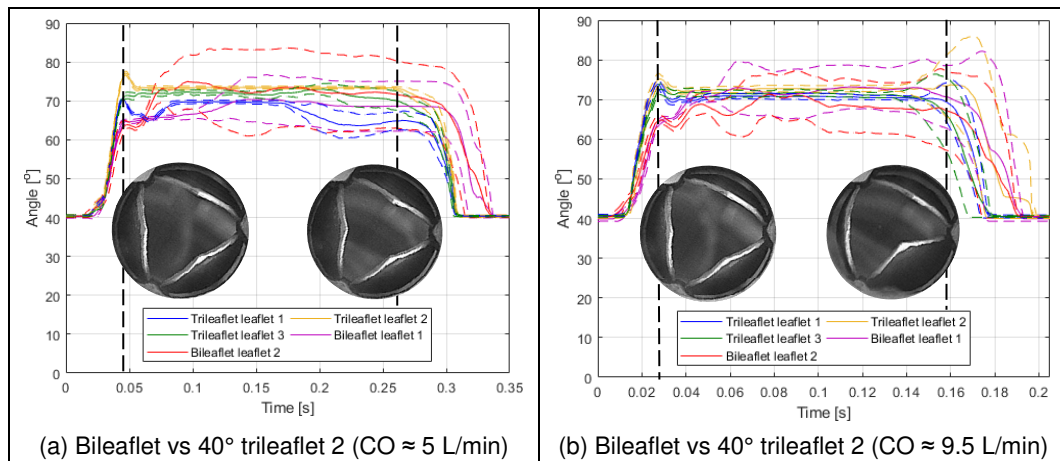
Figure 41:   Comparison between bileaflet and 40° trileaflet 2 valve motion

(a) Bileaflet vs 50° trileaflet 1 (CO ≈ 5 L/min)   (b) Bileaflet vs 50° trileaflet 1 (CO ≈ 9.5 L/min)
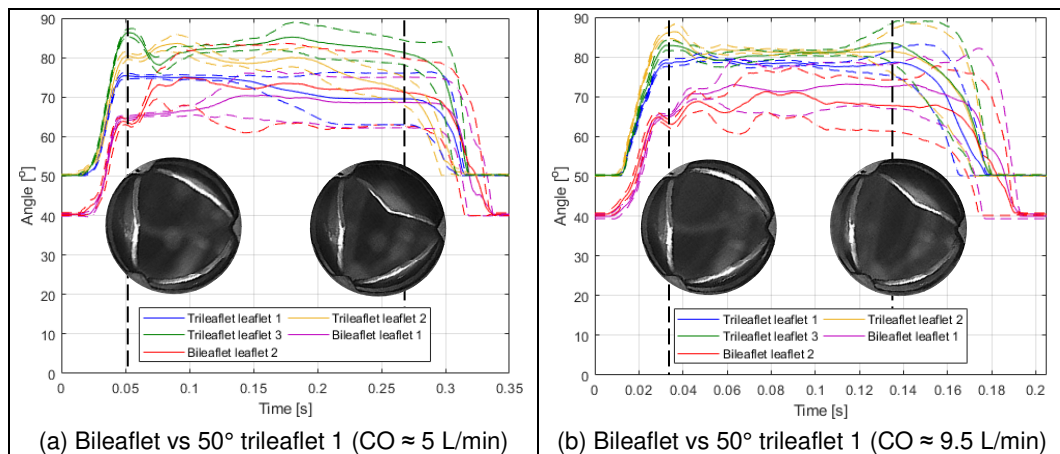
Figure 42:   Comparison between bileaflet and 50° trileaflet 1 valve motion

(a) Bileaflet vs 50° trileaflet 2 (CO ≈ 5 L/min)　(b) Bileaflet vs 50° trileaflet 2 (CO ≈ 9.5 L/min)
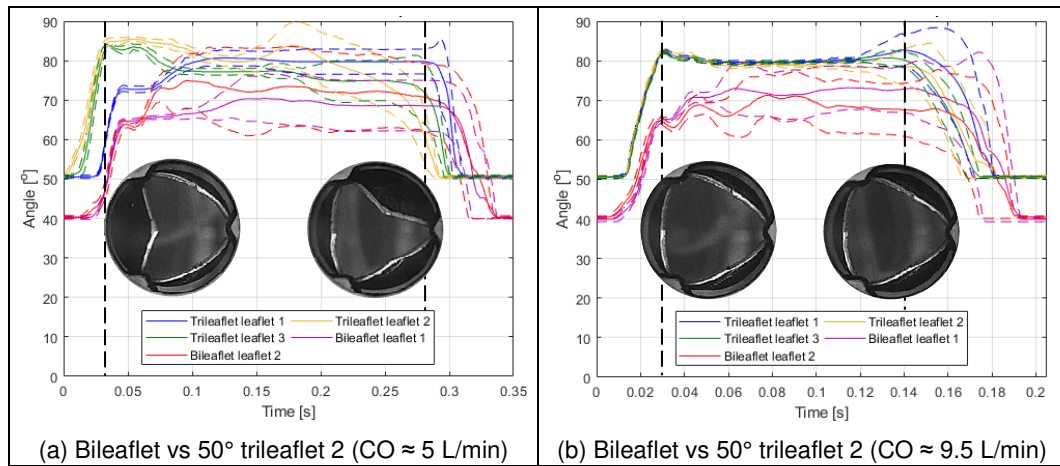
Figure 43:　Comparison between bileaflet and 50° trileaflet 2 valve motion

(a) Commercial bileaflet (CO ≈ 5 L/min)　(b) Commercial bileaflet (CO ≈ 9.5 L/min)
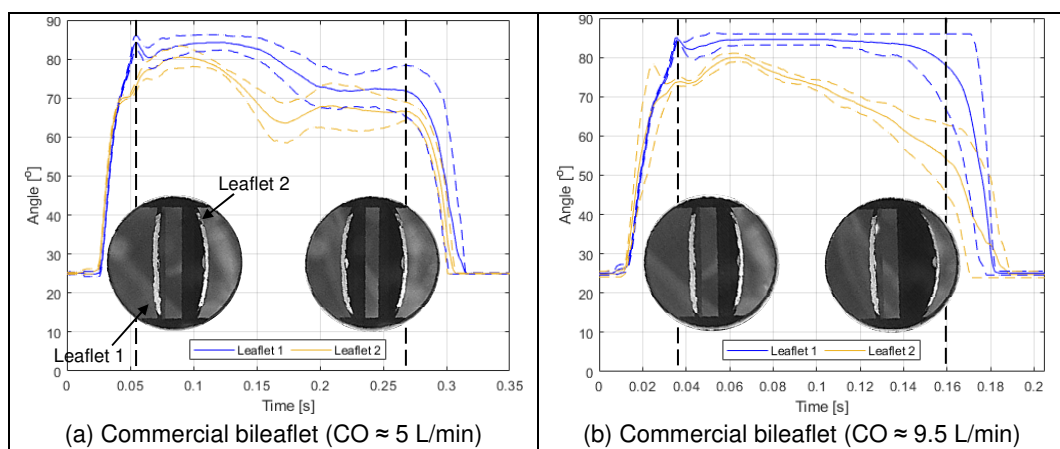
Figure 44:　Commercial bileaflet valve motion analysis

The total and maximum opening and closing leaflet tip linear velocities were calculated. Figure 95 and Figure 96 in Appendix C.2 distinguish between the different velocities that were calculated. Results are shown in Figure 45 to Figure 48. Differences in opening and closing speeds between leaflets of the same valve were observed, confirming that the assumption of symmetry is incorrect.
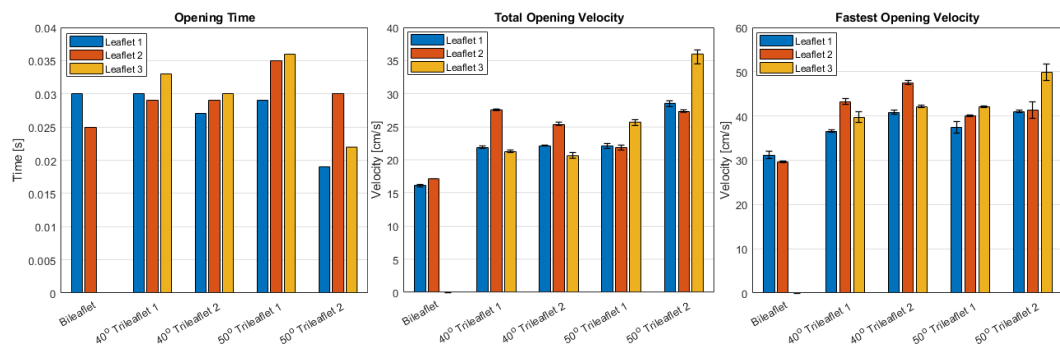
Figure 45:　Opening characteristics at 70 bpm and CO ≈ 5 L/min
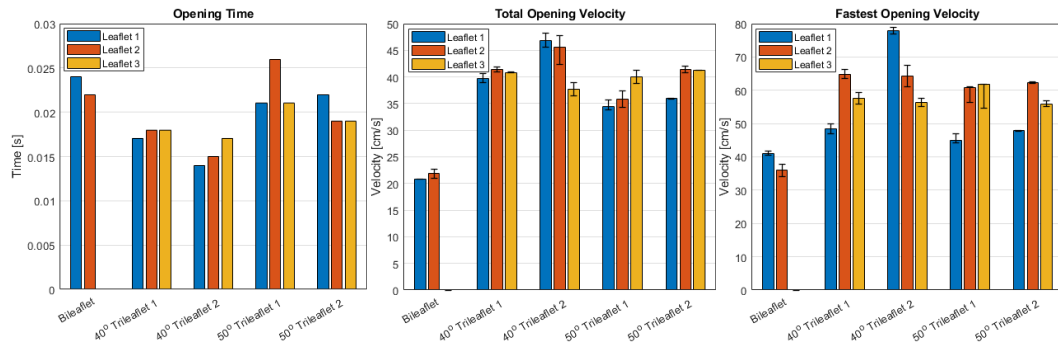
Figure 46: Opening characteristics at 120 bpm and CO ≈ 9.5 L/min
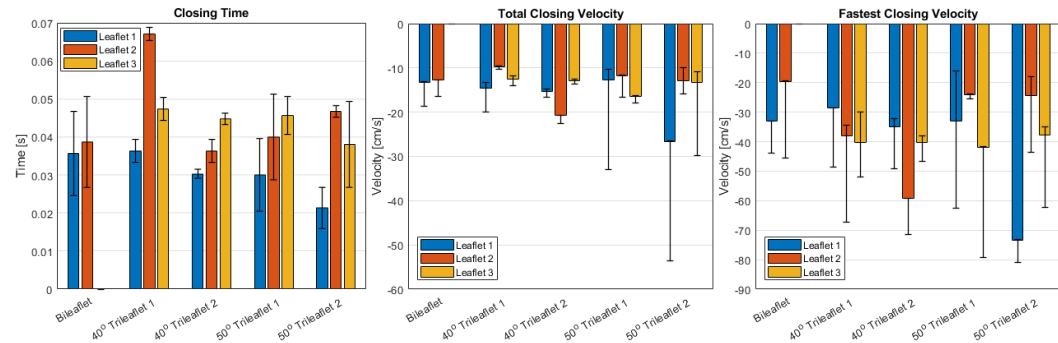
Figure 47: Closing characteristics at 70 bpm and CO ≈ 5 L/min
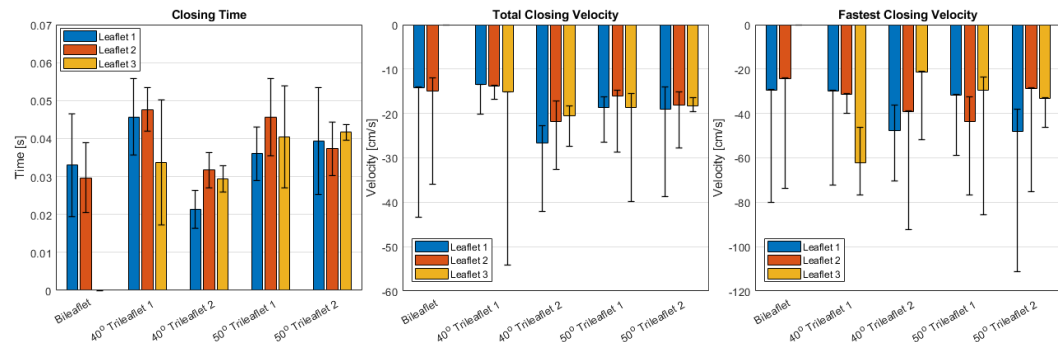
Figure 48: Closing characteristics at 120 bpm and CO ≈ 9.5 L/min

4.2.4　Discussion

Motion analysis was conducted on six valves, including four unique trileaflet designs, over the full cardiac cycle for 10 cycles at two cardiac conditions.

The leaflets tended to open simultaneously and opened with an increasing velocity that decreased later. There was very little cycle-to-cycle variation during opening. The leaflets did not open to the fully open position but opened to a greater degree as the flow rate increased. Once open, the leaflets moved asynchronously and continuous leaflet motion was observed, more so for the bileaflet valves than the trileaflet valves. There was significantly more variation during closing and the standard deviation was large. The leaflets did not close simultaneously and closed with an increasing velocity. The results show that the trileaflet valves generally started closing before the bileaflet valve during the decelerating forward flow phase. This suggests that the vortices contributed to the valve closure.

The opening times of the C1 and bileaflet valves are comparable, more so at the lower flow rate. The C2 type valves did not show improvement over the bileaflet valve. Due to the trileaflet valves' profile height, the leaflet tip linear velocities were greater than that of the bileaflet valve. The lower profile valves compare more favourably to the bileaflet valve. The leaflet that moved the fastest at one cardiac condition, did not necessarily behave the same way at the other cardiac condition. Previous studies show that the opening velocity has a minor effect on coagulation and haemolysis compared to the closing velocity [7].

Cyclic fluctuations during closing have previously been observed [30, 43, 93, 147]. Due to the continuous motion of the leaflets during systole, it was challenging to determine the starting point of closure accurately. The C1 type valves took longer to close than the bileaflet valve. The 40° trileaflet 1 valve had the longest closing time. The C2 type valves did not show much improvement over the bileaflet valve. The total and maximum linear closing velocities of the lower profile valves are comparable to the bileaflet valve, with the 40° trileaflet 1 valve showing the best performance.

Although the prototype valves did not open completely, the ISO 5840 requirements were satisfied. The commercial valve also failed to open completely, which has been mentioned in literature [43, 65, 93, 99, 134, 147, 148]. If the trileaflet valve design is optimised, and precision manufacturing methods are used to develop a prototype, the valves might open to a greater extent and the CPD performance parameters will further improve. More investigation is required to confirm this. Other than a small EOA and greater flow disruption, blood clots can form if the leaflet does not sweep the entire hinge area by opening completely [99].

The commercial valve opened and closed faster than the other valves and generally also opened to a larger degree. The movement of the leaflets was asymmetrical, varied considerably for each cycle and the fully open position was not maintained by both leaflets. The leaflets also displayed continuous motion while open. The valve's leaflet position over time plots resemble that of other studies conducted on the same valve [65, 113]. The faster motion of the leaflets is probably related to the material and manufacturing specifications and strict quality control processes that commercial valves must adhere to.

For the bileaflet valve, a rebounding action during leaflet closure was detected, as shown in Figure 49 (the key refers to each cycle). The maximum rebound was 5°.
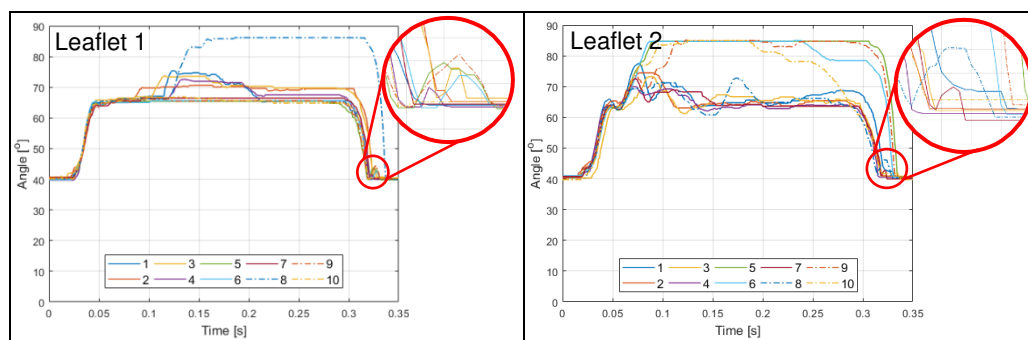
Figure 49:   Bileaflet valve motion at CO ≈ 5 L/min (showing rebounding)

The rebounding behaviour was observed for both leaflets at both cardiac conditions but was not observed for the other valves. Rebounding can cause mechanical damage to erythrocytes and platelets. The rebounding did not seem to affect the performance indicators, as it occurred over a very short time.

The trileaflet valve results were compared to two published trileaflet valve studies with HSV analysis. The first study is based on the *TRI* valve [45, 149] (patent [48]). The *TRI* valve is similar in design to the C2 type valve and manufactured from titanium, with a density of 4 507 kg/m^3 [45]. The test conditions were 5 L/min CO at 70 bpm and the motion analysis was conducted over 30 cycles at 1 000 fps. The performance of the valve was compared to a same-sized *SJM* valve. *SJM* leaflets are manufactured from graphite and coated in pyrolytic carbon. Graphite has a density of 2 250 kg/m^3 [150], comparable to pyrolytic carbon. Leaflet flutter and asynchronous closure were observed. The *TRI* valve failed to maintain its fully open position of 90°. The experimental results were used to validate a 1/3rd symmetry CFD analysis. Figure 50 displays the average computed (CFD) and measured (Exp) leaflet velocities. The red stars indicate the maximum CFD results.
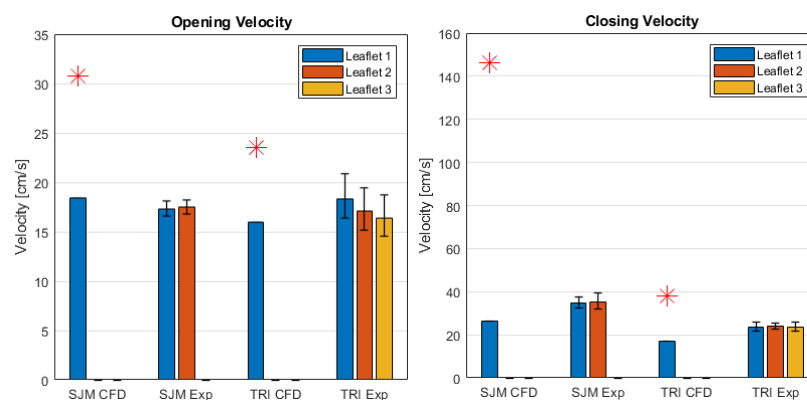
Figure 50: *TRI* **valve velocity characteristics**

The results revealed that the *SJM* and *TRI* valves took approximately the same time to open, but the *TRI* valve started closing first and took longer to close. This is attributed to the valve's mechanism of closure (by the action of the vortices). However, if material differences are considered, similar results might not be observed. The difference between the moment of inertia of the *SJM* and *TRI* valve leaflets is much smaller if mass is adjusted for. This will result in a greater angular acceleration of the leaflets of the *TRI* valve.

The second study is based on the valve shown in Figure 51 [43] (patent [47]). The design of the valve is fundamentally different from the design presented in this study. The leaflets open in the same way as bileaflet valves, which is opposite to that of native valves. The downstream flow profile will show one minor central jet and three major lateral jets. Vortices will not affect valve closure. The leaflets of the valve were manufactured from polyether ether ketone (PEEK). PEEK typically has a density of 1 300 kg/m^3 [151]. The valve was tested in a saline solution at 64 bpm and various flow rates. For the motion analysis, the focus was mainly on the opening and closing phases. The analysis was conducted over 5 cycles at 500 fps. The results were compared to two commercial bileaflet valves, the *SJM*

Regent valve and the *On-X* valve. The researchers highlighted that the continuous leaflet motion of the *On-X* valve posed a challenge in determining the start of closing. The *On-X* and *SJM* valves are manufactured from graphite. Material differences were not considered in the study.
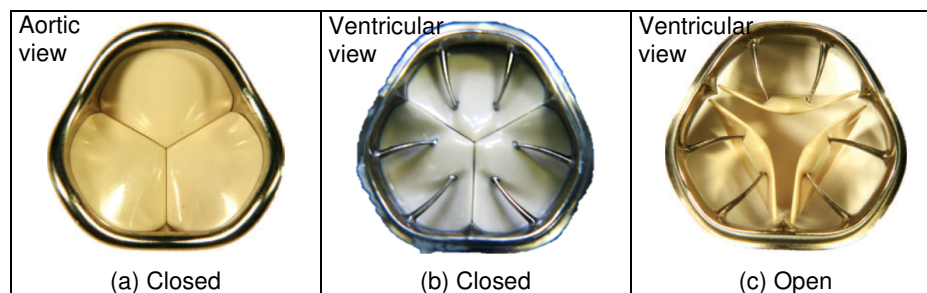
Figure 51:   **PEEK trileaflet valve [43]**

In comparison to the *On-X* valve, the PEEK trileaflet valve showed lower pressure gradients at all mean flow rates, resulting in larger EOAs. The difference between the trileaflet valve and the *SJM* valve was only evident at high flow rates. The authors observed that the *SJM* valve did not open fully, the *On-X* valve opened fully, but the leaflets moved asymmetrically and started to close much earlier. The trileaflet valve opened fully to 84°. The total closing times and the leaflet tip velocities of the three valves are compared in Figure 52. The large standard deviations are an indication of the cyclic fluctuations. The results of the trileaflet valve are comparable to both commercial valves.
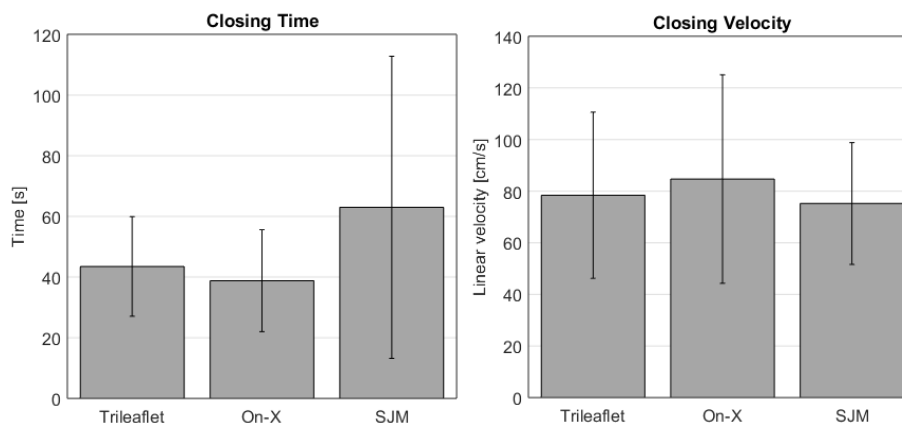
Figure 52:   **Closing characteristics of the PEEK trileaflet valve**

The good haemodynamic performance of the PEEK trileaflet valve is attributed to the leaflet geometry, particularly the curvature of the leaflets. It can probably also be attributed to an optimised, smooth hinge mechanism and the short rotational arm of the leaflets. A substantial performance improvement over the bileaflet valves is not evident. However, if material differences are considered, the trileaflet valve will most likely outperform the bileaflet valves. If all the leaflets are manufactured from the same material, the trileaflet valve leaflets will have a moment of inertia of about double that of the bileaflet valves, resulting in a smaller angular acceleration. The downstream effect of the protruding hinge mechanisms on the flow field was not discussed in the study.

Open-heart surgeries for aortic HVR involve dissection of the aortic root. Case-dependent, the surgeon can partially or completely preserve the sinuses or entirely replace the root and ascending aorta [65, 100, 147, 148, 152]. An axisymmetric conduit, shown in Figure 53 (adapted from [153]), is used to replace the aorta. Newer types of conduits include an expansion region to simulate the sinuses. The valve cannot be implanted much higher than indicated in Figure 53 as this will affect, or even obstruct, flow into the coronary arteries. If the sinuses are sacrificed and a straight conduit is used, the closing dynamics of a trileaflet valve will change and the premise on which the trileaflet valve design is based will no longer be valid.
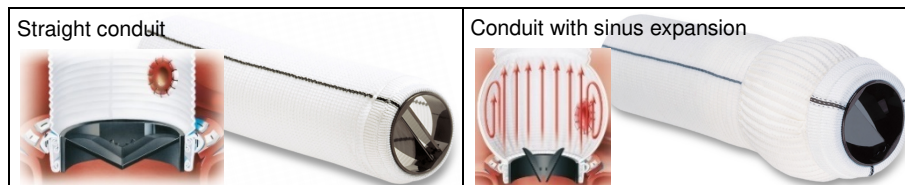
Figure 53: **Ascending aorta prostheses [153]**

4.3 Discussion

The performance requirements evaluation is shown in Table 13. Requirement viii pertains to the experimental and numerical performance of the valve. Table 13 only addresses the experimental performance characteristics.

Table 13: **Requirements analysis and evaluation (2)**

Description	Requirement							
Performance requirements (§3.1.3.2)	i	ii	iii	iv	v	vi	vii	viii
40° Trileaflet 1	✓	✓	✓	✓	✓	✓	N/A	✓
40° Trileaflet 2	✓	✓	✗	✗	✗	✗	N/A	✓
50° Trileaflet 1	✓	✓	✓	✓	✓	✗	N/A	✓
50° Trileaflet 2	✓	✓	✓	✓	✓	✗	N/A	✓

The flow tests showed that the prototype trileaflet valves' performances, except the 40° trileaflet 2 valve, matched or exceeded the performance of the reference valve. The inferior performance of the 40° trileaflet 2 is more likely due to manufacturing imprecision than design. The HSV results showed that the valves took approximately the same time to open. The C1 type valves took longer to open than the C2 type valves. However, the valve profile of the trileaflet valves resulted in large maximum linear opening velocities. The trileaflet valves generally took longer to close than the bileaflet valve. Due to the valve profile differences, the closing velocities are comparable. Considering the large standard deviation and the asymmetries, the 40° trileaflet 1 valve showed the best performance. Comparisons to literature suggest that material choice has a large influence on the results.

Requirement vii applies to the valve's fatigue strength, which was not tested due to the differences between the prototype and final product material and manufacturing specifications. However, the test results suggest that bileaflet valves have a shorter fatigue life irrespective of the material choice.

5 NUMERICAL EVALUATION

The numerical analyses were conducted using *Siemens Simcenter Star-CCM+* 13.04.011. The aims were to 1) extend the comparative study between the valves and to investigate the effect of design variables on the flow field and 2) create a validated computational model of the final prototype HVR in the testing environment to investigate the effect of leaflet kinematics on the flow field.

5.1 Steady State Simulations

The first part of the CFD analysis was assumed steady; the leaflets were fixed and the inlet conditions were constant.

5.1.1 Computational Model

A computational model, shown in Figure 54, was created to simulate the trileaflet and bileaflet heart valves in a simplified native environment. The diameter of the upstream and downstream regions was 28 mm. The sinus region was axisymmetric with a diameter of 36.4 mm. The sinuses are often simplified as an expanded surface of revolution [45, 59, 65, 104, 115]. The dimensions of the numerical setup are representative of that of the experimental setup. The sinus expansion ratio of 1.3 is based on a method described in [65], corresponding with reported dimensions [45, 99, 154].

| (a) Full 3D model | (b) Valve detail |
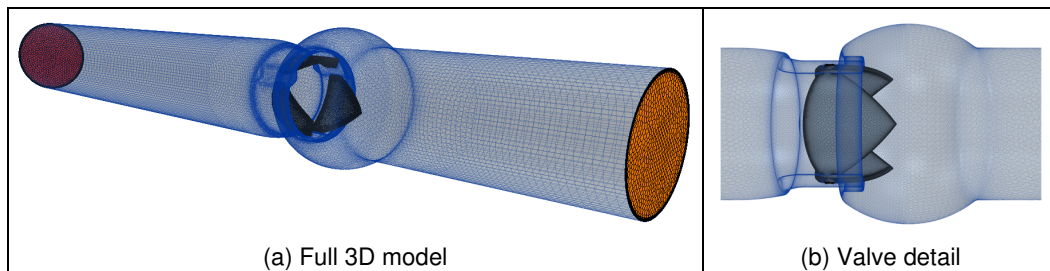
Figure 54: 3D CFD model of the open prototype valve

The length of the pipe was extended upstream and downstream of the valve to exclude inlet and outlet effects on the results. An analysis was conducted to determine the length required to obtain fully developed flow at the valve. The study was performed on a pipe with the same diameter as the valve. The same boundary conditions, physics models and mesh settings as the valve CFD models were specified. The axial velocity profile at various distances upstream from the valve inlet, measured in terms of pipe diameters (D), was computed and are displayed in Figure 55. At approximately 4D the profile started to converge to the fully developed profile. The difference in the maximum velocity between 6D and 8D is 2.3%. A total upstream length of approximately six diameters was created, which is longer than values reported in literature [45, 65, 100, 113, 115]. The outlet surface was extruded by 50 mm, resulting in a downstream length of 70 mm (excluding the sinuses). This is similar to values reported in literature [45, 65, 155]. The cell size in the extrusion regions varied based on their proximity to the region of interest.
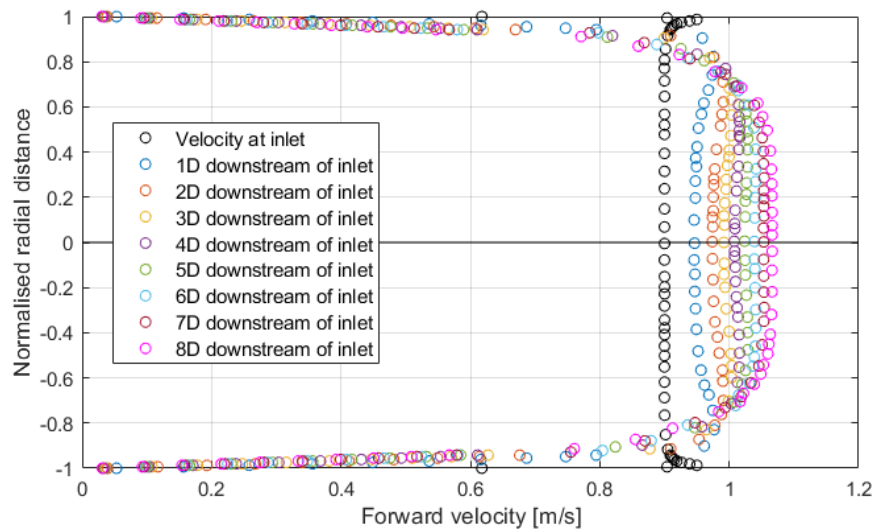
Figure 55: Velocity profile at various distances from the inlet boundary

A constant upstream velocity inlet condition was defined and a downstream outlet pressure boundary condition was specified. The dimensions of the CFD model are indicated in Figure 56. The physics models and material properties are listed in Table 14. The physics models are discussed in Appendix D.
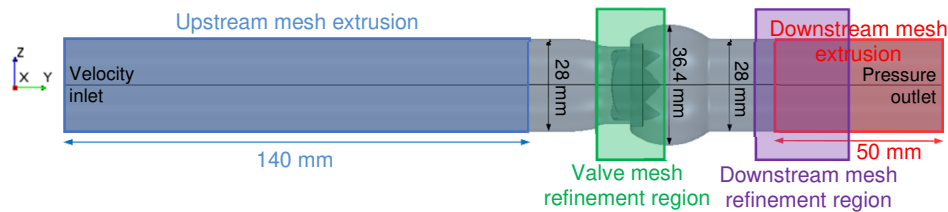
Figure 56: Geometry and dimensions of the CFD model (1)

Table 14: Physics and material properties

Space	3D
Time	Steady state
Material	Liquid (ρ = 1 100 kg/m^3; μ = 0.0035 Pa·s)
Flow	Segregated
Equation of state	Incompressible
Flow regime	Turbulent
Turbulence model	RANS – SST K-Omega (k-ω) [45, 104, 155]
Wall treatment	All y$^+$ (with a sufficiently fine mesh for low y$^+$ treatment)

5.1.2 Assumptions

The following assumptions were made in order to simplify the analyses:

- The fluid was assumed to be an incompressible Newtonian fluid with a density of 1 100 kg/m^3 and dynamic viscosity of 0.0035 Pa·s [45, 65, 93,

109, 156]. The approximation of blood as a homogeneous Newtonian fluid is widely accepted [33, 104, 113, 147].

- The segregated flow solver is valid for incompressible flow and turbulent flow regimes [157].

- Leaflets were stationary for all configurations.

- Flow rate remained constant at either peak forward flow or peak backflow conditions, depending on the type of simulation that was performed. The inlet flow rate for maximum forward flow was 25 L/min, which is representative of the flow rate at peak systole for pulsatile flow at 70 bpm 5 L/min CO [93, 100, 147]. The flow rate at maximum backflow was 3.6 L/min, measured experimentally. The peak backflow rate is a conservative assumption; peak backflow occurs while the leaflets are still in the process of closing and not when fully closed. When the leaflets are closed, the experimentally measured leakage flow rate was ~ 1 L/min.

- Surfaces of solids were ideally smooth and no-slip boundary conditions were defined.

- Gravity was not accounted for [45].

- The sewing cuff was not included in the model [104].

- Continuity, momentum, turbulence parameters, maximum velocity, transvalvular pressure drop, leaflet force and shear stress were used to assess convergence.

- In some cases, the unsteady solver was implemented to obtain a steady state solution.

5.1.3   Mesh Properties

The fluid domain was discretised with prismatic cells at the wall boundaries and an unstructured polygon mesh for the remainder of the domain. The mesh was refined in the vicinity of the valve, as shown in Figure 56. A mesh convergence study was conducted to ensure that the results are independent of the mesh size. The study is presented in Appendix E.1 and the resultant mesh properties are listed in Table 21. The base cell size was 1.2 mm and the smallest leaflet surface cell size was 0.024 mm. A similar mesh independence approach was applied in [33].

The pressure drop for fully developed internal pipe flow with simple geometries and constant hydraulic diameters can be calculated analytically [31], which was done to verify the CFD. In this case, the analytical equations only apply to a very small section of the upstream region. In smooth tubes and if gravity is neglected, the pressure loss is purely due to viscous effects. In [31], fully developed turbulent flow is accepted for $Re > 10^4$ and laminar flow is accepted for $Re < 2\,300$. However, in many applications, flow can become fully turbulent earlier. Following a conservative approach, flow with $Re > 4\,000$ can be treated as turbulent. For the simulated conditions, $Re \approx 6\,000$; therefore, some variation between the CFD and the analytical calculations can be expected. The explicit first Petukhov equation was used to calculate the friction factor for turbulent flow (valid for $3\,000 < Re < 5 \times 10^6$) [31]. The analytically calculated pressure drop over a short section in the upstream region was 6.62 Pa, compared to the numerically

computed pressure drop of 6.19 Pa over the same length. This was assumed acceptable.

5.1.4 Summary of Analyses

A series of simulations were conducted by varying design parameters. A brief overview of each analysis is provided.

5.1.4.1 Open Leaflets

The motion analysis revealed variation in leaflet motion and maximum open angle. Steady state models of the 40° and 50° trileaflet valves and the bileaflet valve were created at five different maximum open angles, ranging from 70° to 90°. The aim was to determine the effect of the leaflet open angle on the flow field. Simulations of stationary leaflets at various maximum open angles were conducted (Figure 57a). The hinge geometry was not included in the model. The longitudinal planes of the valves are defined in Figure 57b – c.

| (a) Open angles | (b) Trileaflet valve | (c) Bileaflet valve |
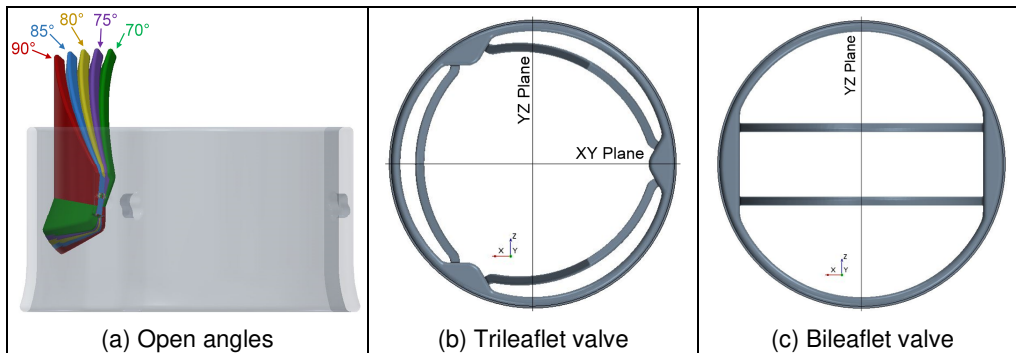
Figure 57:   Open valve geometry

5.1.4.2 Housing Length

Two different housing lengths were modelled to analyse the effect on the bulk flow parameters. The normal housing length (Figure 58a) is based on the *On-X* valve design. The shorter housing length (Figure 58b) has a reduced length downstream of the hinges. Hinge geometry was neglected. The aim was to investigate the claim that the optimised housing length promotes laminar flow.

| (a) Normal downstream housing length (6 mm) | (b) Shorter downstream housing length (2 mm) |
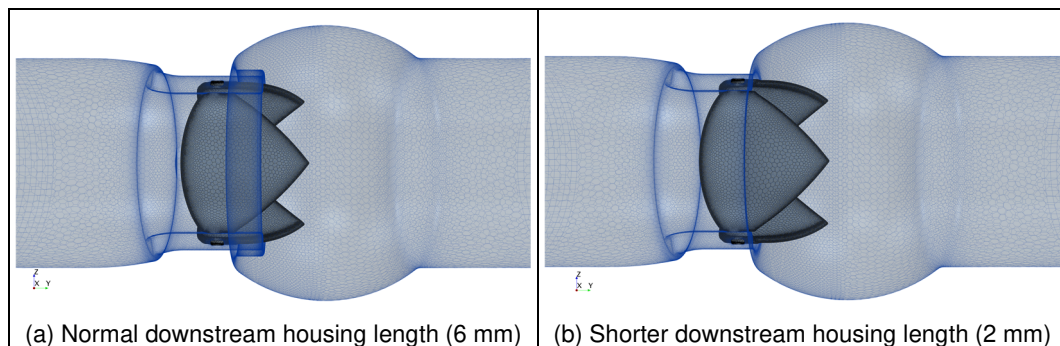
Figure 58:   CFD models indicating housing geometry comparisons

5.1.4.3 Leaflets Edges

The rounded edges of the leaflets were slightly modified to reduce flow separation at peak systole (refer to Figure 59a and Figure 59b). Two leaflet designs were evaluated. The leaflets were modelled in the fully open position. Hinge geometry was neglected.

| (a) Original leaflet edge geometry | (b) Modified leaflet edge geometry |
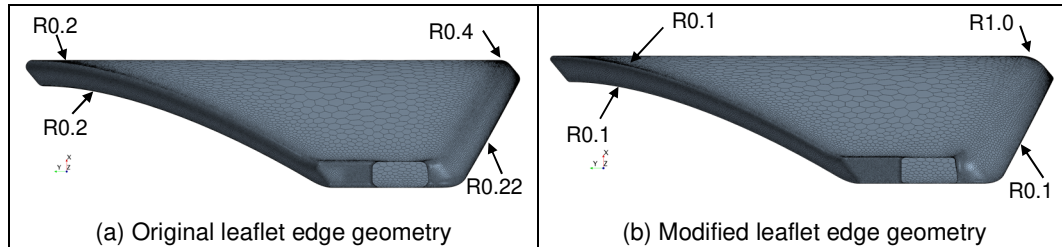
Figure 59: **CFD models indicating leaflet geometry comparisons**

5.1.4.4 Closed Leaflets

The valves were modelled in the closed position to determine maximum velocity at peak backflow conditions. One of the closed models is shown in Figure 60. Analyses were conducted for all five valves (i.e. the 40° and 50° trileaflet valves with both hinge configurations as well as the bileaflet valve). Leaflet and housing geometries were not modified or scaled; gaps ranged between 50 – 100 µm. The hinge geometries were included. The dimensions of the total prism layer and the near-wall prism layer were modified.

| (a) Full 3D closed model | (b) Valve detail |
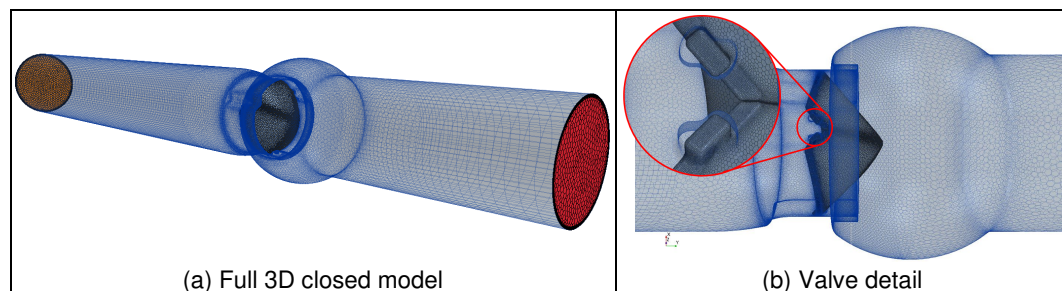
Figure 60: **3D CFD model of the closed valve**

5.1.5 Results and Observations

For each simulation, the effect on the bulk flow was analysed. Planar results are mainly presented (refer to Figure 57). For the sake of brevity, the results are also compared to literature and observations are highlighted in this section. Results are summarised in §5.1.6.

5.1.5.1 Open Leaflets

The maximum wall y^+ values varied between 0.6 and 0.9. Velocity magnitude streamlines as well as contours on two axial planes downstream of the valve are shown in Figure 61. The first plane is located within the sinus region, 8 mm downstream of the top of the valve housing. The second plane is 30 mm

downstream of the housing. The 75° and 85° results are shown in Appendix E.2 (Figure 103). As the orifice decreased in size, the maximum downstream velocity increased and the flow was more chaotic. The streamlines show the effect of the increased obstruction to the flow; the flow is disorderly, swirling flow structures are present and large velocity gradients are observed. This contributes to an increase in turbulence and higher shear stress in the fluid. This increases the likelihood of coagulation and haemolysis. Thrombus formation is promoted in the recirculating regions. The results show that the fastest flowing fluid develops around the 50° trileaflet valve. The streamlines and velocity magnitude, as the maximum open angle decreased, correspond with the results of a computational study of a dysfunctional bileaflet valve that fails to open completely [109].
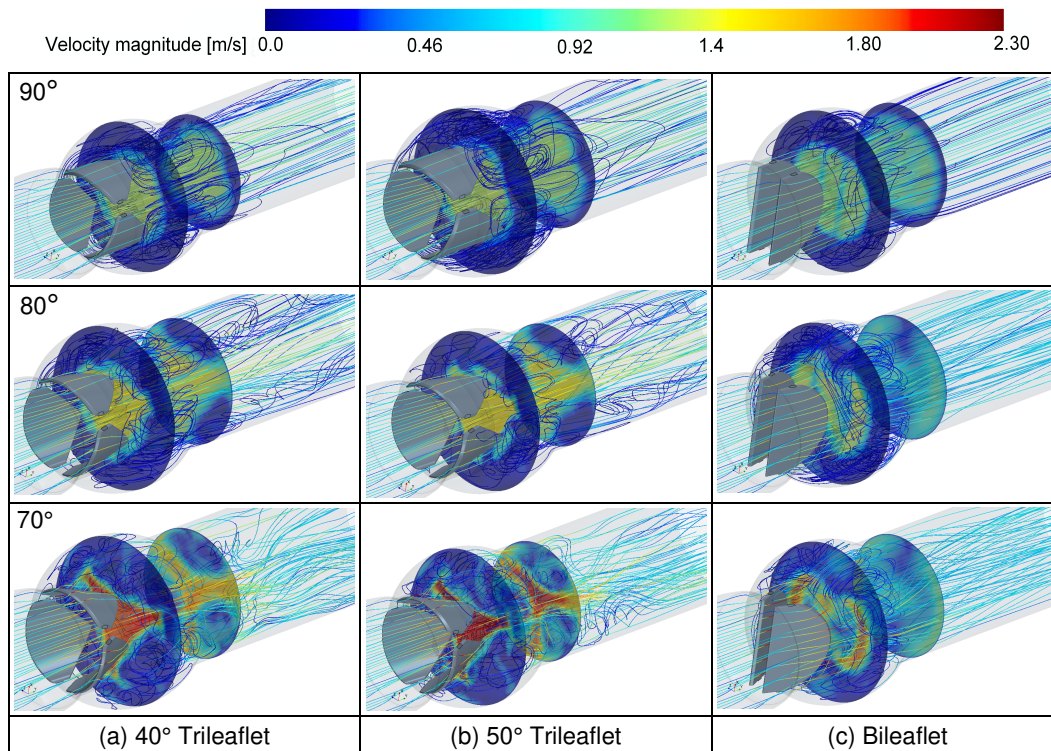
Figure 61: **Velocity results at various open angles (1)**

Figure 62 shows the WSS results (the 75° and 85° results are shown in Appendix E.2 (Figure 104)). WSS increased as the open angle decreased. The maximum WSS was observed on the leading edges of the leaflets. A larger region of high stress was observed on the leaflets' leading edges as the size of the orifice decreased. WSS on the trailing edges of the leaflets and on the edges around the hinges increased as the open angle decreased. WSS on the housing surface also increased as the open angle decreased. At 70°, the housing WSS was the greatest, particularly at the hinge regions and where the leaflet edges are near the housing. High shear stresses on the inlet side of hinge build-outs were observed. The results agree with the results reported in [109]. To reduce the WSS in these regions, the build-outs should be tapered towards the valve inlet and outlet, with the maximum width at the hinge recesses. The change in geometry should be smoother. A similar approach should be followed for the C2 type valves, with gradually expanding protruding geometries.
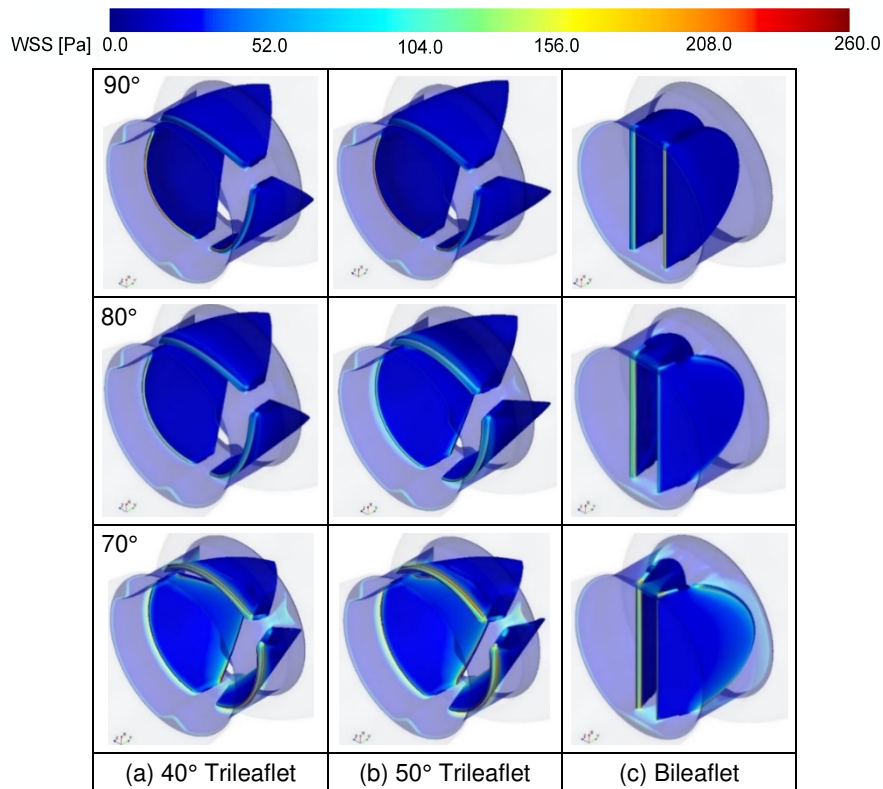
Figure 62:   WSS results at various open angles (2)

Velocity profiles at the intersection of the YZ plane and the axial planes are shown in Figure 63 to Figure 65 (also refer to Appendix E.2). At 90°, the maximum downstream velocities were comparable for all the valves. As the maximum open angle decreased, there were some differences in the maximum velocity. At 70°, the bileaflet valve had the lowest downstream velocity; the 50° trileaflet valve had the highest downstream velocity. The maximum velocity results differ by less than 0.5 m/s at 8 mm downstream. Just as the velocity streamlines in Figure 61 show, flow uniformity deteriorated further downstream and as the open angle decreased. The characteristic triple jet pattern of the bileaflet valve is observed. This type of profile results in larger velocity gradients, leading to the development of higher shear stresses. The trileaflet valves generated a single central jet, which is physiologically representative.
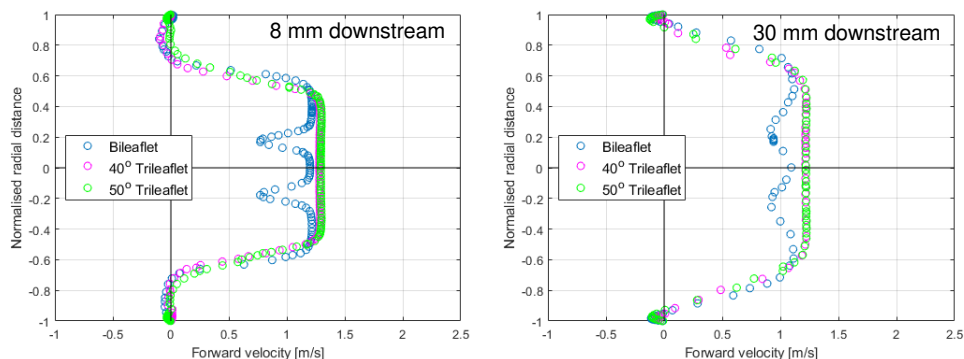
Figure 63:   Downstream velocity profile at 90° open
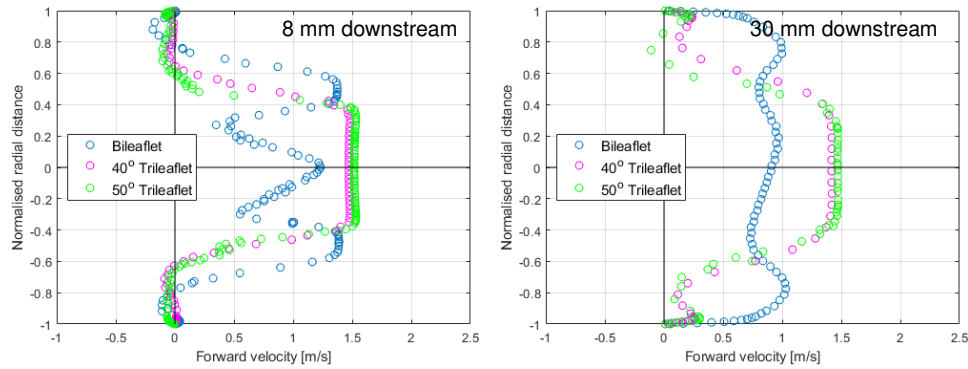
Figure 64:   **Downstream velocity profile at 80° open**
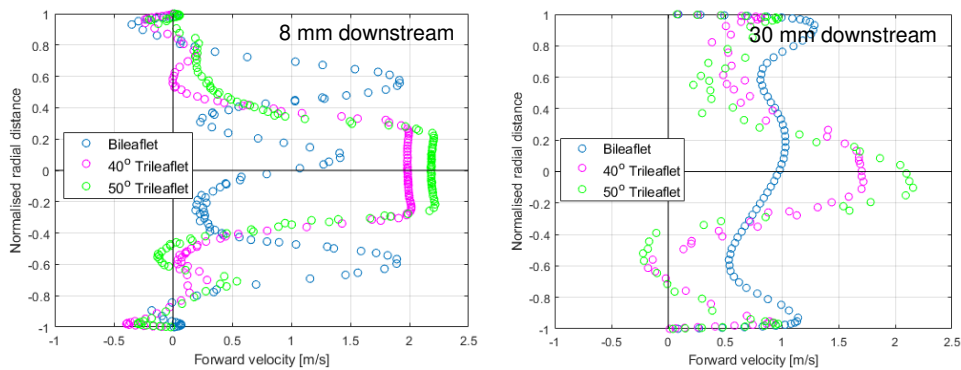
Figure 65:   **Downstream velocity profile at 70° open**

The results were compared to published results in terms of patterns and, where possible, magnitudes. The triple jet pattern of the bileaflet valve is widely documented [109, 115, 147, 148 and 155]. The 85° bileaflet valve results (Figure 105 in Appendix E.2) compare well, in terms of profile and magnitude, to a study of a bileaflet valve conducted at peak systole in the fully open position of 86° [108]. Maximum velocities of 1.22 – 1.4 m/s are reported. The bileaflet results also correspond with other CFD results; maximum velocities of 1.8 m/s at peak flow for a 27 mm valve are reported and the same triple jet pattern is observed [100]. The triple jet pattern is seen in other computational studies with velocity magnitudes at peak systole of 1.72 m/s and 1.38 m/s reported in [45] and [93] respectively. The trileaflet results could only be compared to the *TRI* valve, which reports a maximum velocity of 1.55 m/s at peak systole [45]. The velocity profile at different stages of the cardiac cycle in [45] are similar to the results presented in this report, taking cognisance of the differences between the two studies.

Vorticity and pressure results are presented in Figure 66 and Figure 67 (also refer to Appendix E.2). Vorticity increased as the open angle decreased. Regions of high vorticity were larger and extended further downstream at 70°. If the valve fails to open completely, there is more flow obstruction and the leaflet wake is large. For the bileaflet valve, vortices developed in the centre of the aorta; for the trileaflet valves, vortices developed near the aortic walls. Higher levels of vorticity were noticed for the 50° trileaflet valve. The vorticity contours and magnitudes of the trileaflet and bileaflet valves correspond with the results of the *TRI* valve [45].
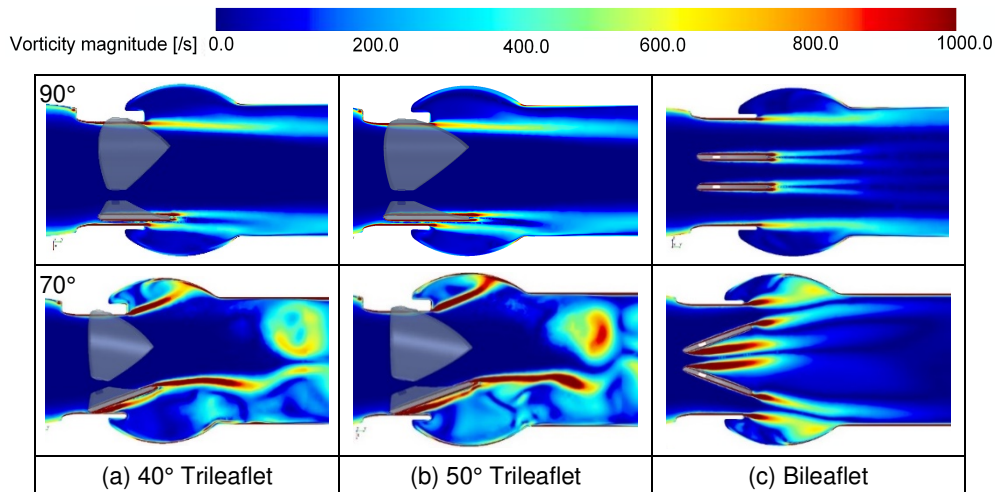
Figure 66: **Vorticity results at various open angles (1)**

The pressure results can offer an explanation for the incomplete valve opening that was observed experimentally, for both the bileaflet and trileaflet valves. At smaller open angles, the pressure on the upstream side of the leaflet surfaces was greater than the pressure on the downstream side of the leaflet surfaces. The net pressure force created a moment about the leaflet's rotational axis that resulted in opening. However, as the open angle increased, the pressure difference between the upstream and downstream leaflet surfaces decreased. This results in either a smaller moment about the leaflet's rotational axis or even a moment that causes partial closure of the leaflets.
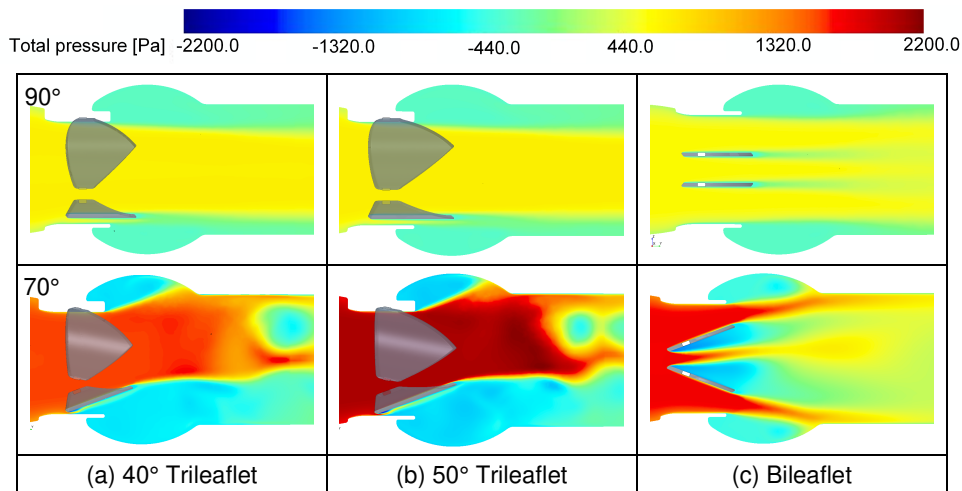
Figure 67: **Pressure results at various open angles (1)**

The pressure drop at peak systole is shown in Figure 68a. The 40° trileaflet valves had the smallest pressure drop, but the difference between the valves decreased as the total open angle increased. The results vary from the experimental results (Figure 36a). The CPD tests were conducted over a full cardiac cycle and the results refer to the average pressure drop during forward flow. Comparisons to the CPD test results are meaningless for the steady state simulations. The bileaflet pressure drop compares well with the steady state *in vitro* results presented in [99].

The tests were conducted at 25 L/min on bileaflet valves with an internal diameter of 24.2 mm and maximum open angle of 85°. The measured pressure drop to 97 mm downstream was 1.4 mmHg. The computed pressure drop at peak systole for 21 mm bileaflet valves varied between 2.49 – 3.95 mmHg in [155]. A larger pressure drop is expected for a smaller valve.

The maximum velocity magnitude in the fluid domain is plotted in Figure 68b. At 70°, the difference between the velocity magnitudes was the greatest. The fluid around the 50° trileaflet valves had the highest velocity. The fluid velocities of the bileaflet and 40° trileaflet valves were similar. The velocity results from literature (previously discussed with reference to Figure 63 to Figure 65) are consistent with the results presented in Figure 68b.

(a) Pressure drop (to 50 mm downstream)   (b) Maximum velocity magnitude in fluid
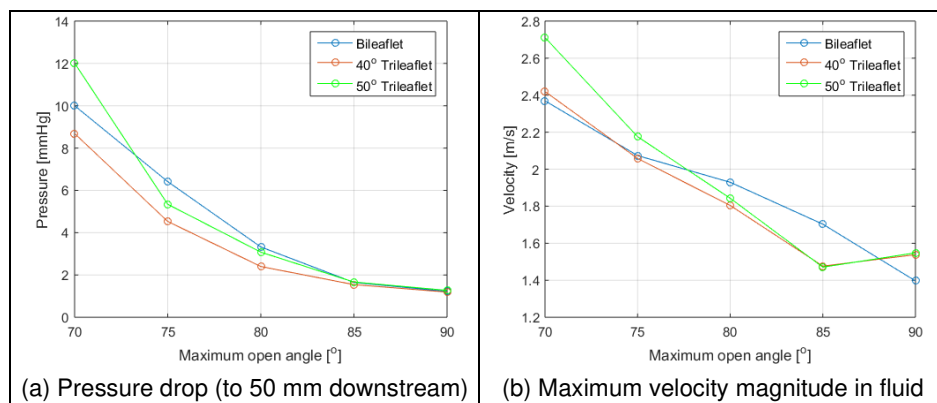
Figure 68:   Pressure drop and maximum velocity magnitude results

The average WSS is plotted in Figure 69a. The results between the different valves are comparable, with a smaller difference as the open angle increased. The highest WSS was observed at the leading edge of the leaflets. The average WSS results are dominated by the low WSS (< 10 Pa) over the majority of the leaflet surface. Presenting the results in this form can be misleading. However, peak WSS results can also be misleading. As an artefact of the numerical model, some isolated cells can have very high WSS values. To overcome this problem and not to misrepresent the results, the average WSS over the leading edge was computed and is shown in Figure 69b.

(a) Average WSS over leaflet surface   (b) Average WSS over leading edge
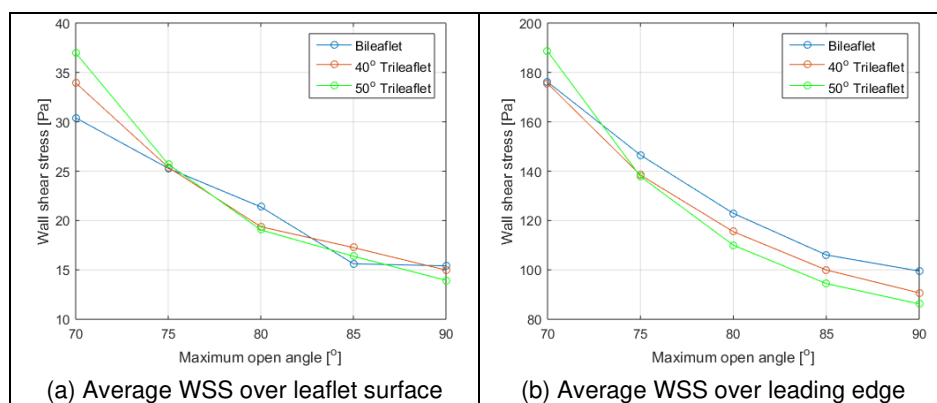
Figure 69:   Average WSS CFD results

In [65], the average WSS over the leaflet surface of different bileaflet valves for a simulated cardiac condition of 4 L/min, range between 19 – 24 Pa. The fully open position of the bileaflet valves is 85°, but it is reported that the valves did not open completely. The maximum stress locations correlate with those reported in [109].

5.1.5.2 Housing Length

The pressure and velocity results at peak systole were not affected by the housing geometry. The velocity profiles on the downstream axial planes were analysed in the same manner as before and a difference was not observed, neither in terms of magnitude nor profile shape. The maximum turbulent energy (Figure 70a) gives an indication of the turbulence intensity [147] and the energy dissipation rate (Figure 70b) can be used to quantify damage to erythrocytes and platelets [32, 158]. Figure 70 shows that the longer length housing seemed to promote downstream laminar flow.

(a) Maximum downstream turbulent energy

(b) Maximum downstream energy dissipation rate
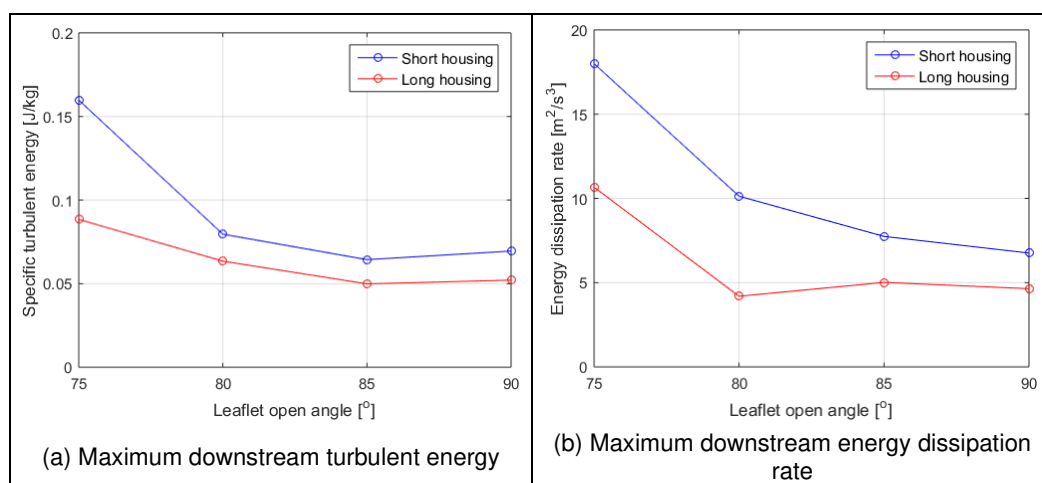
Figure 70:   CFD results of different housing geometries

The effect of the housing length is displayed more clearly on the scalar vorticity and velocity plots, shown in Figure 71. At 90°, a large difference in the results was not observed. At 75°, there was a distinct difference. Higher levels and larger regions of vorticity are seen. The longer housing maintained a more uniform central jet.
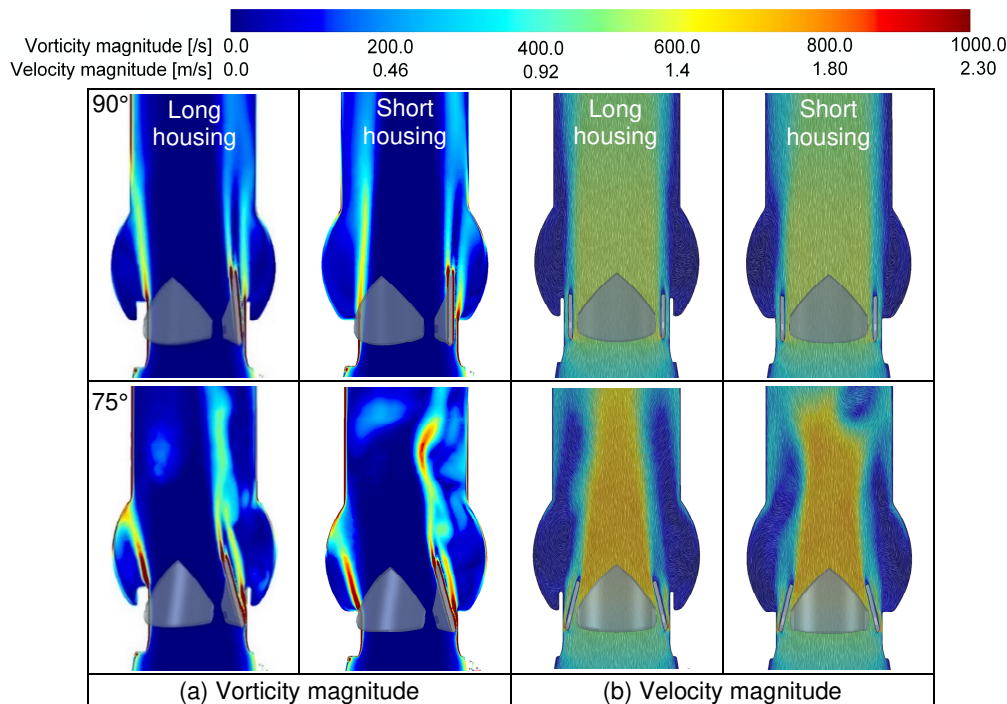
Figure 71: Effect of housing geometry on the flow field

5.1.5.3   Leaflets Edges

The maximum wall y^+ values varied between 0.62 and 0.94 for the different configurations. An effect on the maximum WSS, which is considered one of the major determining factors of valve performance, was not observed. The WSS results for both geometries were almost identical to the results shown in Figure 69. In both cases, the threshold for platelet activation was exceeded at the leading edge. The streamlined leaflet did not have any effect at peak systole but can give rise to high-speed leakage jets during diastole. The limitations of the model are noted; small geometrical changes have a localised effect [59]. Bulk flow parameters are not affected. The RANS models are not suitable for analysing the effect of subtle changes on the flow field. A multi-scale approach is recommended.

5.1.5.4   Closed Leaflets

The maximum wall y^+ values ranged between 0.77 and 1.06. The maximum velocity and WSS results at backflow conditions were much larger in comparison to forward flow conditions, which is attributed to the leakage jets. Fluid velocity magnitudes on an axial plane 1 mm from the ventricular side of the housing of $2 - 3$ m/s were computed, which is comparable to results summarised in §2.4.3. The maximum fluid velocity magnitude around the C1 type valves is comparable to that of the bileaflet valve (Figure 72).The C2 type valves showed the highest velocities (indicated in red). For all the valves, the highest velocity was observed in the gap between the leaflets. To reduce the velocity, the gap between the leaflets can be increased. However, this will increase leakage. CFD has previously been used to analyse the velocity of the leakage jets of bileaflet valves and velocities of 14 m/s were computed [14]. This is comparable to the bileaflet results.

The WSS results are also shown in Figure 72. For all the valves, the thresholds for platelet activation and haemolysis are exceeded. The highest WSS results are reported for the C2 type valves. For the bileaflet valve and the C1 type valves, the maximum WSS developed at the rounded corners where the pivot ears protrude from the leaflet and at the corresponding location on the valve housing. For the C2 type valves, the maximum WSS developed at the protruding parts of the housing and the corresponding locations on the leaflets, as well as along the trailing edges of the leaflets.

(a) Maximum velocity magnitude in the fluid domain

(b) Average maximum WSS over the leaflet edges

(c) Average maximum WSS over the housing surface
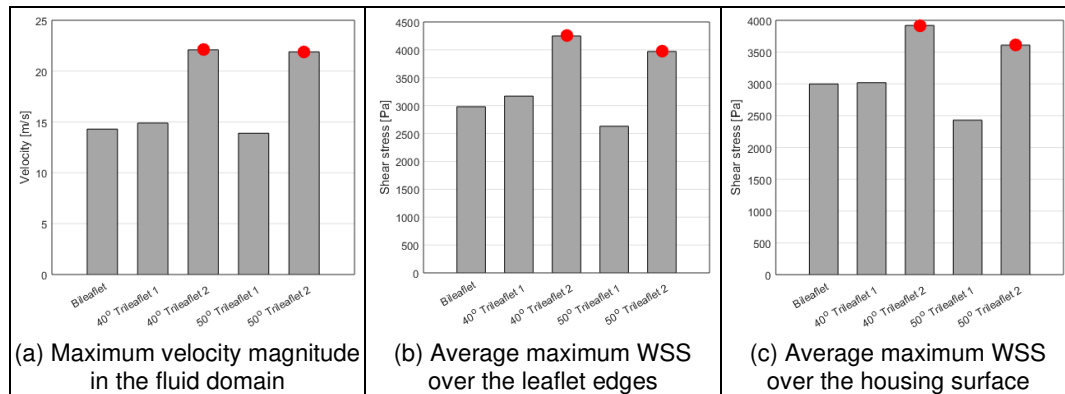
Figure 72: **Velocity and WSS results of closed valves**

5.1.6 Discussion

The results of the simulations conducted at peak forward and backward flow conditions were compared to similar CFD studies in literature, where possible, in the previous section to support the findings of this study. The outcomes indicate an increase in fluid velocity, WSS, pressure gradient and vorticity if the valve fails to open completely. In many cases, the difference between the 85° and 90° open positions is small. This suggests that, although the valve should ideally open to 90°, some flutter or a smaller open orifice at lower CO conditions should be acceptable. At the all open positions, the valves exhibited similar performance characteristics. In most cases, the trileaflet valves performed at least as well as the bileaflet valve. The trileaflet valves produced a more favourable downstream flow pattern in the form of a single, central jet with more uniform flow. The 50° trileaflet valves showed larger pressure gradients and higher maximum velocity and vorticity magnitudes at peak systole in comparison to the 40° trileaflet valves.

The longer length housing outperformed the shorter housing by promoting more structured flow downstream of the valve, even if the valve does not open completely. The streamlined leaflet geometry at peak systolic conditions had a negligible effect on the overall flow field. Based on these results, the housing and leaflet geometries were not modified. The effect of small geometrical changes should be analysed with a more detailed model, capable of capturing micro effects.

In the closed position, higher velocities were computed for the C2 type valves. The velocities of the C1 and bileaflet valves were comparable. A more detailed numerical model is required to analyse the hinge geometry accurately. A study that focusses only on the hinge region is recommended to improve the current design.

The CFD results were integrated into the performance requirements evaluation, as shown in Table 15. The requirements analysis revealed that the 40° trileaflet 1 valve presents the most viable solution. The valve was further evaluated computationally by including leaflet kinematics.

Table 15:   Requirements analysis and evaluation (3)

Description	Requirement							
Performance requirements (§3.1.3.2)	i	ii	iii	iv	v	vi	vii	viii
40° Trileaflet 1	✓	✓	✓	✓	✓	✓	N/A	✓
40° Trileaflet 2	✓	✓	✗	✗	✗	✗	N/A	✗
50° Trileaflet 1	✓	✓	✓	✓	✓	✗	N/A	✓
50° Trileaflet 2	✓	✓	✓	✓	✓	✗	N/A	✗

5.2   Prescribed Motion Simulations

A prescribed motion analysis of the 40° trileaflet 1 valve was conducted. The computing requirements to conduct a DNS or LES analysis of the full HVR with physiological input conditions and 5 L/min CO proved to be unachievable; explanation shown in Appendix E.3. Using RANS models for FSI heart applications has previously shown to result in inaccuracies. A prescribed motion analysis can overcome this problem. Asymmetrical motion, flutter, friction at the hinges, cyclic variation and compliance are also accounted for. Additionally, numerical instabilities linked to the small moment of inertia of the leaflets are avoided.

5.2.1   Computational Model

A computational model, similar to Figure 54, was created to simulate the trileaflet heart valve in the simplified *in vitro* test environment. Figure 73 shows the model in greater detail. The same planar definitions as Figure 57 apply.

(a) CFD model showing a top view of the valve	(b) CFD model showing the valve detail	(c) Photograph of the valve in the physical test setup
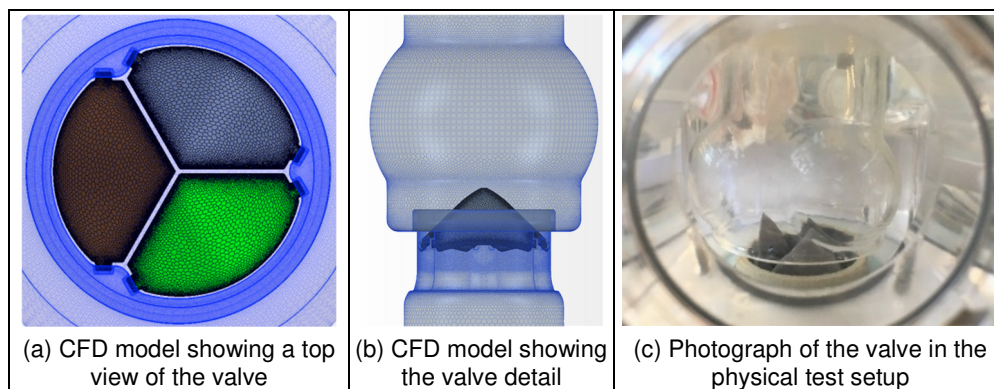
Figure 73:   3D prescribed motion CFD model of the prototype valve

The inlet velocity was calculated based on the experimentally measured flow rate (refer to Figure 34b). The upstream and downstream lengths were the same as the steady state simulations. The boundary conditions and updated geometry are indicated in Figure 74.
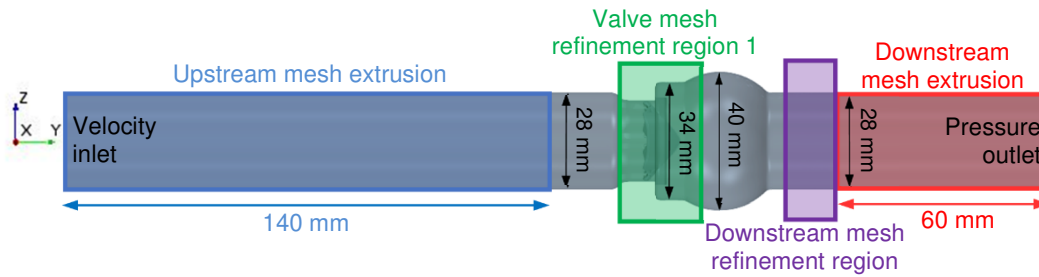
Figure 74:   Geometry and dimensions of the CFD model (2)

Using the aforementioned physics (Table 14), the simulation was solved with an implicit unsteady solver. The material properties of the fluid were adjusted according to the experimental fluid properties.

5.2.2   Assumptions

The following additional assumptions were made:

- The motion of the leaflets was based on the HSV measurements. The average motion of each leaflet, shown in Figure 40, was specified.

- The leaflet geometry was scaled by 97% and the hinge regions were widened to increase gap sizes [45, 65, 93, 114, 120, 121]. The smallest gap was 0.162 mm.

- To ensure that the results were periodically stable, the total simulation time was sufficient to allow for four cardiac cycles [33, 45, 93]. A prescribed motion simulation conducted on the 40° flat trileaflet valve design showed that the results were independent of the inlet conditions before five cycles. The cyclic results were monitored (refer to Figure 111 in Appendix E.4).

- The time step size was 0.5 ms during diastole and reduced to 0.091 ms during systole (~ 40% of the analysis). Time step sizes for prescribed motion analyses vary from 0.5 ms in [147] to 33 ms in [120]. With a time step size of 0.091 ms, rotation per time step was 0.25° (at peak leaflet velocity). The Courant number was monitored.

5.2.3   Mesh Properties

The mesh was created based on the previous simulations. Using steady state results to determine the mesh size for transient problems has been done before [33]. The mesh properties are defined in Appendix E.4 (Table 22).

Overset, or overlapping, meshes were used to discretise the fluid surrounding each leaflet. Overset meshes, explained in Appendix D.5, are useful for problems that include motion as the need for remeshing the entire domain after each time step is negated. The volume mesh is shown in Figure 75. The overset regions are shown in greater detail in Appendix D.5 (Figure 98 to Figure 101). The volume mesh consisted of 10 549 708 cells, which is larger than the CFD models reported in literature [33, 45, 93, 108, 113, 120]. A large, refined mesh was required to ensure coupling between the background and overset regions during the whole cardiac

cycle. Due to narrow gaps and small prism cells at the boundaries, the size of the cells in the leaflet-housing interface region were severely restricted.

| (a) Background and overset regions | (b) Refinement regions |
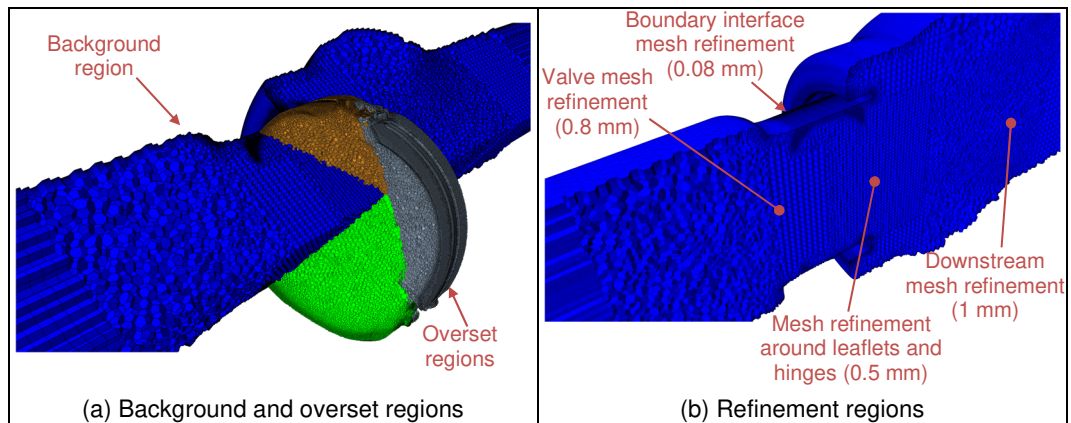
Figure 75:   3D prescribed motion CFD volume mesh

5.2.4   Results

The Centre for High Performance Computing's (CHPC) hardware [159] was used to solve the analysis. Fifteen nodes, each consisting of 24 cores with 128 GB random-access memory (RAM), were used. The central processing units (CPUs) at the CHPC are Intel Xeon processors based on the Haswell microarchitecture, with an InfiniBand (IB) interconnect between the nodes. One cycle of the prescribed motion simulation with manual time step control took ~ 21 hours to solve on 15 of the CHPC's nodes. The wall y^+ values remained below one.

Computed flow parameters are stored at the cell centroid [157]. Results can be displayed based on the cell centroid values. By displaying the results in this way, the entire cell reflects the computed cell centroid value. This is the most accurate manner to report results. However, it can result in a staggered, discontinuous appearance. Results can be smoothed using a distance-weighted interpolation method to compute the flow parameters at the cell vertices. With smoothing, an error at the mesh interface boundary was observed (refer to Figure 76).

| (a) Non-smoothed velocity field | (b) Smoothed velocity field |
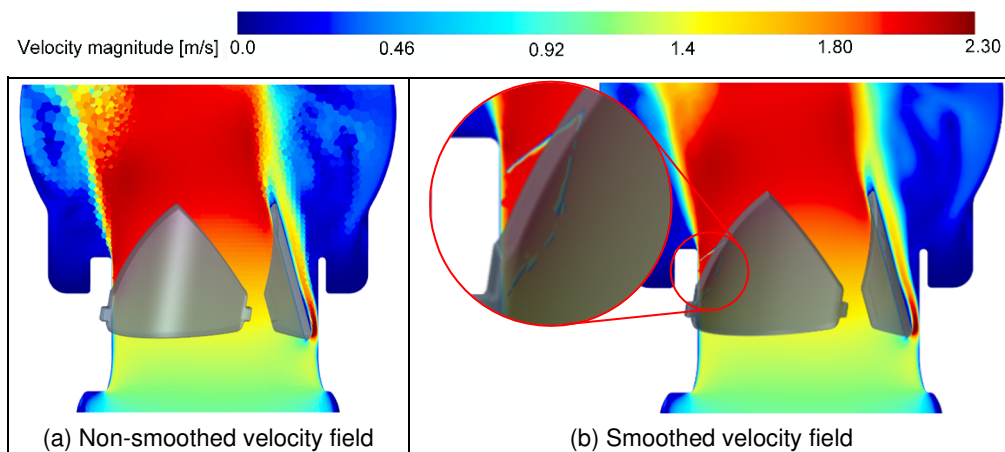
Figure 76:   Effect of smoothing on velocity results

It was interpreted as an error that arises due to the interpolation between active cells in overlapping regions on different sides on the overset boundary. The error was only observed at the intersection of the overset regions and not at the boundary between the overset and background regions. To overcome this problem, different coupling interpolation methods were investigated, the hierarchy of overlapping regions as defined when creating an overset interface was analysed and additional mass conservation treatment was applied. The problem persisted. Solving the problem by means of mesh refinement was not investigated. It was decided to display non-smoothed results for consistency and accuracy. Some of the results presented appear discontinuous. This highlights flaws and identifies regions where further mesh refinement is required.

The pressure, velocity and stress results were analysed at various time points during the cardiac cycle, as shown in Figure 77. Point 1 corresponds to the start of opening; 2 is at approximately mid-opening; 3 is when the leaflets are fully open; 4 is at peak systole; 5 is just after the leaflets start to close; 6 is at peak backflow; 7 is when the leaflets are completely closed and 8 is after valve closure. The results of the fourth cardiac cycle are presented.
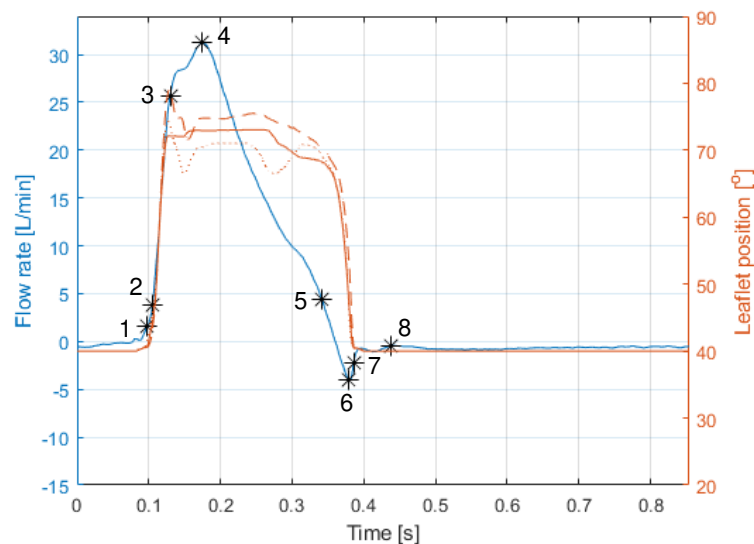
Figure 77: **Aortic flow rate and leaflet positions over one cardiac cycle**

Figure 78 compares the HSV leaflet position results to the CFD results and shows the velocity field and RSS on two axial planes (RSS_{xz}) at positions 2, 4, 6 and 7. The maximum RSS, also referred to as the major RSS, results were calculated and are shown. The RSS_{xz} results are shown on two different scales. The first scale is based on the threshold for haemolysis (600 Pa) and the second scale is based on the peak RSS value. The major RSS results on the XY (RSS_{xy}) and YZ (RSS_{yz}) planes are shown in Figure 79, with the results also displayed on different scales. For the RSS_{xy} results, the first scale is based on the lower limit of the threshold stress for platelet activation (10 Pa) and the second scale is based on the upper limit (100 Pa). RSS_{yz} scales are the same as the RSS_{xz} scales. The results for the other time points are shown in Appendix E.3 (Figure 112 and Figure 113).

Velocity magnitude [m/s]	0.0	0.46	0.92	1.4	1.80	2.30
RSS$_{xz}$ (scale 1) [Pa]	0.0	120.0	240.0	360.0	480.0	600.0
RSS$_{xz}$ (scale 2) [Pa]	0.0	1100.0	2200.0	3300.0	4400.0	5500.0

| (a) Leaflet position | (b) RSS$_{xz}$ and velocity streamlines (scale 1) | (c) RSS$_{xz}$ and velocity streamlines (scale 2) | (d) Velocity vectors |
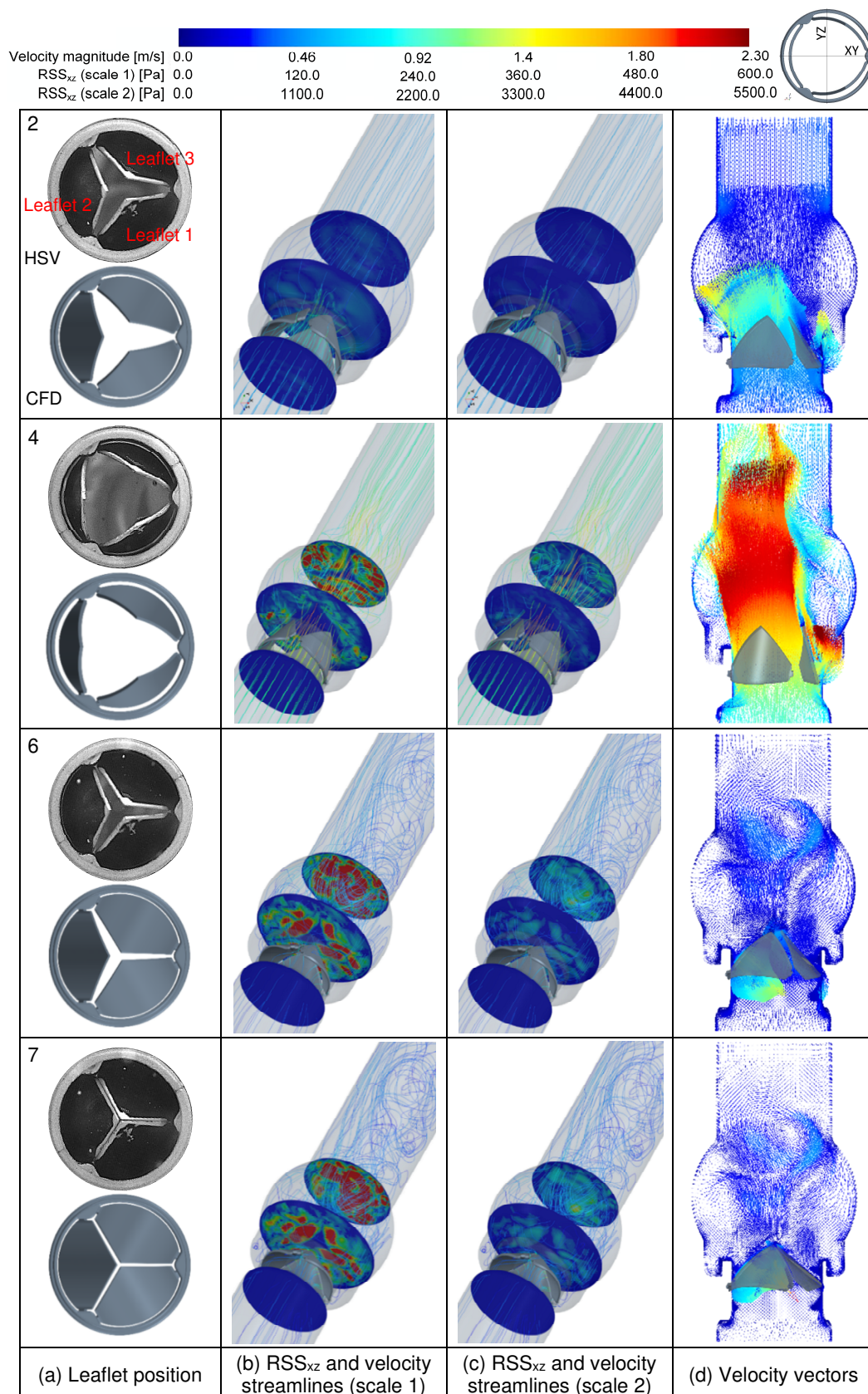
Figure 78: **Leaflet position, velocity and maximum RSS$_{xz}$ CFD results (1)**
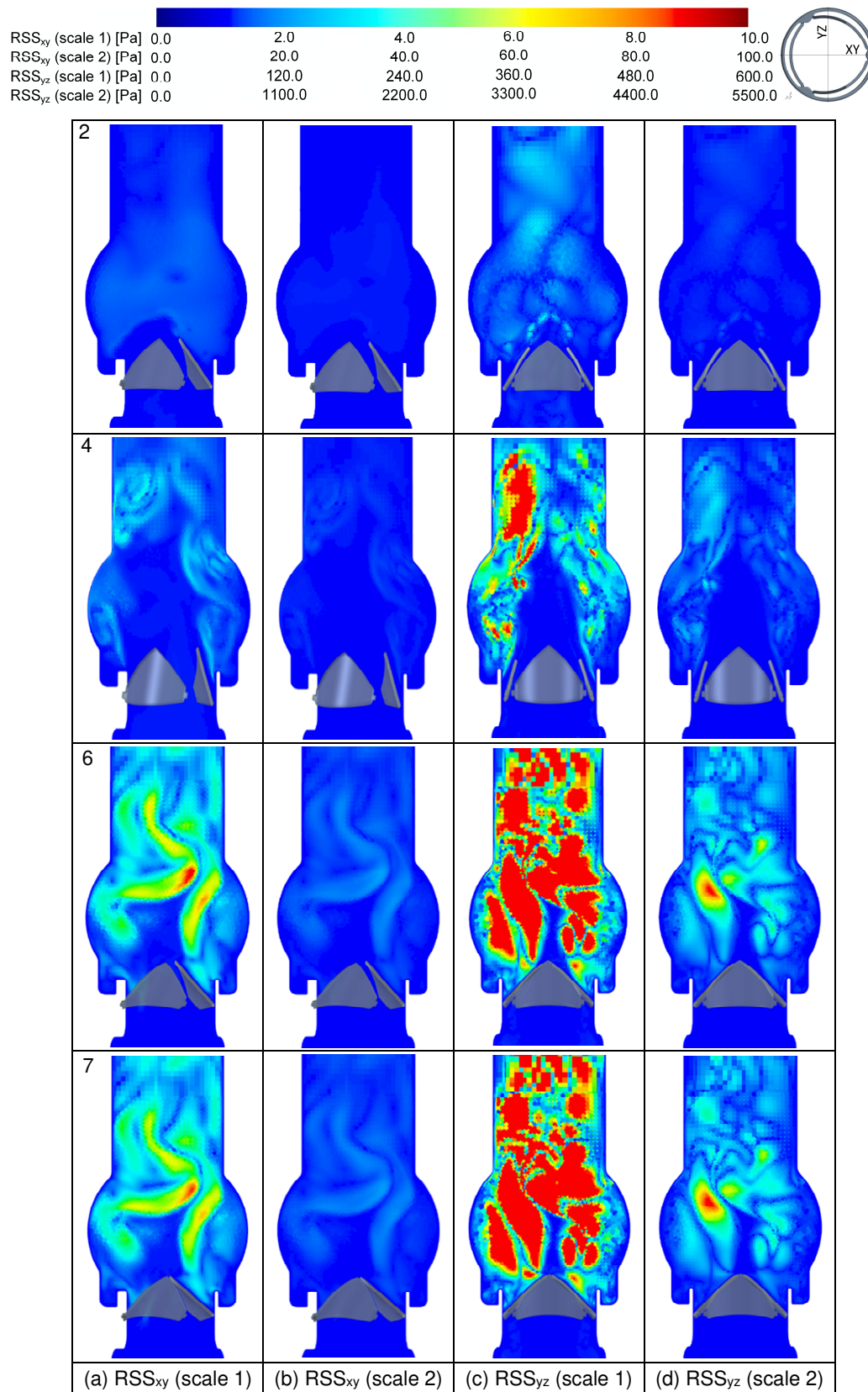
Figure 79: **Maximum RSS_{xy} and RSS_{yz} CFD results (1)**

The maximum fluid velocity over the cardiac cycle is plotted in Figure 80a. The maximum velocity during forward flow was 4.1 m/s, just prior to peak systole. The maximum velocity during backflow was 2.2 m/s, which occured at leaflet closure. Figure 80b shows the velocity profile downstream of the valve at peak systole.

(a) Maximum fluid velocity magnitude   (b) Velocity profile at peak systole
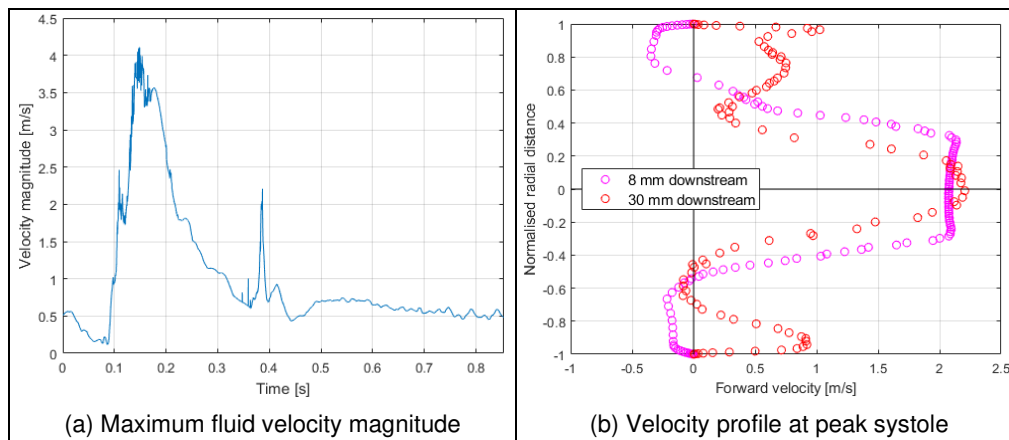
Figure 80:   Fluid velocity results

The forces exerted onto each leaflet during the cardiac cycle are shown in Figure 81. The peaks in Figure 81a correspond to the start of opening, peak systole and leaflet closure. The shear force component of the total force is plotted separately in Figure 81b. Maximum shear force occurred at peak systole and during leaflet closure. Figure 81b confirms that the pressure force is the dominant force, as assumed in Figure 24.

(a) Total force (pressure and shear)   (b) Shear force
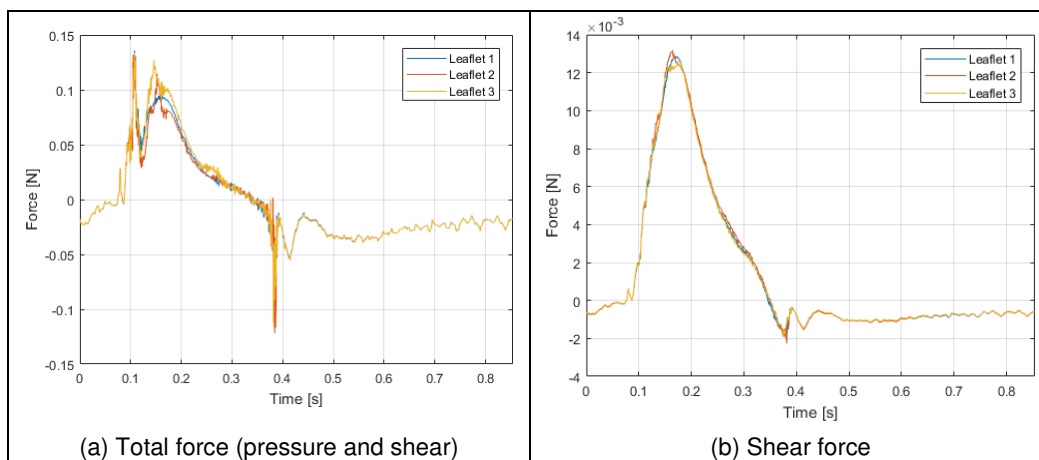
Figure 81:   Force exerted onto the leaflets over one cardiac cycle

The average WSS on the leaflets' leading edges and housing surface over the cardiac cycle is plotted in Figure 82 and the development of the WSS over the leaflet and housing surfaces is shown in Figure 83.
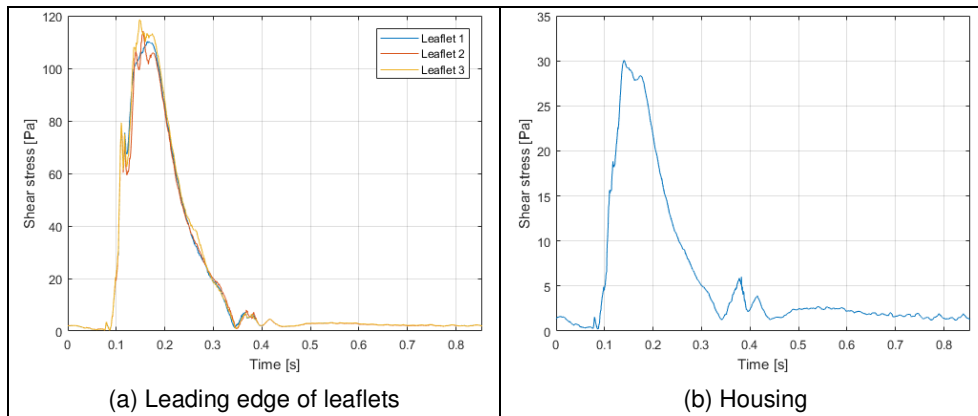
Figure 82:   Average WSS results over one cardiac cycle
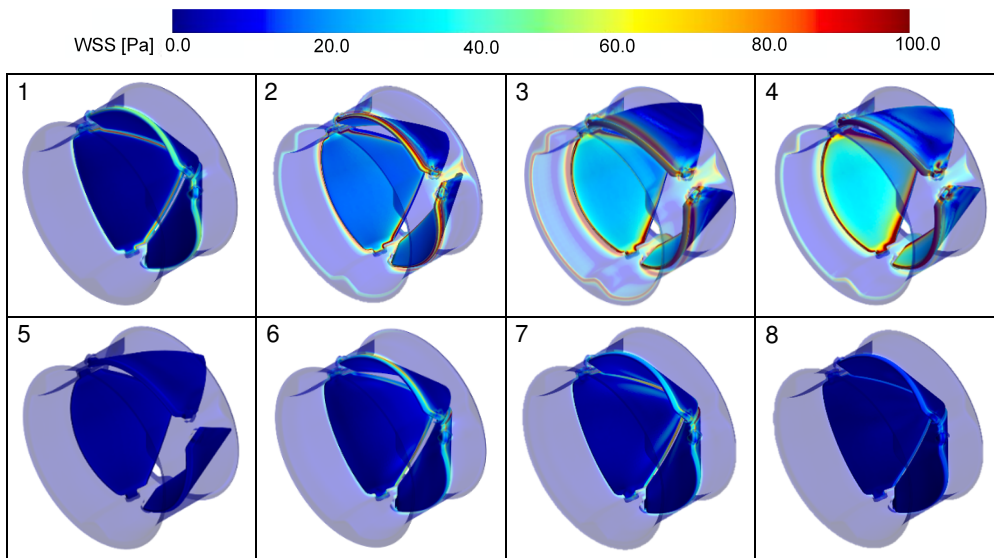
Figure 83:   WSS on the valve surfaces over one cardiac cycle

Additional results showing the development of the pressure and velocity fields over the cardiac cycle are shown in Appendix E.4 (Figure 114 and Figure 115).

5.2.5   Discussion

A 3D CFD analysis with physiologically representative inlet conditions and asymmetrical leaflet motion was conducted over four cardiac cycles on a rigid trileaflet heart valve at high spatial and temporal resolutions. The mean computed pressure gradient during systole was 7.5 mmHg and the EOA was 2.65 cm^2. This corresponds with the experimental results (8.2 mmHg and 2.50 cm^2, in Figure 35a and Figure 36a respectively).

The RSS magnitudes on all planes increased during opening and remained high while the leaflets closed (Figure 78, Figure 79, Figure 112 and Figure 113). The highest shear stresses developed around the central orifice jet, corresponding with the locations of the maximum velocity gradients. From point 1 to 3, RSS$_{xz}$ was above the platelet activation threshold but below the haemolysis threshold.

Throughout the opening phase, the flow remained orderly, but some recirculation was observed in the sinus region. The velocity vectors show that the leaflets had a large wake at peak systole (point 4), due to failing to open completely. During flow deceleration, the fluid was more disrupted. RSS_{xz} was higher further downstream and the haemolysis threshold was exceeded. At point 5, vortices in the aortic sinus were noticed (Figure 112). On the YZ plane, the limit for platelet activation was always exceeded and the haemolysis threshold was exceeded from point 4 onwards. A maximum major RSS_{yz} value of 5 762 Pa was observed at valve closure. The RSS_{xy} results are smaller than the RSS_{xz} and RSS_{yz} results. RSS_{xy} remained below the platelet activation threshold (10 – 100 Pa) and only exceeded the lower limit of the threshold while closing.

The RSS results for bileaflet valves are often reported on the YZ plane (i.e. the longitudinal plane perpendicular to the leaflets' rotational axes; refer to Figure 57). The shear stress results of a 27 mm *SJM* bileaflet valve tested at 5 L/min CO are reported in [34]. Shear stress was monitored to 35 mm downstream. Maximum shear stress was observed at peak systole, 60 ms after peak systole and at valve closure. At these times, major RSS values of up to 71 Pa are reported and large regions of higher stress (> 30 Pa) are observed. In [30], RSS values of ~ 40 Pa are reported for a 23 mm *SJM* bileaflet valve tested at 4.5 L/min CO at peak systole. Higher shear stresses of 150 – 175 Pa on this plane for similar-sized bileaflet valves tested at similar conditions have been observed [14, 100]. On the central longitudinal plane parallel to the leaflets' rotational axes, higher shear stresses of 175 – 200 Pa have been reported for bileaflet valves (< 15 mm downstream) [14, 100]. The RSS results in §5.2.4 suggest that higher stresses can develop on the non-symmetry and axial planes as well as further downstream. In [100], it is stated that 2D analyses (i.e. 2D CFD or 2D PIV) can underestimate the maximum stress by up to 47%. For similar-sized tissue valves, maximum shear stresses of 347 Pa and 400 Pa on the XY plane have been measured [14, 160] and 2 600 Pa major RSS was measured for a 19 mm tissue valve (unspecified plane) [161]. In literature, it is not always specified whether the reported stress values refer to the maximum, coordinate invariant shear stress (i.e. major RSS), or not. In this report, the major RSS results are presented. It has been shown that the coordinate invariant shear stresses can be up to an order of magnitude larger [161].

The RSS_{xy} results of the prototype trileaflet valve are lower than the stress values from literature. The results compare favourably to the tissue valve results. However, the RSS_{yz} and RSS_{xz} results are high and indicate that platelets and erythrocytes will be damaged. In terms of magnitude, the results are most comparable to [161], where high major RSS were measured. The RSS_{yz} results were compared to the *TRI* valve results [149]. In [149], the shear stresses were measured using 2D PIV. The results compare well in terms of the stress development over the whole cardiac cycle, contours and locations of high stress. However, the stress magnitudes of the *TRI* valve are much lower than the values shown in Figure 79 and Figure 113. This could be due to the material specifications of the *TRI* valve, resulting in a slower, gradual closing motion, and manufacturing specifications, resulting in a greater extent of opening and less leaflet flutter. The 2D measured stress compared to the 3D computed stress can also be a contributing factor.

The RNS results were analysed. On the YZ plane, the Z-component of RNS was the same order of magnitude as the RSS and the Y-component was one to two orders of magnitude smaller. The same trend was observed on the XZ planes. On the XY plane, RNS was an order of magnitude larger than RSS. However, as stated in §2.3.4, threshold RNS values do not exist for platelet activation or haemolysis. Higher RNS have previously been reported [30, 32].

The maximum velocity (Figure 80) at peak systole is similar to the results discussed in §2.4. The maximum velocity at backflow is less than the steady state simulation results and published results (§2.4.3), due to the increased gap sizes. However, the results are of the same order of magnitude. Analysing the leakage jets more accurately requires a detailed microscale analysis without geometrical simplifications. The velocity profiles indicate central flow. The central jet is narrow, due to incomplete leaflet opening. Fluid flow is less uniform further downstream.

The leaflet shear force results are comparable to the leaflet shear force results of a dysfunctional bileaflet valve [109]. The comparison shows that the shear force exerted onto the leaflets of a trileaflet valve is not less than that of a bileaflet valve. However, the shear forces exerted on the leaflets are very small.

Maximum leaflet and housing WSS were observed during the flow acceleration phase (point 2 to 4). Maximum leaflet WSS developed on the edges on the upstream surface of the leaflets. The average leaflet WSS over the leading edges at peak systole was 109 Pa. At valve closure, maximum WSS developed on the trailing edges and the average maximum WSS was 88 Pa. At the edges, the threshold for platelet activation was exceeded. The WSS at peak systole will reduce if the extent of valve opening increases, which is likely to be achieved if a prototype is manufactured within the tolerance specifications.

The maximum housing WSS was observed on the leading and trailing edges of the hinge build-outs, the edges of the hinge recesses, downstream of the hinge regions and where the leaflets closely interface with the housing. The average maximum WSS at peak systole was 100 Pa. At valve closure, maximum housing WSS was observed in the region around the leaflets' leading edges. The average maximum WSS at valve closure was 31 Pa. The maximum housing WSS values are less than the bileaflet WSS results reported in [109]. WSS will further reduce if the edges of the hinge recesses and hinge build-outs are more streamlined and if the hinge build-outs are tapered towards the inlet and outlet.

The limitations of this CFD analysis should be noted. The simulated model did not exactly replicate the experimental setup. The CPD test setup was modelled as a straight, rigid pipe with a simplified sinus geometry and the leaflets were scaled to increase gap sizes. Turbulence was modelled using a RANS formulation. The effect of the fluid on the solid structure was not considered and the leaflets only had one degree of freedom. Despite these limitations, there was good correlation with the experimental results. Most of the results, except some of the major RSS values, are comparable to published results. This suggests that the hybrid CFD prescribed kinematics approach can be followed to account for asymmetries as well as other experimental variables and representative results can be obtained at a significantly lower computational cost than DNS or LES.

6   CONCLUSION

The primary aim of this study was to design a prototype mechanical HVR that improves on the hydrodynamic performance of commercial HVRs. This is of interest in developing countries, where a need for a durable, more affordable HVR exists. Considering flexible valves are currently unable to meet these requirements, mechanical HVRs remain the best solution for younger patients.

A literature review was conducted to 1) improve the understanding of the functioning and performance evaluation methods (*in vitro*, *in silico* and *in vivo*) of heart valves, 2) study the characteristics of commercial valves and 3) identify important HVR design features. The holistic design approach highlighted the complexity of valve design and detected leaflet and hinge geometries as well as manufacturing specifications as important aspects.

Using this knowledge, several trileaflet valve concepts were generated. Designs were restricted to the use of rigid materials. Different hinge mechanisms, sweep angles, leaflet curvatures and assembly methods were considered. The concepts were evaluated analytically to study the leaflet dynamics. Various manufacturing methods, focussing on AM, were investigated and initial prototypes were developed using SLA and DMLS technologies. The limitations in terms of dimensional accuracy, surface finish and material variation were considered and deemed appropriate for prototyping. The prototypes were subjected to preliminary pulsatile flow tests to 1) determine whether the valves meet the most important functional requirement, which is to open and close, and 2) assess the SLA and DMLS manufacturing methods. The results indicated that four valve designs, based on two hinge mechanisms and two valve profiles should be evaluated further. The structural integrity of the valves with different leaflet profiles under diastolic backpressure was assessed analytically and using FEM. Calculations were also performed to determine the safety factor under the impact load at closing. Based on the stress results and manufacturability, biocompatible titanium with a pyrolytic carbon coating is recommended for final product development.

SLA technology proved to be better than DMLS for prototyping. Considering the limitations of stereolithography, a reference bileaflet valve was also developed. This eliminated the effect of material and manufacturing differences on test results and enabled more accurate valve comparisons. An additional aim was to explore the use of AM for final product development. Although AM is advantageous in many ways, in its current state it does not seem to offer the complete solution for HVRs.

The hydrodynamic performances of the four prototype trileaflet valves and the benchmark bileaflet valve were evaluated experimentally and computationally. Using a CPD, the pressure gradient, EOA and regurgitant characteristics were determined. The trileaflet valves exhibited a performance equivalent to or exceeding that of the bileaflet valve but highlighted the shortcomings of the manufacturing procedure in one case. The tests revealed that the benchmark bileaflet valve was more prone to flutter, fracture and rebound upon closure. The leaflet opening and closing times and velocities were calculated based on the HSV data. The motion analysis showed significant cyclic variation, incomplete valve

opening, continuous movement and asymmetrical leaflet motion. Most of the trileaflet valves started closing before the bileaflet valve, suggesting that the vortices do influence valve closure. The closing times of the valves were comparable, but the 40° trileaflet 1 valve had the slowest closing time. However, due to the valve profile, the linear velocities at the leaflet tip were not slower than the bileaflet valve. Accounting for the asymmetries and large standard deviation, the linear velocities of the bileaflet and 40° trileaflet 1 valves were comparable.

The numerical evaluations indicated that trileaflet valves generate more physiologically representative flow fields, with less downstream disturbance and a uniform central jet. The study showed the importance of complete valve opening to create a more uniform flow field at peak systole. In terms of design, the housing length based on the *On-X* design proved to be suitable and the 40° trileaflet 1 valve demonstrated the best performance. However, geometries that should be streamlined were identified. The limitations of RANS models to investigate small-scale features were noted. The final prototype trileaflet valve was evaluated using a prescribed kinematics CFD approach. Ideal conditions were assumed, geometrical simplifications were made and only leaflet rotation was considered. The computed pressure gradient and EOA compared well to the experimental results and the velocities, leaflet forces and WSS showed good comparison to literature, instilling confidence in the computational model. The major RSS_{xy} results were below the platelet activation RSS threshold. However, high major RSS_{xz} and RSS_{yz} were computed. The large stresses are attributed to incomplete opening and excessive leaflet flutter as a result of manufacturing imprecision. Comparisons to literature are restricted due to the limited 2D RSS reported results.

A mechanical HVR design, evaluation and optimisation procedure, which can be implemented for future use, was developed. This strategy was developed by combining different technologies and collaborating with various stakeholders.

The study confirms the feasibility of the trileaflet valve concept. However, further investigation is required. Recommendations for future work are:

- Develop and test (CPD, HSV and updated prescribed kinematics CFD) a 40° trileaflet 1 valve that satisfies the final product material and manufacturing requirements and incorporates design recommendations. A comprehensive tolerance stack-up analysis should be conducted before commencement of production, keeping functional and performance requirements in mind.

- Detailed analysis of the hinge regions and the effect of small geometrical modifications and the two additional hinges of the trileaflet design compared to the bileaflet design on the flow parameters (microscale CFD analysis or experimental analysis).

- Further investigation of the use of overset meshes.

- RSS analysis on non-symmetrical and axial planes and whether there exists a need to develop a RNS criterion as a HVR performance metric.

- Standardisation of CPD setups to improve inter-laboratory comparability.

- Increase the sample size of the experimental motion analysis conducted with the use of a high-speed camera to reduce variability.

REFERENCES

[1] Ghanbari, H., Viatge, H., Kidane, A.G., Burriesci, G., Tavakoli, M. and Seifalian, A.M. (2009). Polymeric heart valves: new materials, emerging hopes. *Trends Biotechnol*, 27(6), pp. 359–367.

[2] Khan, S.S., Trento, A., DeRobertis, M., Kass, R.M., Sandhu, M., Czer, L.S., Blanche, C., Raissi, S., Fontana, G.P., Cheng, W. and Chaux, A. (2001). Twenty-year comparison of tissue and mechanical valve replacement. *J Thorac Cardiovasc*, 122(2), pp.257-269.

[3] International Organization for Standardization. (2015). Cardiovascular implants -- cardiac valve prostheses -- part 1: general requirements. (ISO 5840-1:2015).

[4] Brubert, J. (2016). *A novel polymeric prosthetic heart valve: design, manufacture, and testing*. (Doctoral dissertation, Queens' College).

[5] Goldbarg, S.H., Elmariah, S., Miller, M.A. and Fuster, V. (2007). Insights into degenerative aortic valve disease. *J Am Coll Cardiol*, 50(13), pp. 1205-1213.

[6] Nulu, S., Bukhman, G. and Kwan, G. F. (2017). Rheumatic heart disease: the unfinished global agenda. *Cardiol Clin*, 35(1), pp. 165–180.

[7] Jordaan, C.J. (2017). *Hydrodynamic and coagulation characteristics of a re-engineered mechanical heart valve in an ovine model*. (Doctoral dissertation, University of the Free State).

[8] Dasi, L.P., Simon, H.A., Sucosky, P. and Yoganathan, A.P. (2009). Fluid mechanics of artificial heart valves. *Clin Exp Pharmacol Physiol*, 36(2), pp. 225–237.

[9] Wium, E., Jordaan, C.J., Botes, L. and Smit, F.E. (2019). Alternative mechanical heart valves for the developing world. *Asian Cardiovasc Thorac Ann*, p.0218492319891255.

[10] Ayoub, S., Ferrari, G., Gorman, R.C., Gorman III, J.H., Schoen, F.J. and Sacks, M.S. (2011). Heart valve biomechanics and underlying mechanobiology. *Compr Physiol*, 6(4), pp.1743-1780.

[11] Texas Heart Institute. (n.d.). *Valve repair or replacement*. [online] Available at: https://www.texasheart.org/heart-health/heart-information-center/topics/valve-repair-or-replacement/ [Accessed 20 Jul. 2018].

[12] American Heart Association. (2018). *Options for heart valve replacement*. [online] Available at: http://www.heart.org/HEARTORG/Conditions/More/ HeartValveProblemsandDisease/Options-for-Heart-Valve-ReplacementM_ 450816_Article.jsp#.W1MMUdUzaM- [Accessed 20 Jul. 2018].

[13] Mohammadi, H. and Mequanint, K. (2011). Prosthetic aortic heart valves: modeling and design'. *Med Eng Phys*, 33(2), pp. 131–147.

[14] Yoganathan, A.P., He, Z. and Casey Jones, S. (2004). Fluid mechanics of heart valves. *Annul Rev Biomed Eng*, 6(1), pp. 331–362.

[15] Ho, S.Y. (2009). Structure and anatomy of the aortic root. *Eur J Echocardiogr*, 10(1), pp. i3-i10.

[16] Anatomy Sciences. (2018). *Aortic valve anatomy diagram how to assess aortic annular size before transcatheter aortic - anatomy sciences*. [online] Available at: http://anatomysciences.com/aortic-valve-anatomy-diagram/aortic-valve-anatomy-diagram-how-to-assess-aortic-annular-size-before-transcatheter-aortic/ [Accessed 25 Jul. 2018].

[17] By adh30 revised work by DanielChangMD who revised original work of DestinyQx; Redrawn as SVG by xavax - Wikimedia Commons: Wiggers Diagram.svg, CC BY-SA 4.0 [online] Available at: https://commons.wikimedia .org/w/index.php?curid =50317988 [Accessed 6 Aug. 2018].

[18] Yacoub, M. H. and Takkenberg, J. J. M. (2005). Will heart valve tissue engineering change the world? *Nat Clin Pract Cardiovasc Med*, 2(2), 60–61.

[19] Legg, M., Mathews, E. and Pelzer, R. (2012). The design and development of a stented tissue mitral and aortic heart valve. *Cardiovasc J Afr*, 23(3), pp. 126–130.

[20] Businesstech.co.za. (2019). *The 5 biggest medical aid schemes in SA – what they offer, and how much they cost in 2019*. [online] Available at: https://businesstech.co.za/news/finance/287446/the-5-biggest-medical-aid-schemes-in-sa-what-they-offer-and-how-much-they-cost-in-2019/ [Accessed 4 May 2019].

[21] Bestmed Medical Scheme. (2019). *Heart valve costs and incidence*. Data on file at Bestmed. Unpublished.

[22] Pibarot, P., Dumesnil, J.G., Cartier, P.C., Métras, J. and Lemieux, M.D. (2001). Patient-prosthesis mismatch can be predicted at the time of operation. *Ann Thorac Surg*, 71(5), pp.S265-S268.

[23] Yun, S.H., Sim, E.H., Goh, R.Y., Park, J.I. and Han, J.Y. (2016). Platelet activation: the mechanisms and potential biomarkers. *Biomed Res Int*.

[24] Ritchie, R. (1996). Fatigue and fracture of pyrolytic carbon: a damage-tolerant approach to structural integrity and life prediction in "ceramic" heart valve prostheses. *J Heart Valve Dis*, pp. 9–31.

[25] Travis, B.R., Marzec, U.M., Leo, H.L., Momin, T., Sanders, C., Hanson, S.R. and Yoganathan, A.P. (2001) 'Bileaflet aortic valve prosthesis pivot geometry influences platelet secretion and anionic phospholipid exposure', *Ann Biomed Eng*, 29(8), pp. 657–664.

[26] Simon, H.A., Leo, H.L., Carberry, J. and Yoganathan, A.P. (2004). Comparison of the hinge flow fields of two bileaflet mechanical heart valves under aortic and mitral conditions. *Ann Biomed Eng*, 32(12), pp. 1607–1617.

[27] Yin, W., Alemu, Y., Affeld, K., Jesty, J. and Bluestein, D. (2004). Flow-induced platelet activation in bileaflet and monoleaflet mechanical heart valves. *Ann Biomed Eng*, 32(8), pp. 1058–1066.

[28] Lu, P. C., Lai, H. C. and Liu, J. S. (2001). A reevaluation and discussion on the threshold limit for hemolysis in a turbulent shear flow. *J Biomech*, 34(10), 1361–1364.

[29] Raghav, V., Sastry, S. and Saikrishnan, N. (2018). Experimental assessment of flow fields associated with heart valve prostheses using particle image velocimetry (PIV): recommendations for best practices. *Cardiovasc Eng Technol*.

[30] Ge, L., Dasi, L.P., Sotiropoulos, F. and Yoganathan, A.P. (2008). Characterization of hemodynamic forces induced by mechanical heart valves: Reynolds vs. viscous stresses. *Ann Biomed Eng*, 36(2), pp. 276–297.

[31] Cengel, Y.A. and Ghajar, A.J. (2011). Heat and mass transfer: fundamentals and applications. McGraw-Hill Higher Education.

[32] Faghih, M.M. and Sharp, M.K. (2019). Modeling and prediction of flow-induced hemolysis: a review. *Biomech Model Mechan*, pp.1-37.

[33] Kuan, Y.H., Kabinejadian, F., Nguyen, V.T., Su, B., Yoganathan, A.P. and Leo, H.L. (2015). Comparison of hinge microflow fields of bileaflet mechanical heart valves implanted in different sinus shape and downstream geometry. *Comput Methods Biomech Biomedl Engin*, 18(16), pp.1785-1796.

[34] Li, C.P., Lo, C.W. and Lu, P.C. (2010). Estimation of viscous dissipative stresses induced by a mechanical heart valve using PIV data. *Ann Biomed Eng*, 38(3), pp.903-916.

[35] Grigioni, M., Daniele, C., D'Avenio, G. and Barbaro, V. (1999). A discussion on the threshold limit for hemolysis related to Reynolds shear stress. *J Biomech*, 32(10), pp.1107-1112.

[36] Morshed, K.N., Bark Jr, D., Forleo, M. and Dasi, L.P. (2014). Theory to predict shear stress on cells in turbulent blood flow. *PloS One*, 9(8), p.e105357.

[37] Siddiqui, R. F., Abraham, J. R., and Butany, J. (2009). Bioprosthetic heart valves: modes of failure. *Histopathology*, 55(2):135–44.

[38] Gott, V. L., Alejo, D. E. and Cameron, D. E. (2003). Mechanical heart valves: 50 years of evolution. *Ann Thorac Surg*, 76(6).

[39] Yoganathan, A.P., Woo, Y.R. and Sung, H.W. (1986). Turbulent shear stress measurements in the vicinity of aortic heart valve prostheses. *J Biomech*, 19(6), pp.433-442.

[40] Novostia.com. (2018). *Preclinical evidence*. [online] Available at: http://www.novostia.com/preclinical-evidence [Accessed 22 Sep. 2018].

[41] Roscardioinvest.ru. (n.d.). *Tri-leaflet 'TRICARDIKS' heart valve*. [online] Available at: http://roscardioinvest.ru/eng/index.php?id_subpart=5 [Accessed 22 Sep. 2018].

[42] Novostia.com. (2018). *A clinical application of recent basic discoveries*. [online] Available at: http://www.novostia.com/basic-discoveries [Accessed 22 Sep. 2018].

[43] Schubert, K., Schaller, T., Stojenthin, E., Stephan, C., Sievers, H.H. and Scharfschwerdt, M. (2018). A novel trileaflet mechanical heart valve: first *in vitro* results. *Interact Cardiovasc Thorac Surg*, 28(5), pp.689-694.

[44] Sato, M., Harasaki, H., Wika, K.E., Soloviev, M.V. and Lee, A.S. (2003). Blood compatibility of a newly developed trileaflet mechanical heart valve. *ASAIO J*, 49, pp. 117–122.

[45] Li, C.P. and Lu, P.C. (2012). Numerical comparison of the closing dynamics of a new trileaflet and a bileaflet mechanical aortic heart valve. *Artif Organs*, 15(4), pp.364-374.

[46] Meyer, L.C. and Goodenough, S.H., Mitral Medical International Inc. (1984). *Artificial heart valve*. U.S. Patent 4,446,577.

[47] Sievers, H.H. (2006). *Artificial heart valve*. U.S. Patent 6,991,649.

[48] Lu, P.C., Huang, R.H. and Chu, S.H., Tamkang Univ. (2005). *Tri-leaflet mechanical heart valve*. U.S. Patent 6,896,700.

[49] Milo, S. (1996). *Heart valve prostheses*. U.S. Patent 5,522,886.

[50] Amerio, O.N. and Schvezov, C.E., Clover Life Sciences Inc. (2017). *Trileaflet mechanical prosthetic heart valve*. U.S. Patent Application 14/870,049.

[51] Lapeyre, D. and Perrier, P., Lapeyre Group. (2000). *Mechanical valve prosthesis with optimized closing mode*. U.S. Patent 6,068,657.

[52] Lapeyre, D.M., Frazier, O.H., Conger, J.L., Macris, M.P., Perrier, P., Reul, H., Rolland, B., Clubb, J.F., Parnis, S.M. and Fuqua, J.M. (1994). *In vivo* evaluation of a trileaflet mechanical heart valve. *ASAIO J*, 40(3), pp.M707-13.

[53] Gregoric, I.D., Eya, K., Tamez, D., Cervera, R., Byler, D., Conger, J., Tuzun, E., Chee, H.K., Clubb, F.J., Kadipasaoglu, K. and Frazier, O.H. (2004). Preclinical hemodynamic assessment of a new trileaflet mechanical valve in the aortic position in a bovine model. *J Heart Valve Dis*, 13(2), pp.254-259.

[54] Gregoric, I., Conger, J.L., Reul, H., Tamez, D., Clubb Jr, F.J., Stainback, R.F., Hernandez, A., Cervera, R., Eya, K., Byler, D. and Kadipasaoglu, K.A. (2004). Preclinical assessment of a trileaflet mechanical valve in the mitral position in a calf model. *Ann Thorac Surg*, 77(1), pp.196-202.

[55] Gallegos, R.P., Rivard, A.L., Suwan, P.T., Black, S., Bertog, S., Steinseifer, U., Armien, A., Lahti, M. and Bianco, R.W. (2006). *In-vivo* experience with the Triflo trileaflet mechanical heart valve. *J Heart Valve Dis*, 15(6), pp. 791-799.

[56] Gregoric, I.D., Tamez, D., Eya, K., Clubb, F.J., Croitoru, M., Byler, D., Cervera, R., Conger, J.L., Kadipasaoglu, K.A. and Frazier, O.H. (2001). Comparison of a mechanical trileaflet valve to the bileaflet standard: a bovine model of aortic valve replacement. *ASAIO J*, 47(2), p.137.

[57] Kheradvar, A., Groves, E.M., Goergen, C.J., Alavi, S.H., Tranquillo, R., Simmons, C.A., Dasi, L.P., Grande-Allen, K.J., Mofrad, M.R., Falahatpisheh, A. and Griffith, B. (2015). Emerging trends in heart valve engineering: part ii. novel and standard technologies for aortic valve replacement. *Ann Biomed Eng*, 43(4), pp. 844–857.

[58] Bezuidenhout, D., Williams, D.F. and Zilla, P. (2015). Polymeric heart valves for surgical implantation, catheter-based technologies and heart assist devices. *Biomaterials*, 36, pp.6-25.

[59] Dasi, L.P., Ge, L., Simon, H.A., Sotiropoulos, F. and Yoganathan, A.P. (2007). Vorticity dynamics of a bileaflet mechanical heart valve in an axisymmetric aorta. *Phys Fluids*, 19(6), pp.067105 1-17.

[60] Lai, Y.G., Chandran, K.B. and Lemmon, J. (2002). A numerical simulation of mechanical heart valve closure fluid dynamics. *J Biomech*, 35(7), pp.881-892.

[61] On-X Life Technologies, Inc. (2015). *FDA approval: On-X aortic valves with less warfarin - On-X Life Technologies, Inc.* [online] Available at: https://www.onxlti.com/fda-approval-onx-aortic-less-warfarin/ [Accessed 3 Aug. 2018].

[62] Yanagawa, B., Levitsky, S., Puskas, J. D. and PROACT Investigators. (2015). Reduced anticoagulation is safe in high-risk patients with the *On-X* mechanical aortic valve*. Curr Opin Cardiol*, 30(2), 140-145.

[63] CryoLife, Inc. (n.d.). *Heart valve design & features - CryoLife, Inc.* [online] Available at: https://www.cryolife.com/products/on-x-heart-valves/heart-valve-design-features [Accessed 3 Aug. 2018].

[64] Hwang, N.H., Reul, H. and Reinhard, P. (1998). *In vitro* evaluation of the long-body *On-X* bileaflet heart valve. *J Heart Valve Dis*, 7(5), pp.561-568.

[65] Dumont, K., Vierendeels, J., Kaminsky, R., Van Nooten, G., Verdonck, P. and Bluestein, D. (2007). Comparison of the hemodynamic and thrombogenic performance of two bileaflet mechanical heart valves using a CFD/FSI model. *J Biomech Eng*, 129(4), 558-565.

[66] Leo, H., Simon, H.A., Dasi, L.P. and Yoganathan, A.P. (2006). Effect of hinge gap width on the microflow structures in 27-mm bileaflet mechanical heart valves. *J Heart Valve Dis*, 15(6), pp. 800–8.

[67] Alemu, Y., Girdhar, G., Xenos, M., Sheriff, J., Jesty, J., Einav, S. and Bluestein, D. (2010). Design optimization of a mechanical heart valve for reducing valve thrombogenicity - A case study with ATS valve. *ASAIO J*, 56(5), pp. 389–396.

[68] Govindarajan , V., Udaykumer, H. S. and Chandran, K. B. (2009). Two dimensional simulation of flow and platelet dynamics in the hinge region of a mechanical heart valve. *J Biomech Eng*, 131(3), pp. 1–23.

[69] Gross, J. M., Shu, M. C., Dai, F. F., Ellis, J., and Yoganathan, A. P. (1996). A microstructural flow analysis within a bileaflet mechanical heart valve hinge. *J Heart Valve Dis*, 5(6), 581-590.

[70] Gao, Z.B., Hosein, N., Dai, F.F. and Hwang, N.H. (1999). Pressure and flow fields in the hinge region of bileaflet mechanical heart valves. *J Heart Valve Dis*, 8(2), pp.197-205.

[71] Govindarajan, V., Udaykumar, H. S., and Chandran, K. B. (2009). Flow dynamic comparison between recessed hinge and open pivot bi-leaflet heart valve designs. *J Mech Med Biol*, 9(02), 161-176.

[72] King, M. J., David, T. and Fisher, J. (1997). Three-dimensional study of the effect of two leaflet opening angles on the time-dependent flow through a bileaflet mechanical heart valve. *Med Eng Phys*, 19(3), pp. 235–241.

[73] Lee, H., Homma, A. and Taenaka, Y. (2007). Hydrodynamic characteristics of bileaflet mechanical heart valves in an artificial heart: cavitation and closing velocity. *Artif Organs*, 31(7), pp. 532–537.

[74] Lee, H., Ikeuchi, Y., Akagawa, E., Tatsumi, E., Taenaka, Y. and Yamamoto, T. (2009). Effects of leaflet geometry on the flow field in three bileaflet valves when installed in a pneumatic ventricular assist device. *Artif Organs*, 12(2), pp.98-104.

[75] Grigioni, M., Daniele, C., D'Avenio, G. and Barbaro, V. (2001). The influence of the leaflets' curvature on the flow field in two bileaflet prosthetic heart valves. *J Biomech*, 34(5), pp.613-621.

[76] Grunkemeier, G.L., Li, H.H., Naftel, D.C., Starr, A. and Rahimtoola, S.H. (2000). Long-term performance of heart valve prostheses. *Curr Probl Cardiol*, 25(2), pp. 78–154.

[77] Ellis, J. T., Travis, B. R. and Yoganathan, A. P. (2000). An *in vitro* study of the hinge and near-field forward flow dynamics of the *St. Jude Medical* Regent bileaflet mechanical heart valve', *Ann Biomed Eng*, 28(5), pp. 524–532.

[78] International Organization for Standardization. (2009). Biological evaluation of medical devices -- part 1: evaluation and testing within a risk management process. (ISO 10993-1:2009).

[79] Ratner, B.D., Hoffman, A.S., Schoen, F.J. and Lemons, J.E. (2004). *Biomaterials science: an introduction to materials in medicine.* Elsevier.

[80] Mitamura, Y., Hosooka, K., Matsumoto, T., Otaki, K., Sakai, K., Tanabe, T., Yuta, T. and Mikami, T. (1989). Development of a ceramic heart valve. *J Biomater Appl.* 4(1), pp. 33–55.

[81] Zeng, H., Yin, W., Catausan, G., Moldovan, N. and Carlisle, J. (2016). Reprint of "ultrananocrystalline diamond integration with pyrolytic carbon components of mechanical heart valves." *Diamond and Related Materials*, 63, pp. 227–231.

[82] Grill, A. (2003). Diamond-like carbon coatings as biocompatible materials - an overview. *Diamond and Related Materials*, 12(2), pp. 166–170.

[83] Kostrzewa, B. and Rybak, Z. (2013). History, present and future of biomaterials used for artificial heart valves. *Polimery w medycynie*, 43(3), pp.183-189.

[84] Maccauro, G., RossiIommetti, P., Manicone, P. and Raffaelli, L. (2012). Zirconia and alumina bioceramic biocompatibility, *Nova Science Publishers, Inc.* Available at: https://www.scopus.com/inward/record.uri?eid=2-s2.0-84892057573&partnerID=40&md5=38ef11eb8bf1e7387699a8666ab9570d.

[85] Barsoum, M. and Barsoum, M.W. (2002). *Fundamentals of ceramics.* CRC press.

[86] Yao, W., Liu, J., Holland, T.B., Huang, L., Xiong, Y., Schoenung, J.M. and Mukherjee, A.K. (2011). Grain size dependence of fracture toughness for fine grained alumina. *Scr Mater*, 65(2), pp.143-146.

[87] Belenky, A., Bar-On, I. and Rittel, D. (2010). Static and dynamic fracture of transparent nanograined alumina. *J Mech Phys Solids*, 58(4), pp.484-501.

[88] Auerkari, P. (1996). *Mechanical and physical properties of engineering alumina ceramics.* Espoo: Technical Research Centre of Finland.

[89] YouTube. (2011). *SJM mechanical valve manufacturing.* [online] Available at: https://www.youtube.com/watch?v=gQvGlwM4lqs [Accessed 23 Nov. 2018].

[90] Scotten, L.N. and Siegel, R. (2015). Are anticoagulant independent mechanical valves within reach - fast prototype fabrication and *in vitro* testing of innovative bi-leaflet valve models. *Ann Transl Med*, 3(14).

[91] Engineering 103, Group 5. (2016). *Group 075-05: Trileaflet mechanical heart valve.* [online] Du2016-grp075-05.blogspot.com. Available at: http://du2016-grp075-05. blogspot.com/ [Accessed 20 Nov. 2018].

[92] Rodriguez, R. (2017). *Redesign and performance evaluation of a cardiac pulse duplicator.* (Master's thesis, Stellenbosch University).

[93] Nobili, M., Morbiducci, U., Ponzini, R., Del Gaudio, C., Balducci, A., Grigioni, M., Montevecchi, F.M. and Redaelli, A. (2008). Numerical simulation of the dynamics of a bileaflet prosthetic heart valve using a fluid–structure interaction approach. *J Biomech*, 41(11), pp.2539-2550.

[94] Klabunde, R. E. (2016). CV *Physiology | Vascular Compliance.* [online] Cvphysiology.com. Available at: https://www.cvphysiology.com/Blood%20 Pressure /BP004 [Accessed 25 Jul. 2018].

[95] Klabunde, R. E. (2015). CV *Physiology | Ventricular Compliance*. [online] Cvphysiology.com. Available at: https://cvphysiology.com/Cardiac%20 Function/CF014 [Accessed 25 Jul. 2018].

[96] Viscoelastic Impedance Adapter User Manual. (2015). [online] Available at: https://vivitrolabs.com/wp-content/uploads/2015/04/22846-A-Viscoelastic-Impedance-Adapter-VIA-User-Manual.pdf [Accessed 25 Jul. 2018].

[97] Jennings, L., Butterfield, M., Walker, P., Watterson, K. and Fisher, J. (2001). The influence of ventricular input impedance on the hydrodynamic performance of bioprosthetic aortic roots *in vitro*. *J Heart Valve Dis*, 10(2), pp.269-275.

[98] Retta, S.M., Kepner, J., Marquez, S., Herman, B.A. and Grossman, L.W. (2017). *In-Vitro* pulsatile flow measurement in prosthetic heart valves: An inter-laboratory comparison. *J Heart Valve Dis*, 26(1), pp.72-80.

[99] Feng, Z., Nakamura, T., Fujimoto, T. and Umezu, M. (2002). *In vitro* investigation of opening behavior and hydrodynamics of bileaflet valves in the mitral position. *Artif Organs*, 26(1), pp.32-39.

[100] De Tullio, M.D., Cristallo, A., Balaras, E. and Verzicco, R. (2009). Direct numerical simulation of the pulsatile flow through an aortic bileaflet mechanical heart valve. *J Fluid Mech*, 622, pp.259-290.

[101] Lu, P.C., Liu, J.S., Huang, R.H., Lo, C.W., Lai, H.C. and Hwang, N.H. (2004). The closing behavior of mechanical aortic heart valve prostheses. *ASAIO J*, 50(4), pp.294-300.

[102] Barbaro, V., Grigioni, M., Daniele, C. and Boccanera, G. (1970). Reconstruction of closing phase kinematics by motion analysis for a prosthetic bileaflet valve. *WIT Tr Biom Health*, 4.

[103] Robbe, C., Nsiampa, N., Oukara, A. and Papy, A. (2014). Quantification of the uncertainties of high-speed camera measurements. *Int J Metrol Qual Eng*, 5(2), p.201.

[104] Wei, Z.A., Sonntag, S.J., Toma, M., Singh-Gryzbon, S. and Sun, W. (2018). Computational fluid dynamics assessment associated with transcatheter heart valve prostheses: a position paper of the ISO working group. *Cardiovasc Eng Technol*, pp.1-11.

[105] Bluestein, D., Rambod, E. and Gharib, M. (2000). Vortex shedding as a mechanism for free emboli formation in mechanical heart valves. *J Biomech Eng*, 122(2), pp.125-134.

[106] Alemu, Y. and Bluestein, D. (2007). Flow-induced platelet activation and damage accumulation in a mechanical heart valve: numerical studies. *Artif Organs*, 31(9), pp.677-688.

[107] Grigioni, M., Daniele, C., Del Gaudio, C., Morbiducci, U., Balducci, A., D'avenio, G. and Barbaro, V. (2005). Three-dimensional numeric simulation of flow through an aortic bileaflet valve in a realistic model of aortic root. *ASAIO J*, 51(3), pp.176-183.

[108] Yokoyama, Y., Medart, D., Hormes, M., Schmitz, C., Hamilton, K., Kwant, P.B., Takatani, S., Schmitz-Rode, T. and Steinseifer, U. (2006). CFD simulation of a novel bileaflet mechanical heart valve prosthesis-an estimation of the Venturi passage formed by the leaflets. *Int J Artif Organs*, 29(12), pp.1132-1139.

[109] Khalili, F., Gamage, P. and Mansy, H.A. (2017). Hemodynamics of a bileaflet mechanical heart valve with different levels of dysfunction. *J Appl Biotechnol Bioeng* 2(5): 00044.

[110] Smadi, O., Hassan, I., Pibarot, P. and Kadem, L. (2010). Numerical and experimental investigations of pulsatile blood flow pattern through a dysfunctional mechanical heart valve. *J Biomech*, 43(8), pp.1565-1572.

[111] Ge, L., Jones, S.C., Sotiropoulos, F., Healy, T.M. and Yoganathan, A.P. (2003). Numerical simulation of flow in mechanical heart valves: grid resolution and the assumption of flow symmetry. *J Biomech Eng*, 125(5), pp.709-718.

[112] Redaelli, A., Bothorel, H., Votta, E., Soncini, M., Morbiducci, U., Del, C.G., Balducci, A. and Grigioni, M. (2004). 3-D simulation of the *St. Jude Medical* bileaflet valve opening process: fluid-structure interaction study and experimental validation. *J Heart Valve Dis*, 13(5), pp.804-813.

[113] Annerel, S., Degroote, J., Vierendeels, J., Claessens, T., Van Ransbeeck, P., Dahl, S.K., Skallerud, B., Hellevik, L.R., Segers, P. and Verdonck, P. (2012). Application of a strong FSI coupling scheme for the numerical simulation of bileaflet mechanical heart valve dynamics: study of wall shear stress on the valve leaflets. *Prog Comput Fluid Dy*, 12(2-3), pp.68-79.

[114] Su, B., Kabinejadian, F., Phang, H.Q., Kumar, G.P., Cui, F., Kim, S., San Tan, R., Hon, J.K.F., Allen, J.C., Leo, H.L. and Zhong, L. (2015). Numerical modeling of intraventricular flow during diastole after implantation of BMHV. *PloS One*, 10(5), p.e0126315.

[115] Nobili, M., Passoni, G. and Redaelli, A. (2007). Two fluid-structure approaches for 3D simulation of *St. Jude Medical* bileaflet valve opening. *J Appl Biomater Biom*, 5(1), pp.49-59.

[116] Nguyen, V.T., Kuan, Y.H., Chen, P.Y., Ge, L., Sotiropoulos, F., Yoganathan, A.P. and Leo, H.L. (2012). Experimentally validated hemodynamics simulations of mechanical heart valves in three dimensions. *Cardiovasc Eng Technol*, 3(1), pp.88-100.

[117] De Vita, F., De Tullio, M.D. and Verzicco, R. (2016). Numerical simulation of the non-Newtonian blood flow through a mechanical aortic valve. *Theor Comp Fluid Dyn*, 30(1-2), pp.129-138.

[118] Shu, M.C., Gross, J.M., O Rourke, K.K. and Yoganathan, A.P. (2003). An integrated macro/micro approach to evaluating pivot flow within the *Medtronic* Advantage bileaflet mechanical heart valve. *J Heart Valve Dis*, 12(4), pp.503-512.

[119] Yun, B.M., Aidun, C.K. and Yoganathan, A.P. (2014). Blood damage through a bileaflet mechanical heart valve: a quantitative computational study using a multiscale suspension flow solver. *J Biomech Eng*, 136(10), p.101009.

[120] Kaufmann, T.A., Linde, T., Cuenca-Navalon, E., Schmitz, C., Hormes, M., Schmitz-Rode, T. and Steinseifer, U. (2011). Transient, three-dimensional flow field simulation through a mechanical, trileaflet heart valve prosthesis. *ASAIO J*, 57(4), pp.278-282.

[121] Yeh, H.H., Grecov, D. and Karri, S. (2014). Computational modelling of bileaflet mechanical valves using fluid-structure interaction approach. *J Med Biol Eng*, 34(5), pp.482-486.

[122] Zakaria, M.S., Ismail, F., Tamagawa, M., Aziz, A.F.A., Wiriadidjaja, S., Basri, A.A. and Ahmad, K.A. (2017). Review of numerical methods for simulation of mechanical heart valves and the potential for blood clotting. *Med Biol Eng Comput*, 55(9), pp.1519-1548.

[123] Debus, K. (2018). *Saving lives: CFD simulation of a mechanical heart valve*. [online] Siemens PLM Community. Available at: https://community.plm. automation.siemens.com/t5/Simcenter-Blog/Saving-Lives-CFD-Simulation-of-a-Mechanical-Heart-Valve/ba-p/511064 [Accessed 22 Nov. 2018].

[124] Simon, H.A., Ge, L., Sotiropoulos, F. and Yoganathan, A.P. (2010). Numerical investigation of the performance of three hinge designs of bileaflet mechanical heart valves. *Ann Biomed Eng*, 38(11), pp.3295-3310.

[125] Jun, B.H., Saikrishnan, N. and Yoganathan, A.P. (2014). Micro particle image velocimetry measurements of steady diastolic leakage flow in the hinge of a *St. Jude Medical* Regent mechanical heart valve. *Ann Biomed Eng*, 42(3), pp.526-540.

[126] Saxena, R., Lemmon, J., Ellis, J. and Yoganathan, A. (2003). An *in vitro* assessment by means of laser Doppler velocimetry of the *Medtronic* Advantage bileaflet mechanical heart valve hinge flow. *J Thorac Cardiovasc Surg*, 126(1), pp.90-98.

[127] Rosenberger, M. R., Amerio, O., and Schvezov, C. (2005). Optimizing of the design of a prosthetic heart valve with three leaves. In *Fourth International Congress of Cardiology*. Available at: http://citeseerx.ist.psu.edu/ viewdoc /download?doi=10.1.1.594.9347&rep=rep1&type=pdf [Accessed 31 July 2018].

[128] Esquivel, C., Rosenberger, M., Gueijman, S., Schvezov, C., Amerio, O. and IOT, S.I. (2003). Design of a fourth generation prosthetic heart valve: tri-leaflet valve. In *Third Congress of Cardiology on the Internet*.

[129] Zhang, B.L., Bianco, R.W. and Schoen, F.J. (2019). Preclinical assessment of cardiac valve substitutes: current status and considerations for engineered tissue heart valves. *Front Cardiovasc Med*, 6.

[130] Quinn, R.W. (2013). Animal models for bench to bedside translation of regenerative cardiac constructs. *Prog Pediatr Cardiol*, *35*(2), pp.91-94.

[131] Janse van Rensburg, W.J. (2015). *Comparison of platelet receptors P2Y12, GPIIB/IIIA, GPVI, and GPIBα between the Cape chacma baboon and the human.* (Doctoral dissertation, University of the Free State).

[132] CryoLife, Inc. (n.d.). *On-X prosthetic heart valves*. [online] Available at: https://www.cryolife.com/products/on-x-heart-valves/ [Accessed 27 Feb. 2019].

[133] CryoLife, Inc. (n.d.). *Heart valve design & features*. [online] Available at: https://www.cryolife.com/products/on-x-heart-valves/heart-valve-design-features/ [Accessed 27 Feb. 2019].

[134] Suh, Y.J., Kim, Y.J., Hong, Y.J., Lee, H.J., Hur, J., Im, D.J., Kim, Y.J. and Choi, B.W. (2015). Measurement of opening and closing angles of aortic valve prostheses *in vivo* using dual-source computed tomography: comparison with those of manufacturers' in 10 different types. *Korean J Radiol*, 16(5), pp.1012-1023.

[135] Medtronic. (2011). *Medtronic Open Pivot mechanical heart valves*. [online] Available at: http://medtronic.webvertise.ro/medicalshop/upload/files/OPHV%20 NEW%20UC 201101694A_EN.pdf [Accessed 4 Feb. 2019].

[136] ViVitro Labs Inc. (2014). *Pulse duplicator system user manual*. No. 17473 V1.3.

[137] Wium, E., Davis, K., Müller, J.H., and Smit, F.E. (2019). *The effect of ventricular compliance on pulse duplicator test results*. [Poster]. Heart Valve Society's Annual Scientific Meeting, 11 – 13 April 2019, Barcelona, Spain.

[138] Davis, K., Wium, E., Müller, J.H., Meyer, C.J. and Smit, F.E. (2019). *Combining experimental and computational techniques to evaluate the shear stress through an artificial heart valve.* [Poster]. Heart Valve Society's Annual Scientific Meeting, 11 – 13 April 2019, Barcelona, Spain.

[139] De Lazzari, C., Marconi, S., Oelofse, A., Wium, E., Smit, F.E., Papa, S., Badagliacca, R. (accepted). *E-learning and research experience between Italy and South Africa using in vitro and in silico left circulatory cardiovascular system*. [Presentation]. Bio Medical Engineering Conference, 1 – 2 June 2020, Stockholm, Sweden.

[140] Brookshier, K.A. and Tarbell, J.M. (1993). Evaluation of a transparent blood analog fluid: aqueous xanthan gum/glycerin. *Biorheology*, 30(2), pp.107-116.

[141] Verdonck, P.R., Nooten, G.V. and Belleghem, Y.V. (1997). Pulse duplicator hydrodynamics of four different bileaflet valves in the mitral position*. Cardiovascular Surgery*, 5(6), pp.593-603.

[142] Mascherbauer, J., Schima, H., Rosenhek, R., Czerny, M., Maurer, G. and Baumgartner, H. (2004). Value and limitations of aortic valve resistance with particular consideration of low flow–low gradient aortic stenosis: an *in vitro* study. *Eur Heart J*, 25(9), pp.787-793.

[143] Mathew, P. (2010). *A comparison of hemodynamic performance in mechanical and biological heart valve prostheses*. (Master's thesis, University of Tennessee at Chattanooga).

[144] Medtronic. (n.d.). *Medtronic Open Pivot heart valve*. [online] Available at: https://dmec.moh.gov.vn/documents/10182/7760461/upload_00271176_15283 59091579.pdf?version=1.0&fileId=7766645 [Accessed 30 June 2019].

[145] Laske, A., Jenni, R., Maloigne, M., Vassalli, G., Bertel, O. and Turina, M.I., (1996). Pressure gradients across bileaflet aortic valves by direct measurement and echocardiography. *Ann Thorac Surg*, 61(1), pp.48-57.

[146] Tracker - Video Analysis and Modeling Tool. (2019). Open Source Physics. [online] Available at: https://physlets.org/tracker/.

[147] Mirkhani, N., Davoudi, M.R., Hanafizadeh, P., Javidi, D. and Saffarian, N. (2016). On-X heart valve prosthesis: numerical simulation of hemodynamic performance in accelerating systole. *Cardiovasc Eng Technol*, 7(3), pp.223-237.

[148] Annerel, S., Degroote, J., Claessens, T., Dahl, S.K., Skallerud, B., Hellevik, L.R., Van Ransbeeck, P., Segers, P., Verdonck, P. and Vierendeels, J. (2012). A fast strong coupling algorithm for the partitioned fluid–structure interaction simulation of BMHVs. *Comput Methods Biomech Biomed Eng*, 15(12), pp.1281-1312.

[149] Li, C.P., Chen, S.F., Lo, C.W. and Lu, P.C. (2011). Turbulence characteristics downstream of a new trileaflet mechanical heart valve. *ASAIO J*, 57(3), pp.188-196.

[150] Matweb.com. (n.d.). *Graphite, Carbon, C.* [online] Available at: http://www.matweb.com/search/DataSheet.aspx?MatGUID=3f64b985402445c 0a5af911135909344&ckck=1 [Accessed 6 Aug. 2019].

[151] Matweb.com. (n.d.). *Victrex™ PEEK 650P PolyEtherEtherKetone.* [online] Available at: http://www.matweb.com/search/datasheet.aspx?matguid=62a7 727e4e1a455cb 3fe7ca32f9a9860 [Accessed 6 Aug. 2019].

[152] De Tullio, M.D., Pascazio, G., Weltert, L., De Paulis, R. and Verzicco, R. (2011). Evaluation of prosthetic-valved devices by means of numerical simulations. *Philos Trans Royal Soc A*, 369(1945), pp.2502-2509.

[153] Vingmed.dk. (2017). *LivaNova: ascending aortic prostheses.* [online] Available at: https://www.vingmed.dk/wp-content/uploads/sites/3/2019/03/Carbomedic-Carbo -Seal-Valsalva1.pdf [Accessed 7 Sep. 2019].

[154] Vascutek Ltd (2019). *Gelweave Valsalva.* [online] Vascutek.com. Available at: https://www.vascutek.com/site/assets/files/3497/gelwvalsalva_trifold_b331-2e.pdf [Accessed 20 Mar. 2019].

[155] Mathur, M., Saxena, A., Shad, R. and Chattoraj, A. (2017). Computational evaluation of the haemodynamic performance of a novel prosthetic heart valve. In: *ASME 2017 International Design Engineering Technical Conferences and Computers and Information in Engineering Conference.* 6 – 9 August 2017. American Society of Mechanical Engineers Digital Collection.

[156] Chandran, K.B. and Aluri, S. (1997). Mechanical valve closing dynamics: relationship between velocity of closing, pressure transients, and cavitation initiation. *Ann Biomed Eng*, 25(6), pp.926-938.

[157] Siemens. (2018). *Simcenter STAR-CCM+: Documentation* (Version 13.04). Siemens PLM Software, Texas, United States of America.

[158] Hund, S.J., Antaki, J.F. and Massoudi, M. (2010). On the representation of turbulent stresses for computing blood damage. *Int J Eng Sci*, 48(11), pp.1325-1331.

[159] CHPC wiki. (Updated on 09/09/2019). *CHPC quick start guide.* [online] Available at: http://wiki.chpc.ac.za/quick:start#overview32_832_cores [Accessed 4 Oct. 2019].

[160] Lim, W.L., Chew, Y.T., Chew, T.C. and Low, H.T. (2001). Pulsatile flow studies of a porcine bioprosthetic aortic valve *in vitro*: PIV measurements and shear-induced blood damage. *J Biomech*, 34(11), pp.1417-1427.

[161] Davis, K. (2018). *Numerical and Experimental Investigation of the Hemodynamics of an Artificial Heart Valve.* (Master's thesis, Stellenbosch University).

[162] Snikhovska, K. (n.d.). *Seven types of 3D printers - different printing and extruder technologies.* [online] Pen and Plastic. Available at: https://penandplastic.com/3d-printer-types/ [Accessed 15 Mar. 2019].

[163] Formlabs.com. (2017). *SLA vs. DLP: a 3D printing technology comparison.* [online] Available at: https://formlabs.com/blog/3d-printing-technology-comparison -sla-dlp/ [Accessed 15 Mar. 2019].

[164] Pires, R. (2018). *DLP vs SLA – 3D printing technologies shootout | All3DP.* [online] All3DP. Available at: https://all3dp.com/2/dlp-vs-sla-3d-printing-technologies-shootout/ [Accessed 15 Mar. 2019].

Appendix A   DESIGN AND PROTOTYPE DEVELOPMENT

A.1   Failure Modes, Effects and Criticality Analysis

The aim of the FMECA was to identify critical design aspects to aid in developing a reliable design. The severity and probability of each failure mode were classified according to Table 16 and Table 17 respectively (both reproduced from [3]). The criticality number is the product of the severity and probability scores. The analysis is presented in Table 18.

Table 16:   **FMECA - severity classification**

Effect	Severity	Description
Catastrophic	7	Probable patient death regardless of intervention
	6	Probable patient death without immediate intervention
Critical	5	Possible patient death or probable permanent disabling injury regardless of intervention
	4	Possible patient death or probable permanent disabling without immediate intervention
Serious	3	Possible permanent impairment of bodily function
Minor	2	Possible temporary impairment of bodily function
Negligible	1	Slight or no potential for patient injury

Table 17:   **FMECA - probability classification**

Effect	Probability	Description
Very high	7	Causes occur often
High	6	Causes occur sometimes
Moderately high	5	Causes occur sometimes
Medium	4	Causes occur infrequently
Low	3	Causes occur infrequently
Very low	2	Causes occur rarely
Remote	1	Causes not expected to occur

Table 18: **FMECA of the prototype trileaflet aortic HVR**

Part	Failure Mode	Failure Effect	Severity	Failure Cause	Probability	Failure Detection / Design verification	Criticality
Housing	Rough or porous surface	Platelet adherence (leading to a thromboembolic event), calcification	4	Incorrect surface tolerance specification, presence of surface impurities, poor quality control	2	Correct surface specification, suitable manufacturing processes, quality control measures	8
	Fracture	Embolism	5	Brittle material, presence of stress raisers (e.g. cracks, voids, impurities or geometrical discontinuities)	1	Stress analysis (first order calculations, FEA), fatigue testing	5
	Large clearances at the hinges	Leakage	3	Poor design, incorrect manufacturing specifications or procedures	2	Tolerance analysis, correct tolerance specification, characterisation of the accuracy of manufacturing processes	6
	Hinge regions	Hinges that allow for a large range of motion resulting in a large closing volume, hinges that do not facilitate slow, gentle closure generating high levels of stress in the fluid and structural components and noise, geometrical discontinuities resulting in flow stasis	4	Poor design, incorrect manufacturing specifications or procedures	3	Good hinge design and design reviews, tolerance analysis, CFD, *in vitro* tests, flow visualisation (PIV, HSV analysis)	12
	Profile that promotes turbulence	Platelet activation and thrombus formation, haemolysis	4	Poor design, incorrect manufacturing specifications or procedures	1	Design reviews, CFD, flow visualisation	4
	Bio-incompatible material	Thrombus formation due to platelet reaction to foreign material, calcification, material degradation	4	Incorrect material specification	1	Select ISO 10993-1 compliant material	4

Part	Failure Mode	Failure Effect	Severity	Failure Cause	Probability	Failure Detection / Design verification	Criticality
Leaflet	Rough or porous surface	Platelet adherence, calcification	4	Incorrect surface tolerance specification, poor quality control	1	Correct tolerance specification, suitable manufacturing process, quality control, inspection	4
	Fracture	Embolism	5	Locations of stress concentration, load exceeding design, weak / brittle material	2	Stress analysis, fatigue testing	10
	Leaflet escape	Embolism	6	Locations of stress concentration, brittle material, incorrect tolerance specification, poor hinge design	2	Stress analysis, fatigue testing, *in vitro* testing, tolerance analysis	12
	Unable to close or insufficient sealing	Leakage	4	Poor design, incorrect tolerance specification, inaccurate manufacturing process, poor quality control	2	*In vitro* testing, tolerance analysis, characterisation of the accuracy of manufacturing processes, quality control	8
	Unable to open completely	Large pressure drop, reduced EOA	4	Tight fits, tissue overgrowth, calcification	2	*In vitro* testing, tolerance analysis, axially extended housing to limit tissue growth	8
	Bio-incompatible material	Thrombus formation due to platelet reaction to foreign material, calcification, material degradation	4	Incorrect material specification	1	Select ISO 10993-1 compliant material	4
	Profile that results in a large closing volume	Regurgitation	4	Poor design, incorrect manufacturing specifications or procedures	2	Design reviews, CFD, *in vitro* testing, flow visualisation	8
	Profile that promotes turbulence	Platelet activation and thrombus formation, haemolysis	4	Poor design, incorrect manufacturing specifications or procedures	2	Design reviews, CFD, *in vitro* testing, flow visualisation	8

A.2   Prototype Development

From the onset of the project, it was envisioned that AM technology will be utilised to develop a functional model of the valve for concept evaluation purposes. AM can be employed effectively to expedite the product development process by allowing the comparison of multiple design concepts and rapid implementation of design changes. This is generally more cost- and time-efficient than conventional manufacturing methods. AM also offers more flexibility; it is not limited in terms of design complexity in the same way as conventional machining methods.

For AM technologies, the resolution and quality of the print are dependent on the printing technology and machine specifications. To produce high quality parts, experimentation and characterisation of the machine are required. Different AM technologies, namely fused deposition modelling (FDM), stereolithography and laser-sintering, were investigated for prototype development. For each type of process, test pieces were manufactured to gauge the accuracy of the machine. There was experimentation in terms of part orientation, location of support structures, clearances, wall thickness, materials, scaling and machine-specific settings.

FDM printers operate by melting a solid filament and depositing a thin layer of the melted material on a build platform [162]. Upon deposition, the material cools and solidifies. Layer-by-layer, a solid part is formed. Figure 84 shows photographs of the test pieces using different FDM printers. It was established that FDM was not suitable for this application.
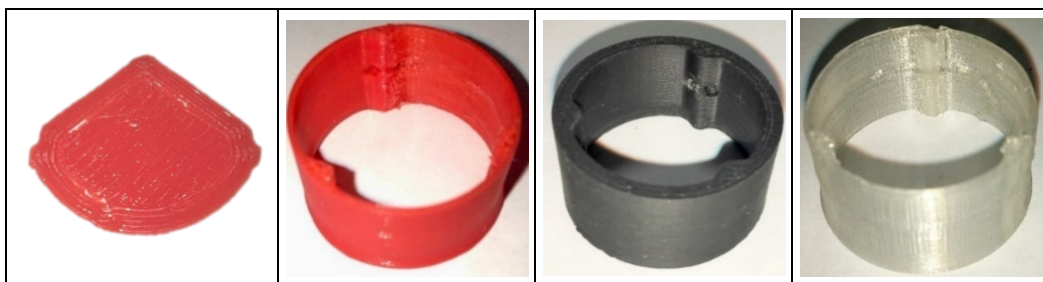

Figure 84:   FDM test pieces

Stereolithography, also known as resin printing, is an AM technology that uses ultra-violet light to solidify a liquid photosensitive resin, layer-by-layer. The light source can either be in the form of a laser beam, which is known as SLA, or a projector, which is known as digital light processing (DLP) [162 – 164]. In SLA printers, the laser rapidly traces the entire cross-section of the part, hardening the resin as it moves. In DLP printers, the whole layer of resin is exposed to the ultra-violet light and hardened at once. After fabrication, the part is further cured. Resin printers can create more accurate and precise parts than other AM methods. SLA printers can achieve smoother surface finishes compared to DLP printers. In DLP parts, the individual layers are more distinct. The main post-processing that was required for stereolithography-based parts was improving the surface roughness at the locations of the support structure attachments. SLA and DMLS parts are

shown in Figure 28 and Figure 85 respectively. DLP parts were manufactured at CRPM. Note the rougher surfaces of the DLP parts.
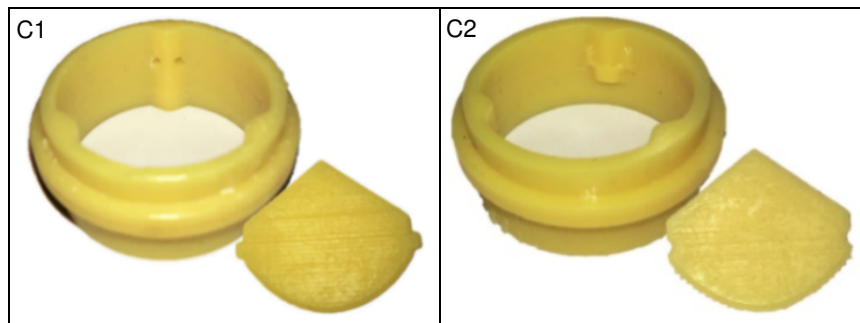

Figure 85:   DLP test pieces

Laser-sintering is a process whereby a laser melts and fuses a powder into a solid, as the laser traces the cross-section of the part in sequential layers [162]. If a metallic powder is used, it is referred to as DMLS. Metal additive manufactured parts have very rough surfaces, therefore post-processing of is an integral part of the manufacturing procedure. DMLS test pieces, which were manufactured at CRPM, are shown in Figure 28 and Figure 86.

To be able to specify manufacturing tolerances, the accuracy of the machine had to be quantified. The titanium laser-sintering machine at CRPM has not previously been characterised in terms of machining accuracy (for dimensions ≤ 50 μm). This is crucial for heart valve applications. A tolerance gauge was designed and scanned using computed tomography (CT) to assess the accuracy of the machine. Figure 86 shows some of the parts. Through an iterative process, the impact of small design changes and different printing orientations on the print quality and the valve assembly and operation were evaluated until a functional valve was manufactured.

To improve the surface finish of the metal AM parts, the parts were first shot peened and then subjected to a variety of sanding and polishing methods that included the use of power tools and manual operations (e.g. sandpaper, water paper, honing stones, needle files). Some of the post-processed leaflets are shown in Figure 28. The process required some investigation to determine how much material can be removed. This was especially difficult without the use of precision measurement techniques. Furthermore, it was impossible to access small-scale features (i.e. the interior of the recessed hinges and the small features of the protruding hinges). Surface roughness at the hinges is critical to reduce friction, thereby facilitating smooth motion and reducing wear, and to improve the haemocompatibility.
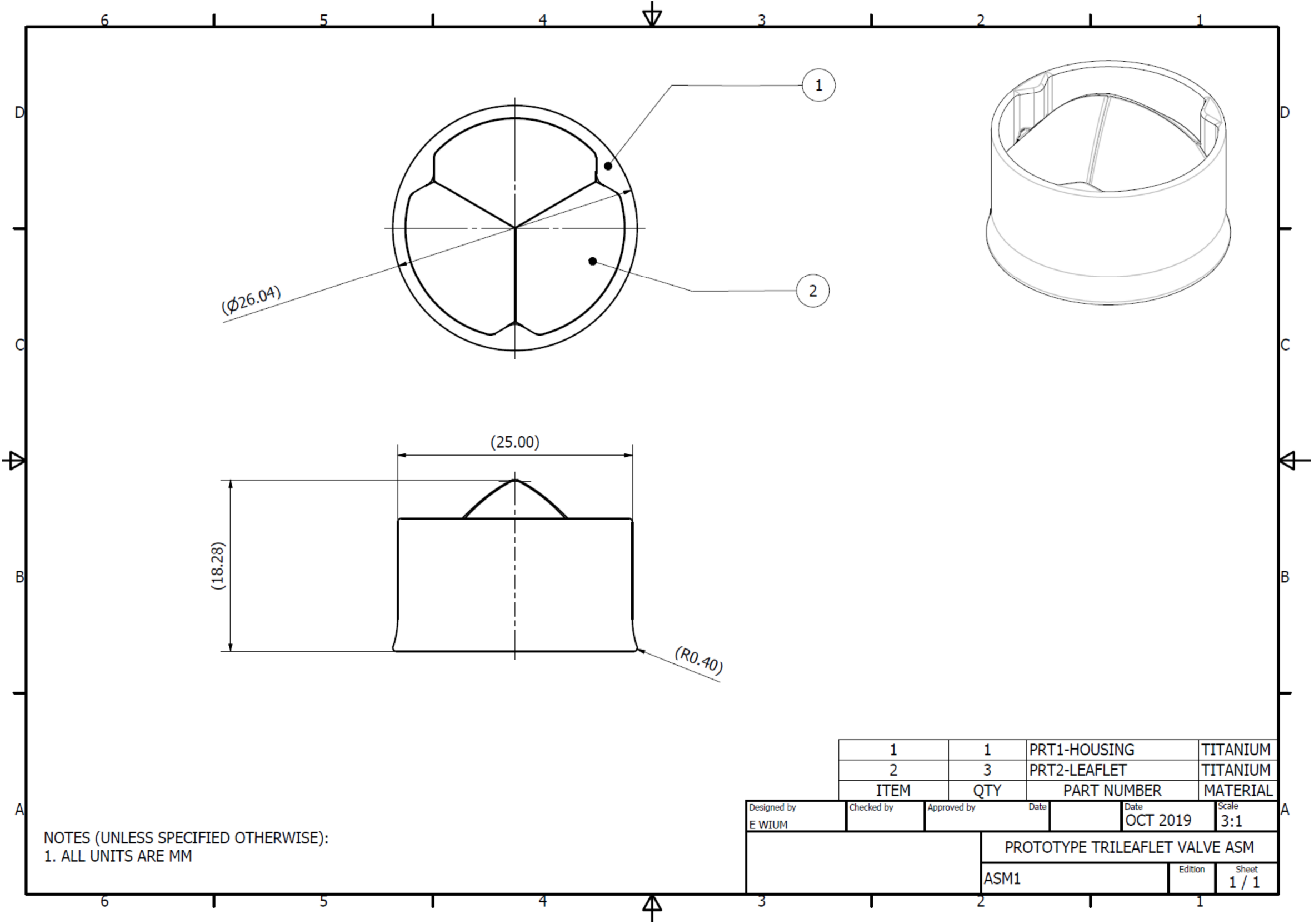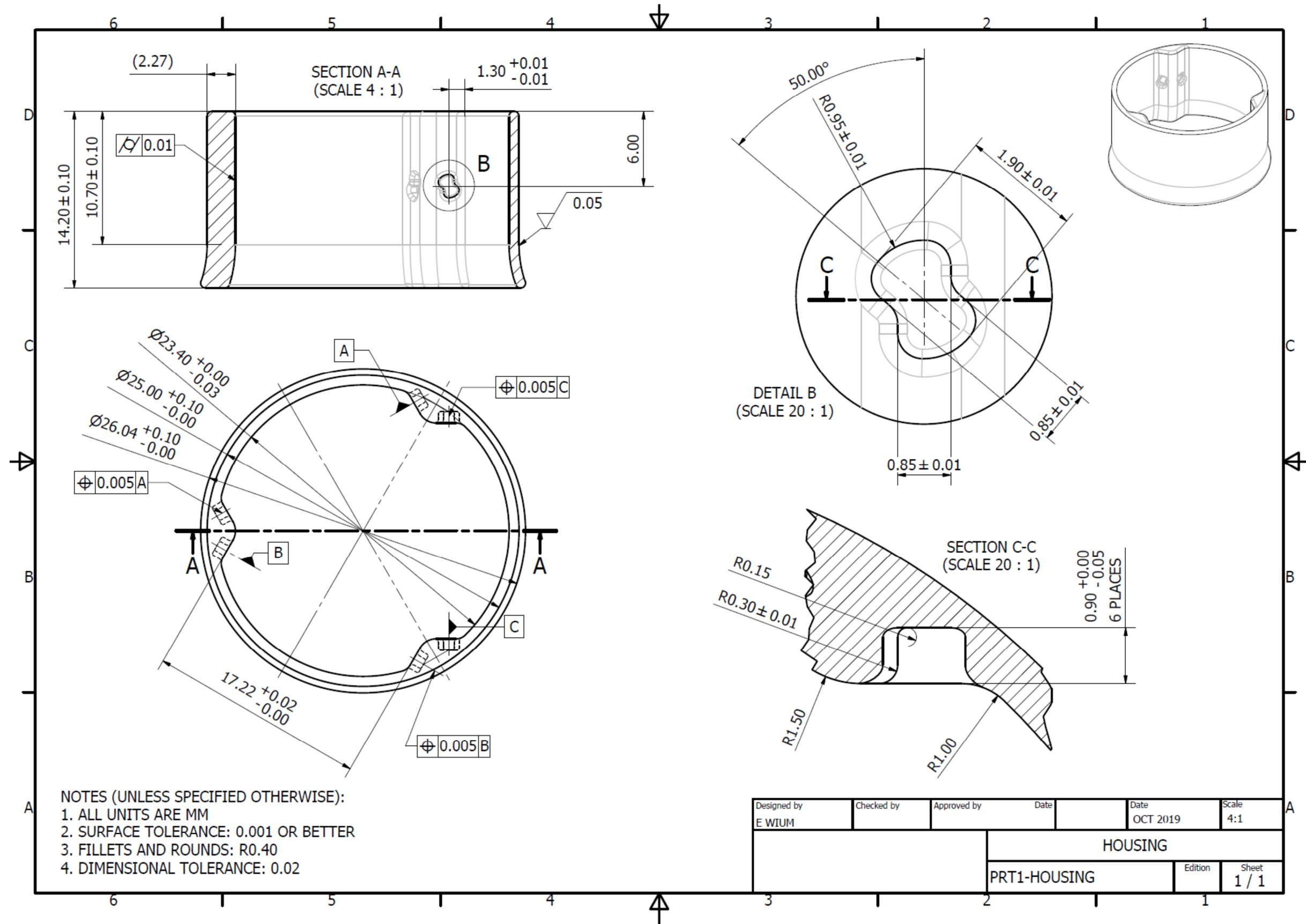
Figure 86:   **DMLS test pieces (characterisation phase)**

Conventional machining methods (waterjet and laser cutting) were also investigated. However, due to the cost and time of precision manufacturing techniques, conventional manufacturing did not seem to present a viable solution for testing multiple prototypes. The parts were limited to simpler designs (e.g. flat leaflets).

An alternative type of rapid prototyping process, vacuum casting, was considered as a potential solution for the direct comparison of prototype trileaflet valves to commercial bileaflet valves. The vacuum casting process involves creating a silicone mould using a master part, which is typically a SLA part. A polyurethane resin is poured into the mould under vacuum and set to oven-cure. Once solidified, the casting is easily removed from the mould and the mould can be reused. The cast parts have smooth surface finishes. The casting resin can be mixed with a metal filler powder to alter the mechanical properties of the part, for example to match the material properties (in terms of density) of commercial valves. However, this option was not further pursued.

			PART NUMBER	MATERIAL
1	1	PRT1-HOUSING	TITANIUM
2	3	PRT2-LEAFLET	TITANIUM
ITEM	QTY	PART NUMBER	MATERIAL

Designed by	Checked by	Approved by	Date	Date	Scale
E WIUM				OCT 2019	3:1

PROTOTYPE TRILEAFLET VALVE ASM

	Edition	Sheet
ASM1		1 / 1

NOTES (UNLESS SPECIFIED OTHERWISE):
1. ALL UNITS ARE MM

SECTION A-A
(SCALE 4 : 1)

(2.27)

1.30 +0.01 / -0.01

14.20 ± 0.10

10.70 ± 0.10

6.00

⌀ 0.01

0.05

B

50.00°

R0.95 ± 0.01

1.90 ± 0.01

0.85 ± 0.01

DETAIL B
(SCALE 20 : 1)

C   C

0.85 ± 0.01

⌀23.40 +0.00 / -0.03

⌀25.00 +0.10 / -0.00

⌀26.04 +0.10 / -0.00

⊕ 0.005 C

⊕ 0.005 A

⊕ 0.005 B

17.22 +0.02 / -0.00

A   A

A

B

C

SECTION C-C
(SCALE 20 : 1)

R0.15

R0.30 ± 0.01

R1.50

R1.00

0.90 +0.00 / -0.05
6 PLACES

NOTES (UNLESS SPECIFIED OTHERWISE):
1. ALL UNITS ARE MM
2. SURFACE TOLERANCE: 0.001 OR BETTER
3. FILLETS AND ROUNDS: R0.40
4. DIMENSIONAL TOLERANCE: 0.02

Designed by	Checked by	Approved by	Date	Date	Scale
E WIUM				OCT 2019	4:1

HOUSING

PRT1-HOUSING		Edition	Sheet
			1 / 1

50.00°

(3.92)

17.22 $^{+0.00}_{-0.01}$

0.005
2 PLACES

(15.32)

11.61 $^{+0.00}_{-0.01}$

1.37

0.80

A

⊥ 0.005 A

(1.68)

B

R0.4

50.00°

1.60 $^{+0.00}_{-0.02}$

∥ 0.005 B

∥ 0.005 B

R19.88

○ 0.005

R1.00

0.80 $^{+0.00}_{-0.01}$

R11.82 $^{+0.00}_{-0.05}$

R1.00

R1.00

18.82 $^{+0.01}_{-0.00}$

NOTES (UNLESS SPECIFIED OTHERWISE):
1. ALL UNITS ARE MM
2. SURFACE TOLERANCE: 0.001 OR BETTER
3. FILLETS AND ROUNDS: R0.40
4. DIMENSIONAL TOLERANCE: 0.02

Designed by	Checked by	Approved by	Date	Date	Scale
E WIUM				OCT 2019	5:1

LEAFLET

PRT2-LEAFLET		Edition	Sheet
			1 / 1

Appendix C   EXPERIMENTAL EVALUATION

C.1   Pulsatile Flow Tests

The ventricular and aortic pressure and aortic flow rate waveforms for each test are displayed in Figure 87 to Figure 93.
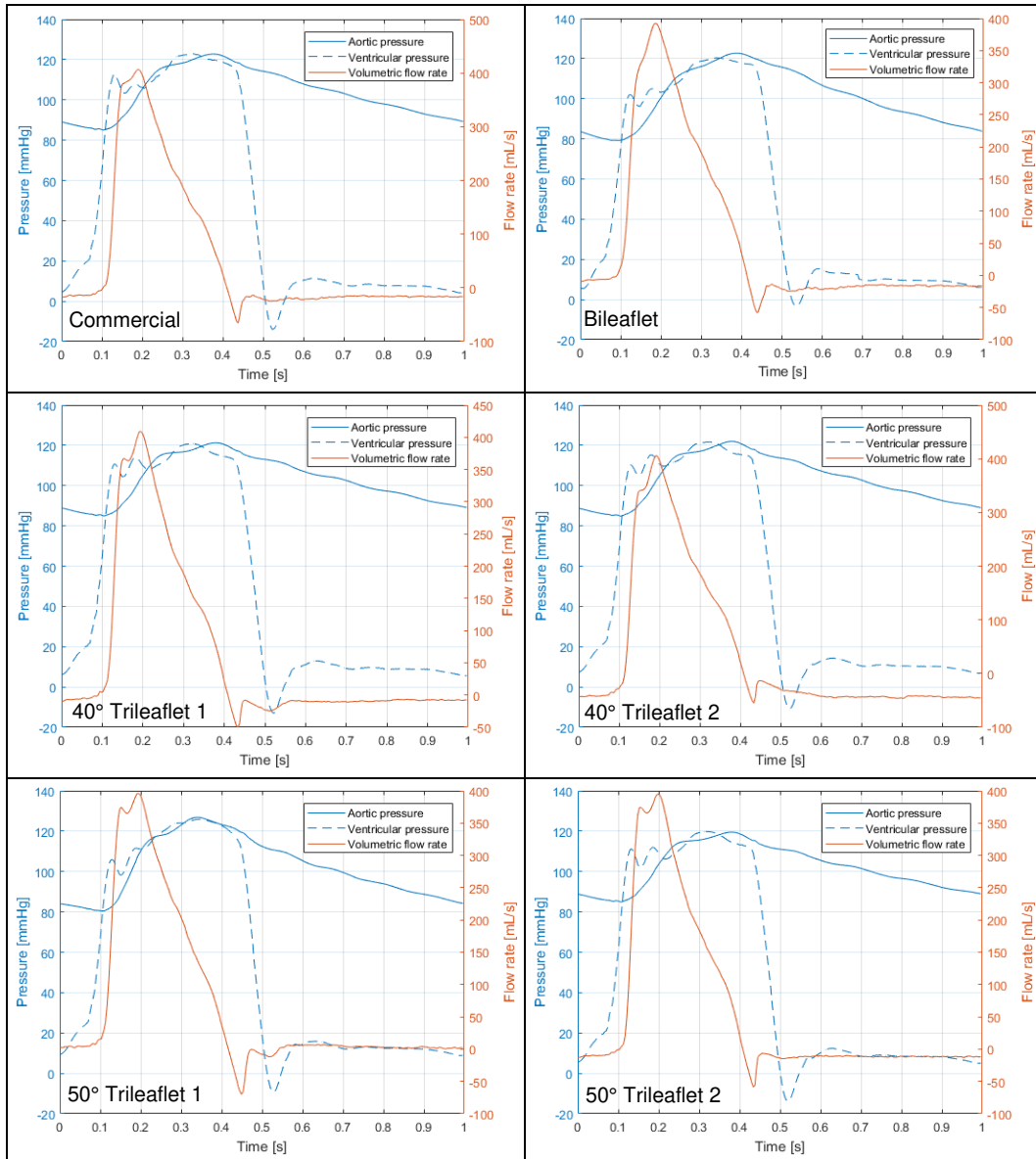
Figure 87:   Test 1 - CPD pressure and flow waveforms
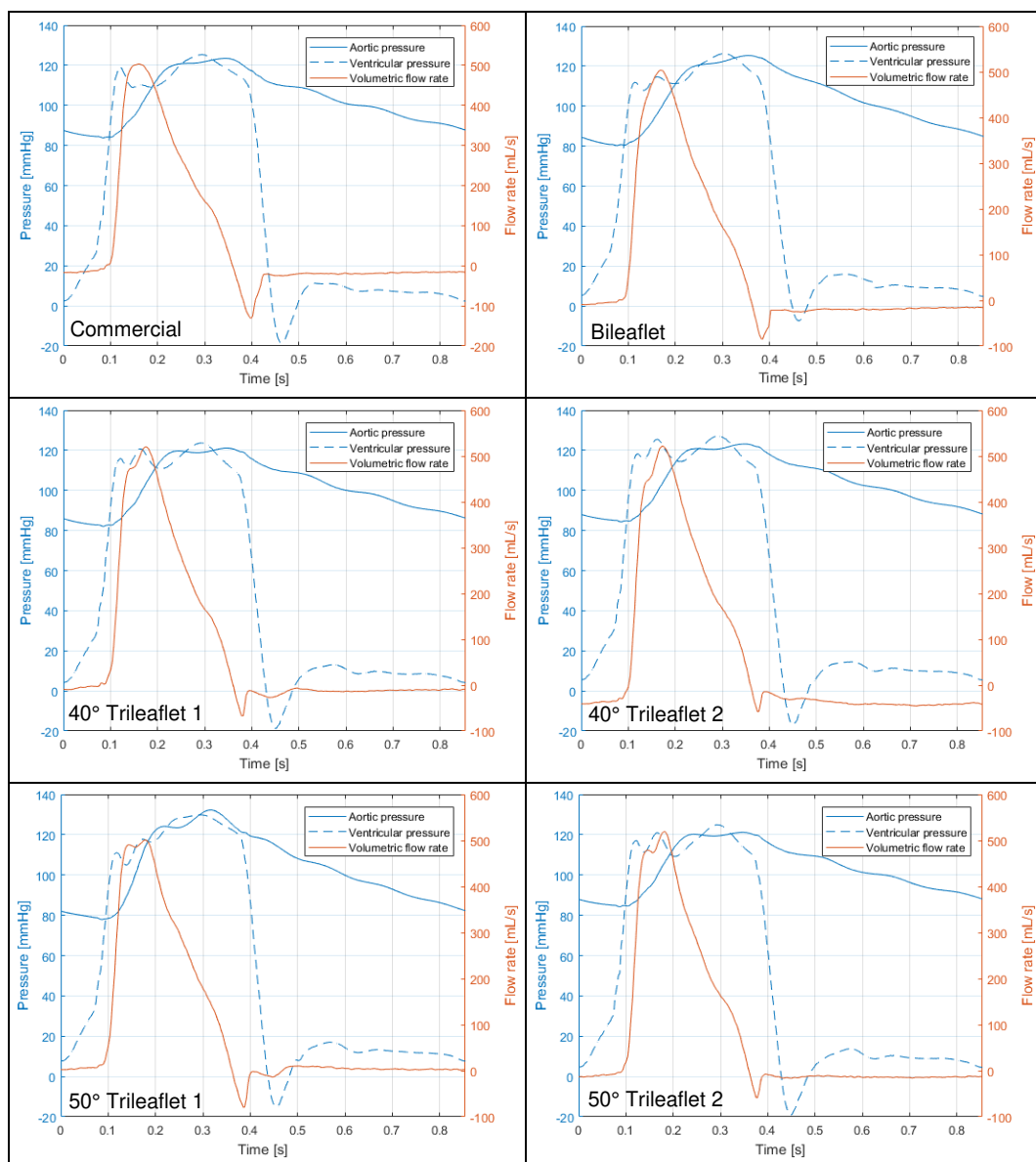
Figure 88:   Test 2 - CPD pressure and flow waveforms
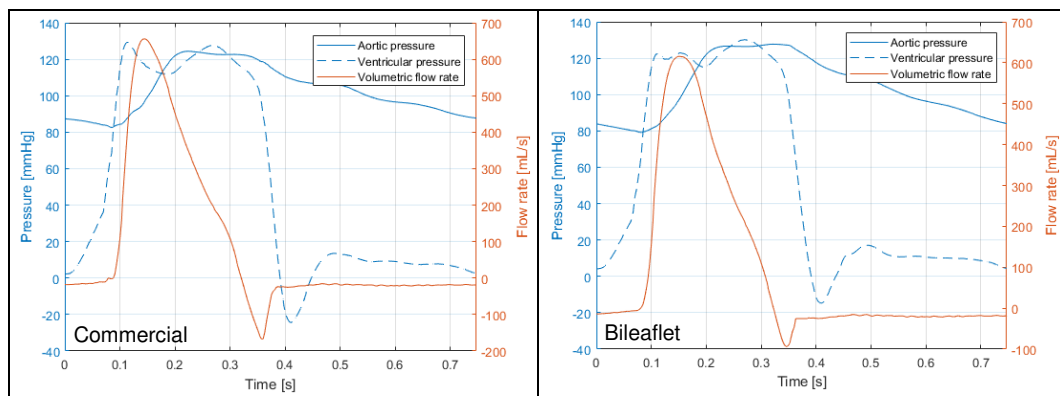
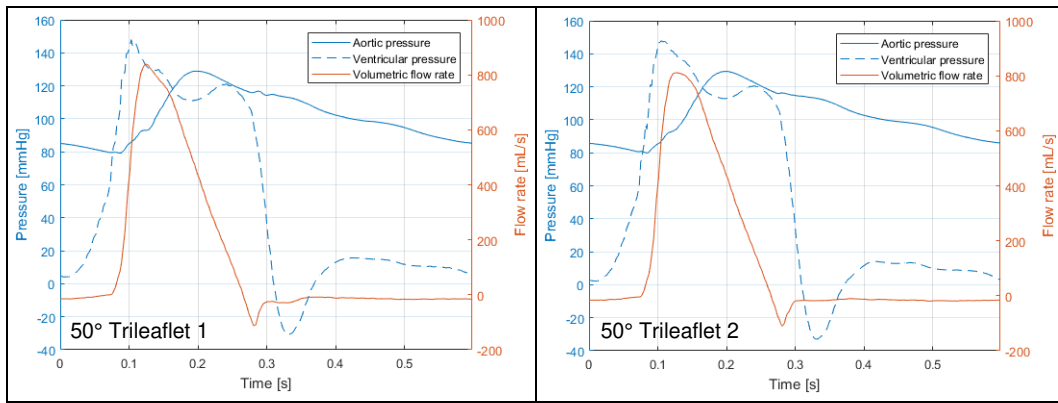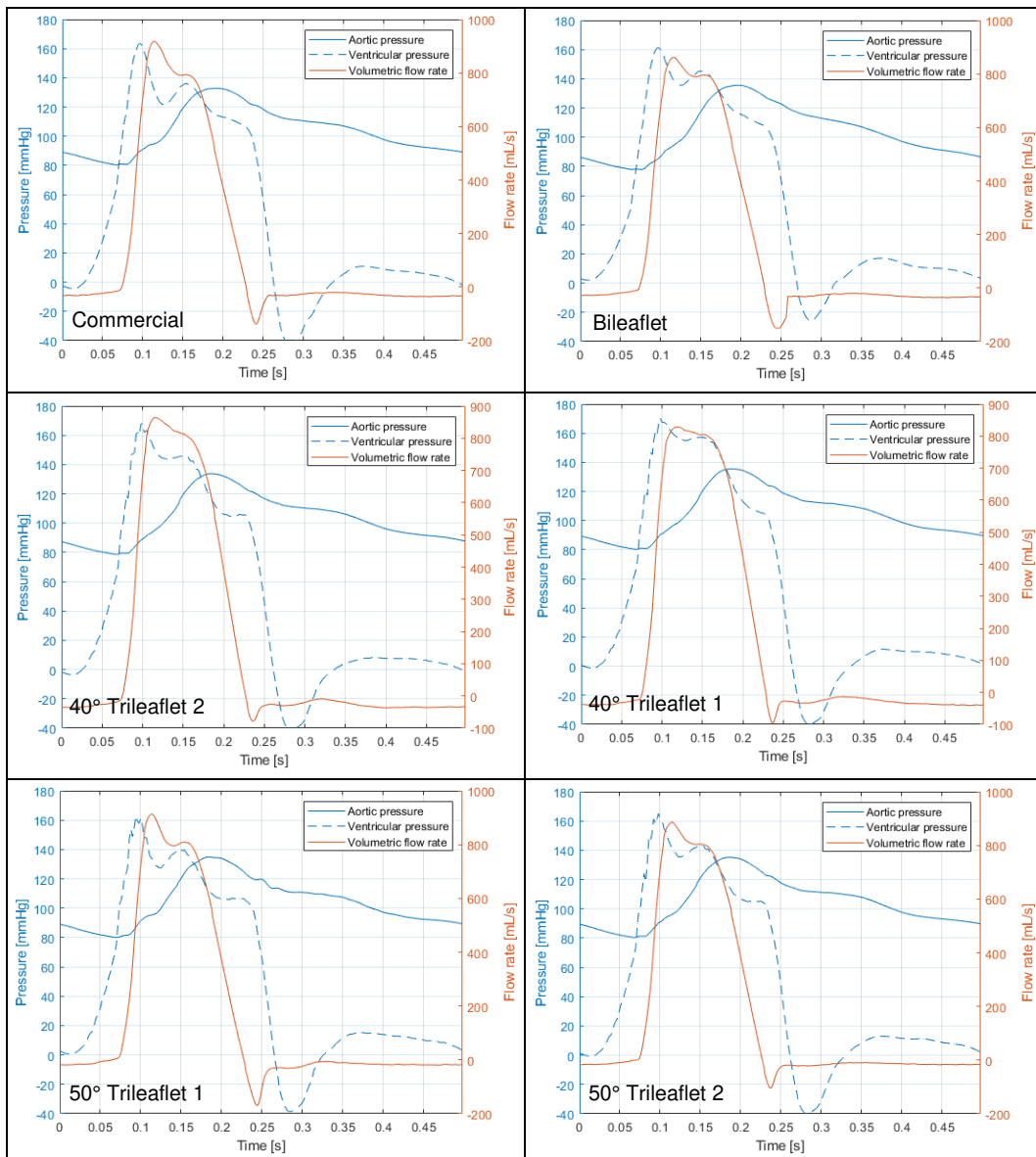**Figure 89:   Test 3 - CPD pressure and flow waveforms (1)**
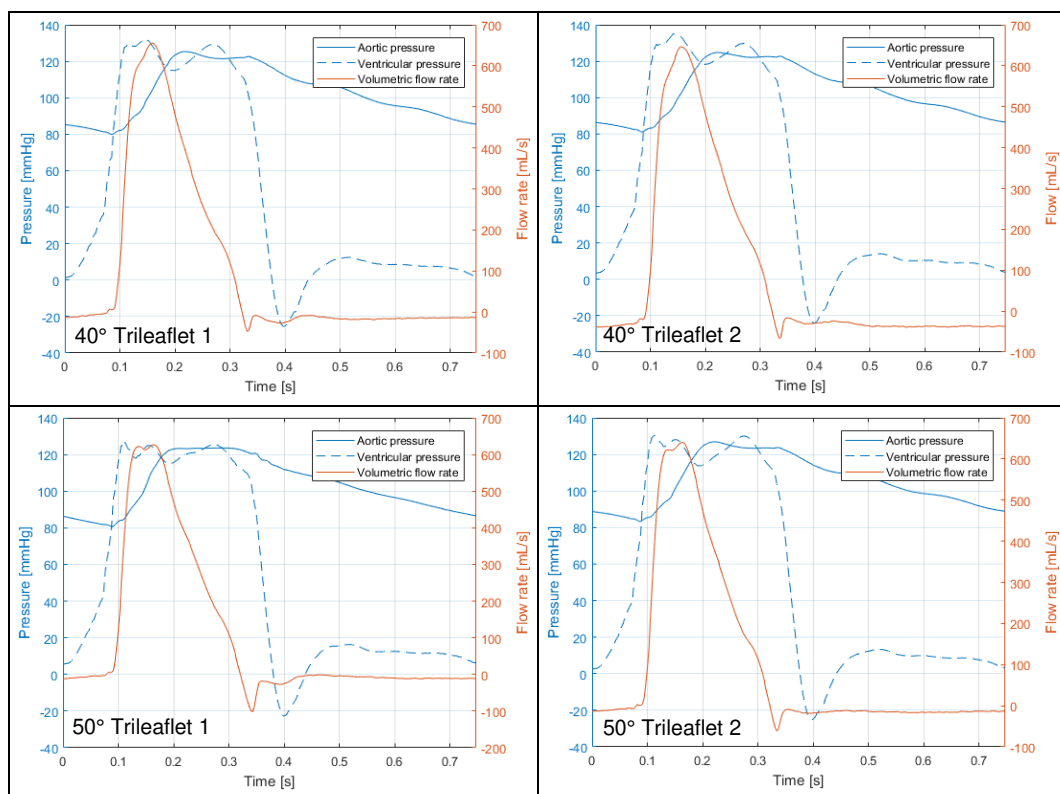
Figure 90: Test 3 - CPD pressure and flow waveforms (2)
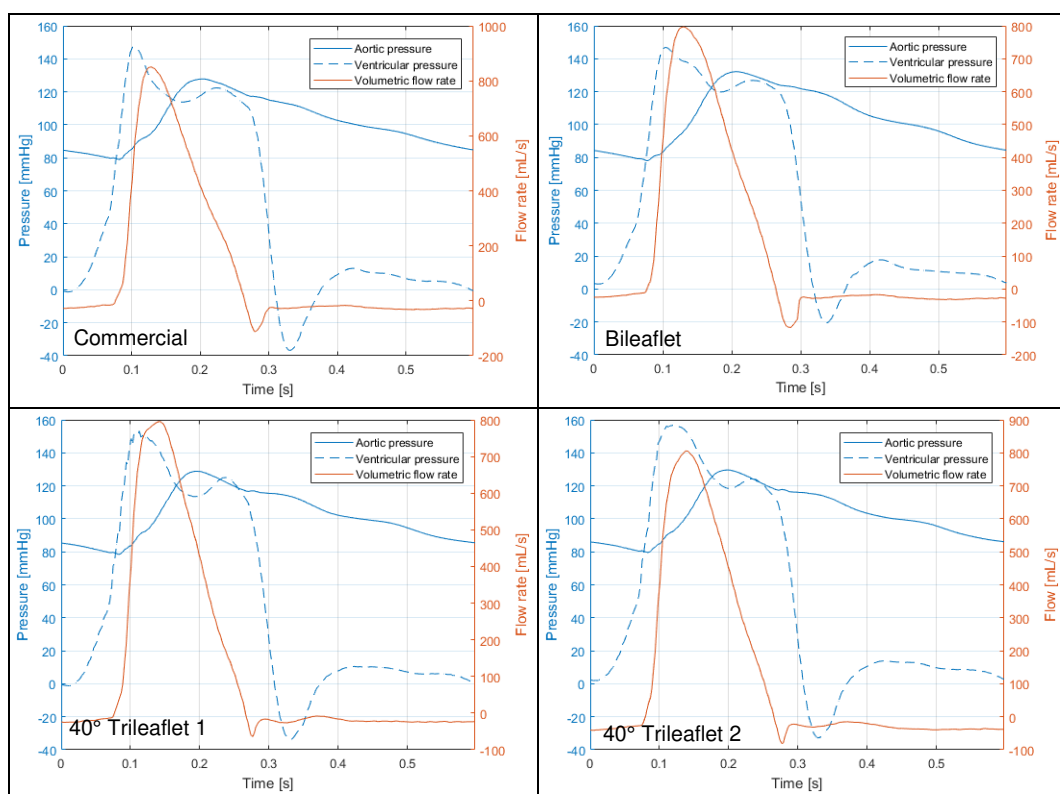
Figure 91: Test 4 - CPD pressure and flow waveforms (1)

Figure 92:   Test 4 - CPD pressure and flow waveforms (2)

Figure 93:   Test 5 - CPD pressure and flow waveforms

The measured average output parameters are shown in Figure 94. Figure 94 confirms that the pulsatile flow tests were conducted in accordance with ISO 5840 and under approximately equivalent load conditions.
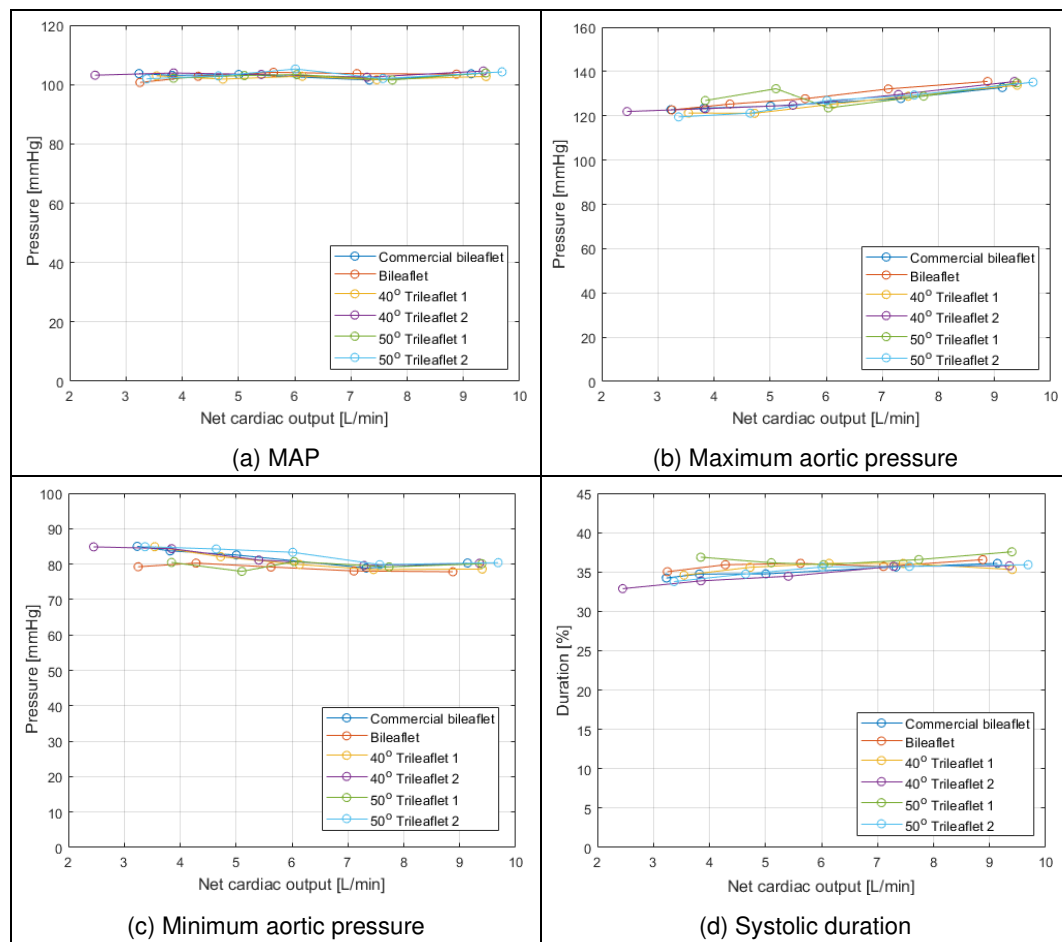
Figure 94:   Average CPD test output parameters as a function of CO

C.2   High-Speed Video Tests

Figure 95 and Figure 96 describe the total / average and maximum / fastest velocity calculations.
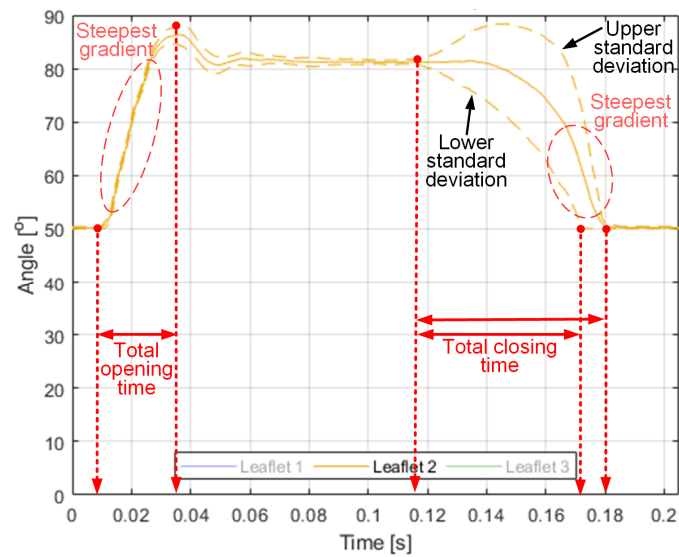
Figure 95:   Description of the HSV velocity calculations
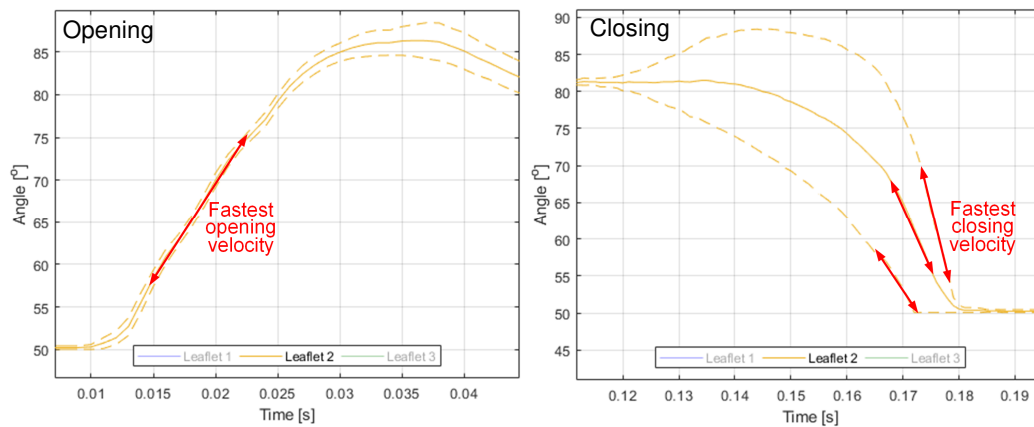
Figure 96:   Detailed description of maximum HSV velocity calculations

Appendix D   COMPUTATIONAL FLUID DYNAMICS

D.1   Conservation Equations

Differential form of the conservation equations of mass, momentum and energy are presented in Equation 7 to Equation 12.

Continuity:

$$\frac{\partial \rho}{\partial t} + \partial_i(\rho u_i) = 0 \tag{7}$$

$$\rho = \text{density}$$
$$t = \text{time}$$
$$u_i = \text{velocity}$$

Conservation of momentum:

$$\frac{\partial \rho u_i}{\partial t} + \partial_j\left(u_j \rho u_i\right) = -\partial_i P + \partial_j \tau_{ji} + \rho F_i \tag{8}$$

$$P = \text{pressure}$$
$$\tau_{ji} = \text{viscous stress tensor}$$
$$F_i = \text{body force vector}$$

For a Newtonian fluid:

$$\partial_j \tau_{ji} = -\frac{2}{3}\partial_i\left(\mu(\partial_k u_k)\right) + 2\,\partial_j\left(\mu S_{ij}\right) \tag{9}$$

$$S_{ij} = \frac{1}{2}\partial_i u_j + \frac{1}{2}\partial_j u_i \tag{10}$$

$$S_{ij} = \text{strain rate tensor}$$
$$\mu = \text{viscosity}$$

Momentum equations in Cartesian coordinates for a Newtonian fluid with constant density and constant viscosity:

$$\rho\left(\frac{\partial u_x}{\partial t} + u_x\frac{\partial u_x}{\partial x} + u_y\frac{\partial u_x}{\partial y} + u_z\frac{\partial u_x}{\partial z}\right) = \mu\left(\frac{\partial^2 u_x}{\partial x^2} + \frac{\partial^2 u_x}{\partial y^2} + \frac{\partial^2 u_x}{\partial z^2}\right) - \frac{\partial P}{\partial x} + \rho g_x$$

$$\rho\left(\frac{\partial u_y}{\partial t} + u_x\frac{\partial u_y}{\partial x} + u_y\frac{\partial u_y}{\partial y} + u_z\frac{\partial u_y}{\partial z}\right) = \mu\left(\frac{\partial^2 u_y}{\partial x^2} + \frac{\partial^2 u_y}{\partial y^2} + \frac{\partial^2 u_y}{\partial z^2}\right) - \frac{\partial P}{\partial y} + \rho g_y \tag{11}$$

$$\rho\left(\frac{\partial u_z}{\partial t} + u_x\frac{\partial u_z}{\partial x} + u_y\frac{\partial u_z}{\partial y} + u_z\frac{\partial u_z}{\partial z}\right) = \mu\left(\frac{\partial^2 u_z}{\partial x^2} + \frac{\partial^2 u_z}{\partial y^2} + \frac{\partial^2 u_z}{\partial z^2}\right) - \frac{\partial P}{\partial z} + \rho g_z$$

Conservation of energy:

$$\frac{\partial}{\partial t}\left[\rho\left(e + \frac{1}{2}u^2\right)\right] + \partial_i\left[\rho u_i\left(e + \frac{1}{2}u^2\right)\right] = -\partial_i q_i + \rho u_i F_i + \partial_j\left(T_{ij}u_j\right) \tag{12}$$

$$q_i = \text{heat flux vector}$$
$$T_{ji} = \text{stress tensor}$$

D.2   Discretised Conservation Equations

The conservation equations are converted from differential equations to a set of algebraic equations using the finite volume method. The algebraic equations are solved with a multigrid solver. For transient simulations, the total time is divided into an arbitrary number of time steps. The size of the time step is problem-dependent and affects the stability of the solution. Implicit solvers are unconditionally stable; however, the time step affects the accuracy of the results. The time step size is governed by the Courant-Friedrichs-Lewy (CFL) number. At each time step an inner iterative loop was conducted ten times.

Each conservation equation is written in the form of a general transport equation, defined in Equation 13, by integrating over a control volume [157]. The control volumes are 3D polyhedral elements that do not overlap and discretise the entire fluid domain (with prismatic cells at the wall boundaries). The general transport equation is.

$$\frac{d}{dt}\int_V \rho\phi dV + \int_S \rho\mathbf{v}\phi d\mathbf{a} = \int_S \Gamma\nabla\phi d\mathbf{a} + \int_V S_\phi dV \qquad (13)$$

$$\phi = \text{any scalar property (e. g. u, v, w or E)}$$
$$V = \text{control volume}$$
$$S = \text{surface area of control volume}$$
$$\mathbf{a} = \text{surface vector}$$
$$\Gamma = \text{diffusion coefficient}$$

The terms of the transport equation are the 1) transient term, which refers to the time rate of change of fluid property, ϕ, within the control volume, 2) convective flux term, which is the rate of decrease of the fluid property as a result of convection across the control volume's boundaries, 3) diffusive flux term, which is the rate of increase of the fluid property as a result of diffusion across the control volume's boundaries and 4) Source / sink term, representing the creation / loss of the fluid property within the control volume.

For each cell, the surface integrals are solved by the product of the quantity of interest at the midpoint of the cell face and the surface area of the cell face and summing over all the faces of the cell. The cell face centre is the area-weighted centre of the face. If the quantity at the centre of the cell face is not known, the value is approximated from adjacent cell centre values by interpolation (second order accurate methods). Variable gradients at cell- and face centres are calculated using a hybrid Gauss-least squares method. The source / sink term is calculated as the product of the average creation / loss value within the cell and the volume of the cell. This results in the semi-discrete transport equation (Equation 14).

$$\frac{d}{dt}\rho\phi V = -\sum \rho\phi(\mathbf{v}\cdot\mathbf{a}) + \sum \Gamma\nabla\phi\cdot\mathbf{a} + S_\phi V \qquad (14)$$

The transient term is solved implicitly (first order accurate):

$$\frac{d}{dt}\rho\phi V = \frac{(\rho\phi V)^{n+1} - (\rho\phi V)^{n}}{\Delta t} \tag{15}$$

The updated transported variable at cell P, ϕ_p, is solved by:

$$\phi_p{}^{k+1} = \phi_p{}^{k} + \Delta\phi_p \tag{16}$$

Where:

$$\frac{a_p}{\omega}\Delta\phi_p + \sum_N a_N\Delta\phi_N = R \tag{17}$$

$$\Delta\phi_p = \frac{\omega}{a_p}\left(R - \sum_N a_N\Delta\phi_N\right)$$

$$\omega = \text{under relaxation factor}$$
$$a_p, a_N = \text{coefficients obtained from the discretised terms}$$
$$N = \text{all the neighbouring cells of cell p}$$
$$R = \text{residual}$$

The residual, which is zero for the exact solution, is the transport equation:

$$R = -\left[\frac{d}{dt}\rho\phi V + \sum \rho\phi(\mathbf{v}\cdot\mathbf{a}) - \sum \Gamma\nabla\phi\cdot\mathbf{a} - S_\phi V\right] \approx 0 \tag{18}$$

The linear algebraic equations can be written in matrix form, $\mathbf{Ax} = \mathbf{b}$, and solved using an iterative method, namely Gauss-Seidel. $\mathbf{A}$ is the matrix of coefficients (a_p, a_N), $\mathbf{x}$ is the vector of unknowns $(\Delta\phi_p)$ and $\mathbf{b}$ is the residual vector (R). Using a segregated solver, the mass and momentum conservation equations are solved sequentially.

For transient problems, the algorithm iterates to converge at each time step (inner loop) before progressing to the next time step (outer loop) until the solution end time is reached. The solution procedure is shown in Figure 97.
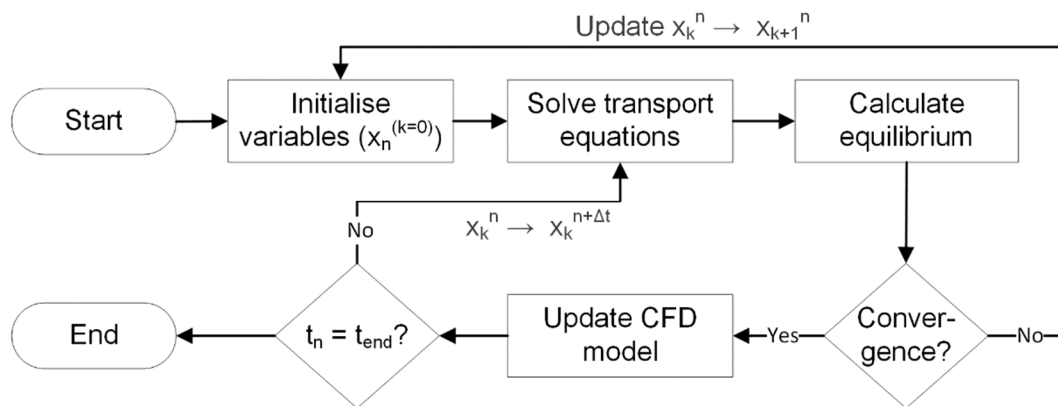

Figure 97:   CFD solution procedure (implicit analysis)

D.3   Turbulence Modelling

The Reynolds-Averaged Navier-Stokes equations are derived based on the assumption that in the turbulent flow regime, a fluid property, ϕ, can be decomposed into its mean (ensemble average for transient problems), $\bar{\phi}$, and fluctuating components, ϕ' [157]:

$$\phi = \bar{\phi} + \phi' \tag{19}$$

Substituting this into the Navier-Stokes equations results in Equation 20 and 21.

$$\frac{\partial \rho}{\partial t} + \partial_i(\rho \bar{u}_i) = 0 \tag{20}$$

$$\frac{\partial \rho \bar{u}_i}{\partial t} + \partial_j(\rho \overline{u_j u_i}) = \rho F_i - \partial_i P + \partial_j(\tau_{ji} + \boldsymbol{T}_t) \tag{21}$$

An additional term, T_t, appears in the momentum equation. This is known as the Reynolds stress tensor and is defined as:

$$\boldsymbol{T}_t = -\rho \begin{bmatrix} \overline{u'u'} & \overline{u'v'} & \overline{u'w'} \\ \overline{u'v'} & \overline{v'v'} & \overline{v'w'} \\ \overline{u'w'} & \overline{v'w'} & \overline{w'w'} \end{bmatrix} \tag{22}$$

The Reynolds stress tensor is modelled using eddy viscosity models.

$$\boldsymbol{T}_t = 2\mu_t \boldsymbol{S} - \frac{2}{3}(\mu_t \nabla \cdot \bar{\mathbf{u}})\boldsymbol{I} \tag{23}$$

$\mu_t = $ turbulent eddy viscosity
$\boldsymbol{S} = $ mean strain rate tensor

The turbulent viscosity is calculated based on the K-Omega (k-ω) model.

$$\mu_t = \rho k T \tag{24}$$

$k = $ turbukent kinetic energy
$T = $ turbulent time scale

The turbulent time scale is a function of the specific dissipation rate, ω. The transport equations for k and ω are defined by the model and are solved to calculate μ_t.

D.4   Wall Treatment

The velocity boundary layer is the layer of fluid adjacent to solid boundaries [31]. The boundary layer can be divided into four regions; 1) viscous sublayer, where the flow is dominated by viscous effects, therefore considered laminar, and the fluid in direct contact with the wall boundary has zero velocity due to the no-slip boundary condition, 2) buffer layer, where viscous effects continue to dominate, 3) overlap layer, where both viscous and turbulent effects dominate and 4) the

turbulent region, where flow is governed by the turbulent effects of the bulk flow. Flow near walls can be solved using the methods summarised in Table 19 [157].

Table 19:   **Various wall treatment methods**

Low y+	The viscous sublayer is solved exactly, which requires a sufficiently fine mesh near the wall. Wall shear stress is calculated as in laminar flows. Valid for $y^+ \approx 1$.
High y+	Wall functions are used to model the viscous sublayer. Coarser meshes are allowed, offering a computational advantage. Valid for $y^+ > 30$.
All y+	Hybrid method that uses low y^+ treatment for fine meshes and high y^+ treatment for coarse meshes.

D.5   Overset Meshes

Overset meshes, or overlapping meshes, are useful for problems with that include motion of solid bodies [157]. The general procedure for overset meshes is summarised as follows:

i.   A background mesh is created, representing the fluid domain.

ii.   A separate mesh, that overlaps the background mesh, is created around a moving body. The overlapping mesh is known as the overset region. Multiple overset regions can be created.

iii.   Coupling between the background region and the overset region is defined by an overset mesh interface boundary condition. Coupling is also specified for overlapping overset regions. For effective coupling between regions and to reduce interpolation errors, the cells in the overlapping regions must be the same size at the overset boundary.

Cells in the background and overset meshes are classified as either active, inactive, donor or acceptor. The governing algebraic equations are solved normally for active cells in each region. The inactive cells do not take part in the simulation. The inactive cells are identified as the cells in the background region with cell centroids overlapped by the overset region. For a problem that includes motion, the active and inactive cells at each time step will change as the overset region moves. Therefore, it is more suitable to view the inactive cells as passive cells.

The acceptor cells separate the background's inactive cells from the active cells, which forms a boundary around the overlapping region. The donor cells surround the overset region's active cells. The exchange of information occurs between the acceptor and donor cells. The donor cells provide data from the overset region to be transferred to the background region. The acceptor cells in the background region receive information from the nearby donor cells. The contribution of each donor cell to an acceptor cell is dependent on the interpolation method. The process is reversed to transfer information from the background region to the overset region. For this study, linear interpolation shape functions were selected to determine the donor cells for each acceptor cell.

Figure 98 shows a planar view of the CFD model at t = 0 s. The background region models the majority of the fluid domain and is representative of the experimental test setup. A separate overset region encloses each leaflet. The same motion condition is specified for each overset-leaflet pair; therefore, the overset region rotates with the leaflet.
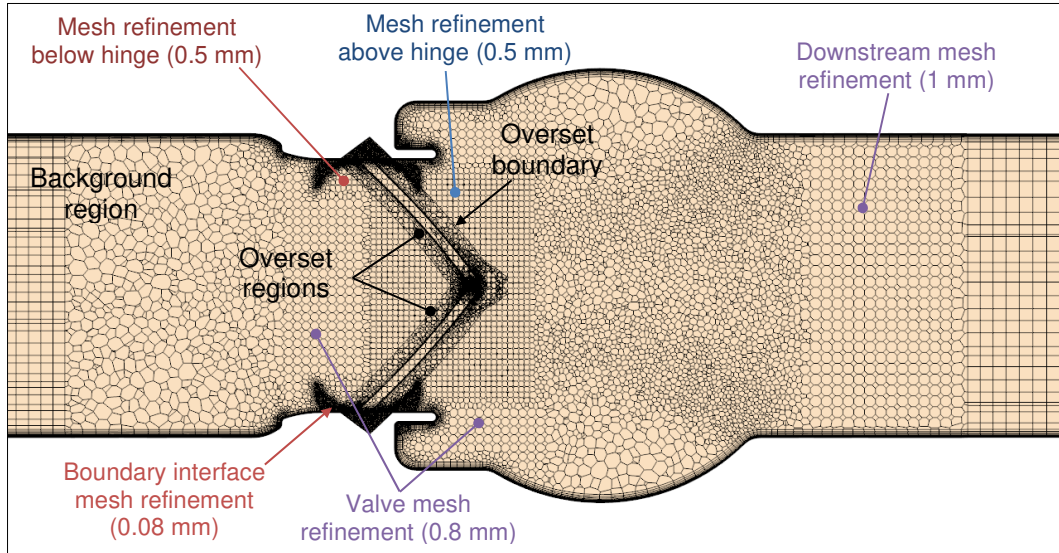

Figure 98: **CFD model showing the overlapping meshes on the YZ plane**

Each region is distinguished in Figure 99 (YZ planar view). The overlapping meshes are shown in Figure 99a. The overset regions overlap the background region as well as the other overset regions. Once the overset condition is activated, the volume mesh is created, which is shown in Figure 99b. The coupling boundary between each region is established and the inactive cells are not displayed.

| (a) Overset mesh | (b) Volume mesh |
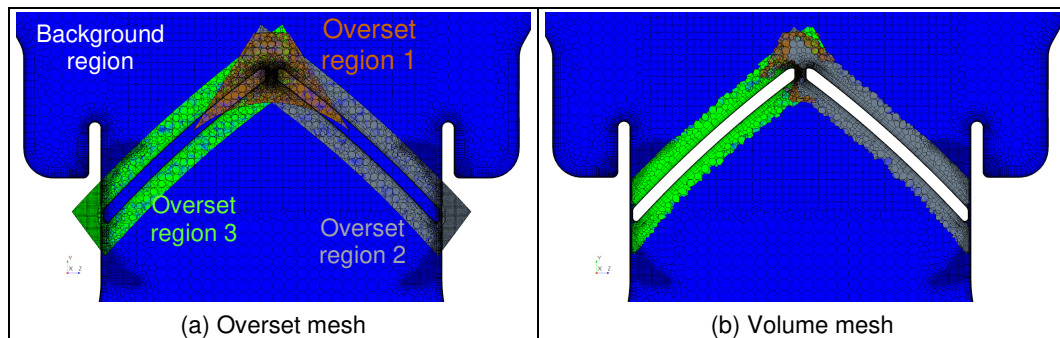
Figure 99: **Background and overset regions**

Figure 100 and Figure 101 show the cell types of the background and overset regions. Green, blue and red indicate active, communicator and inactive cells respectively. The communicator cells either donate or accept information, to or from overlapping regions.
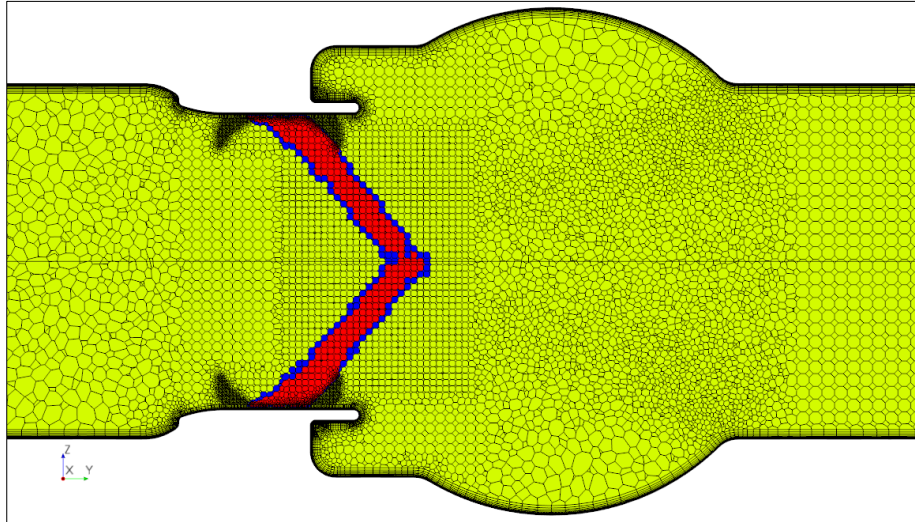
Figure 100:   Cell status of the background region

In Figure 101, all three overset regions are shown. Each region has its own active, inactive and communicator cells. The communicator cells exchange information with the background region as well as the other overset regions, forming multiple coupling boundaries. Visualisation of the individual overset regions is challenging due to the overlapping of the regions.
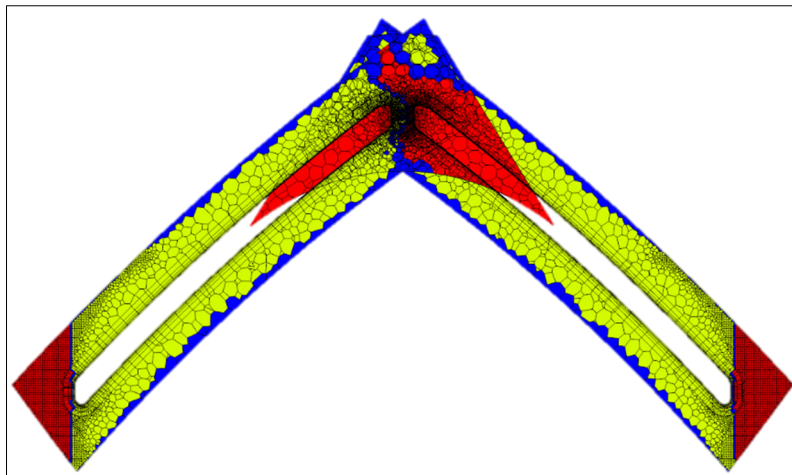

Figure 101:   Cell status of the overlapping overset regions

Appendix E   NUMERICAL EVALUATION

E.1   Mesh Independence Study

Following the same approach as in [33], the mesh convergence study was conducted at peak systole, with steady state conditions and stationary leaflets (fully open position). The mesh density was varied, as listed in Table 20, and the effect on certain flow parameters was analysed.

Table 20:   **Mesh specifications of the mesh independence study**

Mesh property	Mesh size				
	Very coarse	Coarse	Inter-mediate	Fine	Very fine
Base cell size [mm]	2	1.4	1.2	1	0.8
Number of cells	2 403 746	3 743 865	4 450 897	5 330 743	6 116 242

The parameters of interest that were monitored are maximum velocity in the flow field and pressure drop (from 30 mm upstream to 85 mm downstream of the valve). The results of the mesh independence study are plotted in Figure 102.
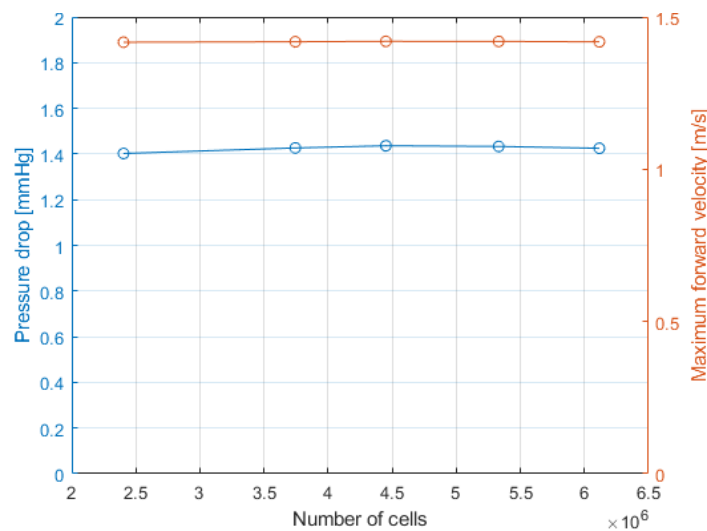
Figure 102:   **Results of the mesh independence study**

Based on the outcome of the mesh independence study, the intermediate mesh with a 1.2 mm base size was selected. The mesh properties are listed in Table 21. The values apply to the 40° trileaflet valve at 90° open. The same mesh properties were applied to the other cases, although the total cell count differed based on the valve configuration.

Table 21:   Steady state CFD mesh properties

Mesh property	Upstream region	Valve refinement region	Downstream refinement region	Downstream region
Maximum cell size [mm]	1.2	0.6	1	1.2
No. of prism layers	10	10	10	10
Total prism layer thickness [mm]	0.75	0.4	0.75	0.75
Thickness of near-wall prism layer [mm]	0.04	0.0125 (housing) 0.009 (leaflets)	0.04	0.04
Mesh extrusion properties [mm]	140 (average cell size 1.87)	-	-	50 (average cell size 1.43)

E.2   Steady State Simulation Results

Figure 103 shows the velocity magnitude streamlines and contour plots at 8 mm and 30 mm downstream at various open positions.
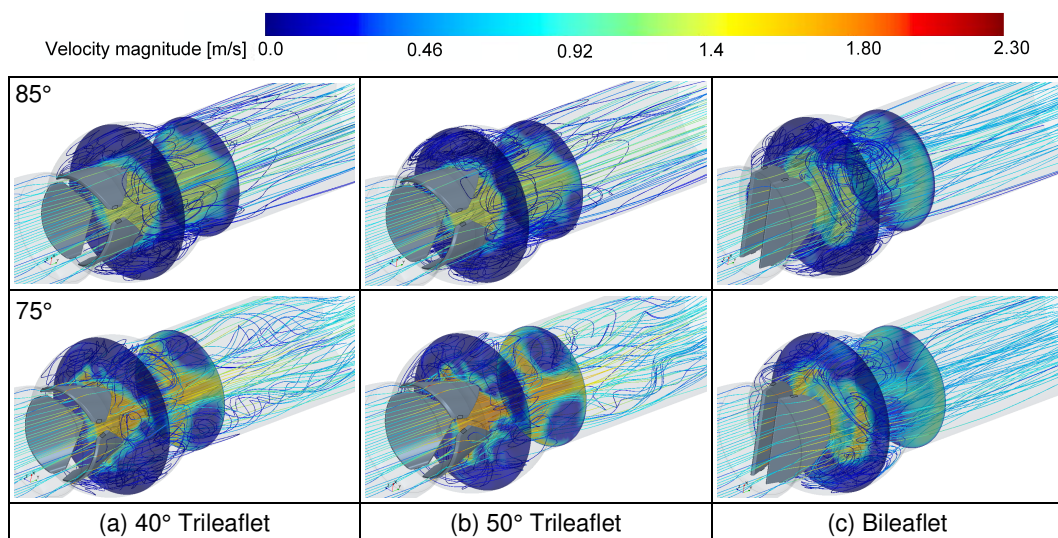
Figure 103:   Steady state velocity results at various open angles (2)

The maximum housing and leaflet WSS at various open positions is displayed in Figure 104.
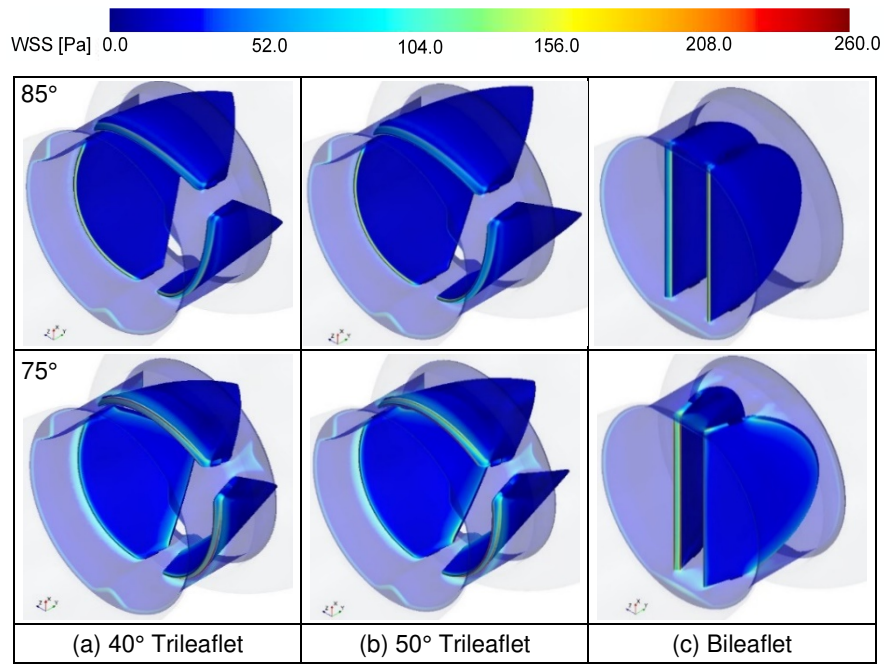
Figure 104: WSS results at various open angles (2)

Velocity profiles of the 85° and 75° open positions are shown in Figure 105 and Figure 106 respectively.
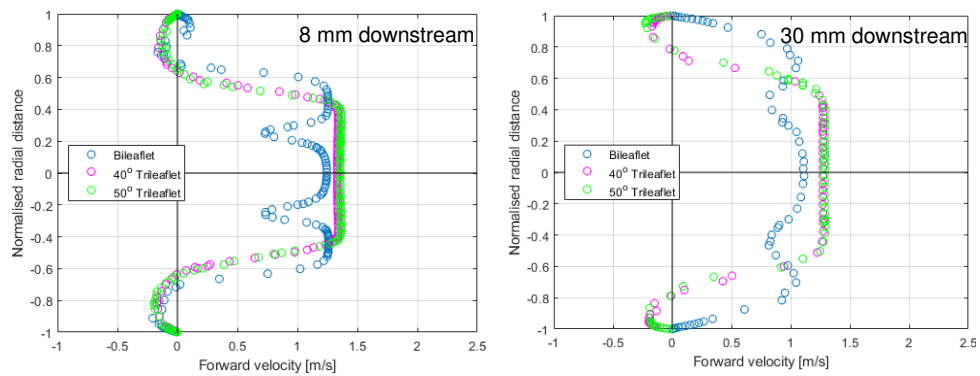
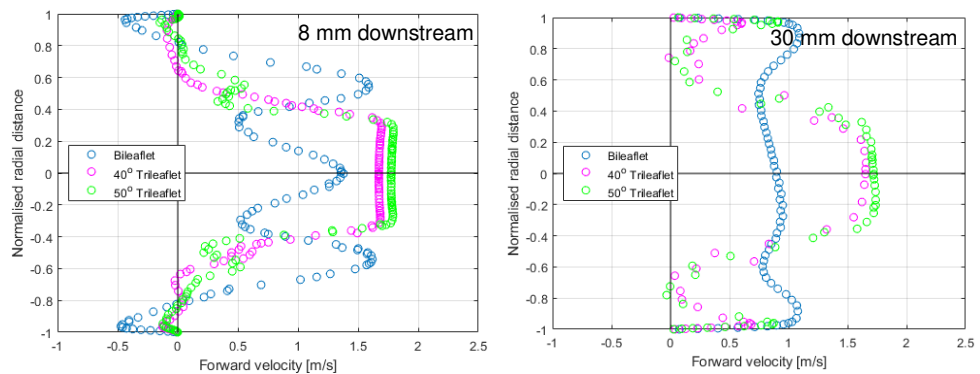**Figure 105: Downstream velocity profile at 85° open**

Figure 106: Downstream velocity profile at 75° open

The vorticity magnitude on a longitudinal plane of the valves for various open angles are shown in Figure 107. Figure 108 shows the total pressure on a longitudinal plane at various open angles.
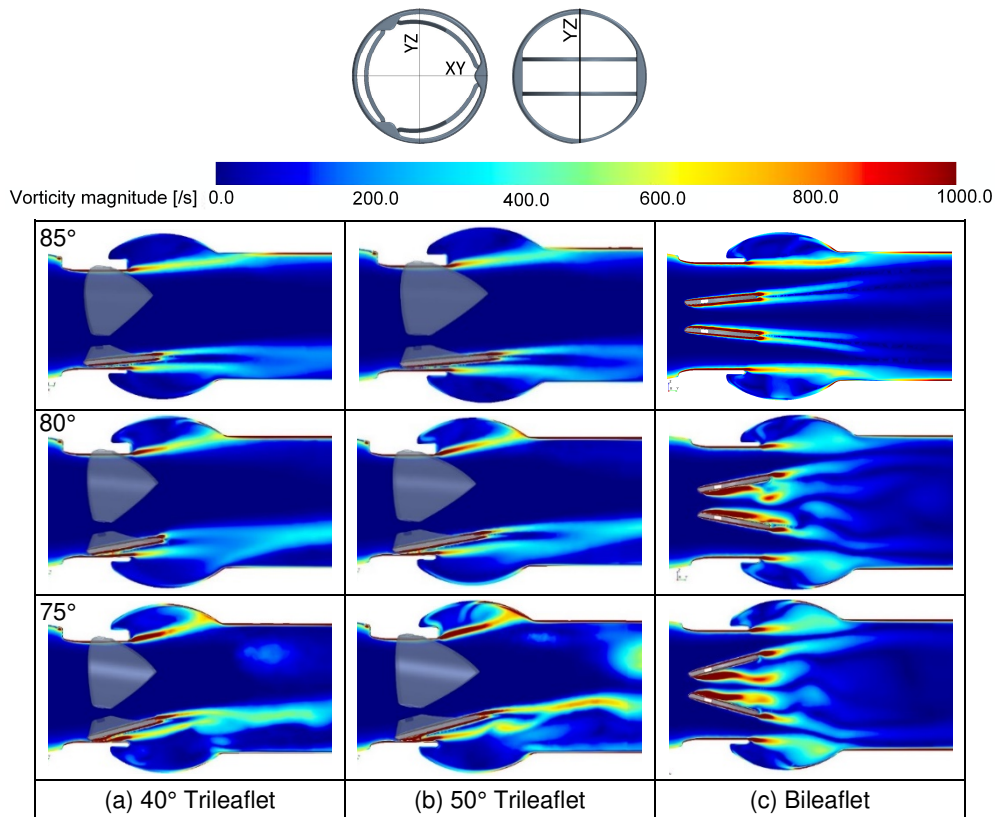

Figure 107: **Vorticity results at various open angles (2)**
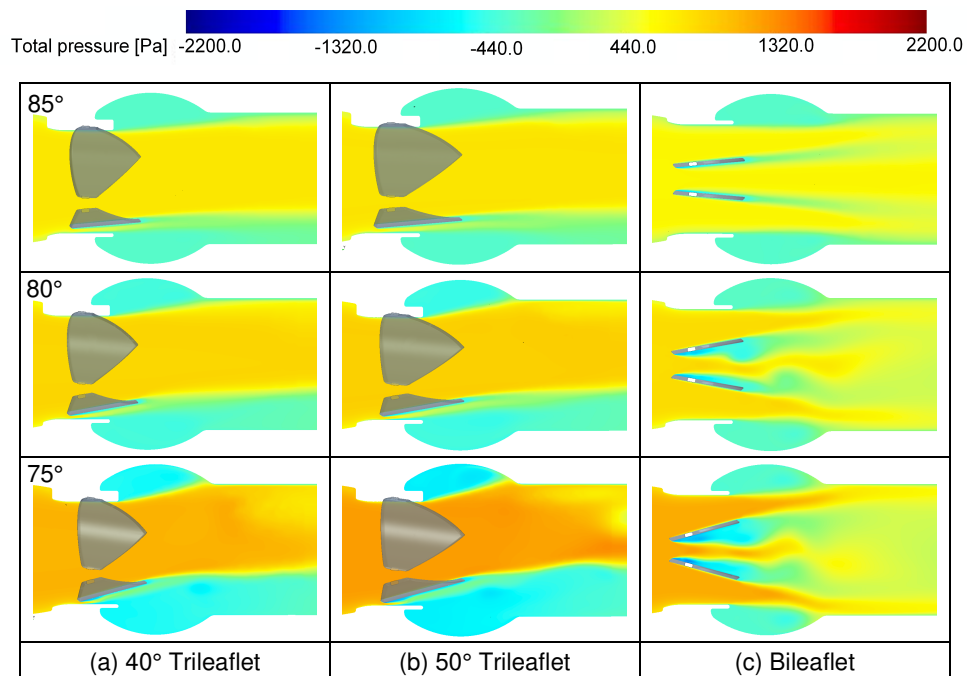
Figure 108: **Pressure results at various open angles (2)**

E.3   LES Mesh Requirements

The results from the steady state open and closed analyses were used to get an indication of the surface cell size requirements to perform a LES analysis, where large-scale eddies are solved and small-scale eddies are modelled. The Kolmogorov length scale represents the smallest energy dissipating eddies in turbulent flow [30, 115, 157]. The Taylor microscale is representative of the intermediate-sized eddies [32, 93, 157]. Creating a mesh where the average cell size is larger than the Kolmogorov length scale yet smaller than the Taylor microscale, should result in a sufficiently refined mesh for a LES analysis [157], at least as a first order approach. Figure 109 displays the Taylor microscale on the wall surfaces in the fully open and fully closed positions for the 40° trileaflet 1 valve. The results indicate that the maximum LES mesh requirements over the full cardiac cycle range between 1.4 – 24 µm.
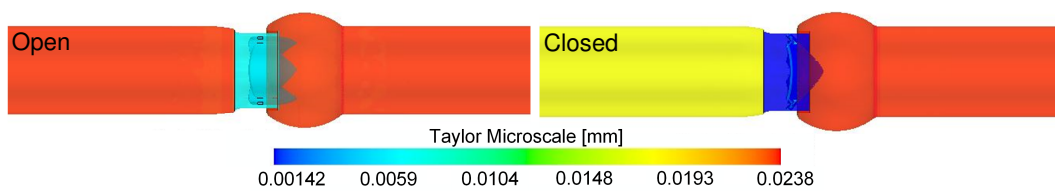

Figure 109:   Taylor microscale of the open and closed CFD models

To determine the feasibility of solving the problem using LES, a mesh based on the Taylor microscale was created. However, the minimum cell size was still an order of magnitude larger than required. The following modifications were made to the mesh settings as previously defined for the steady state simulations:

- Surface mesh refinement of 0.01 mm in the housing region and a surface mesh refinement of 0.05 mm in the upstream and downstream regions. The refinement regions are indicated in Figure 110.

- Overall prism layer height of 2 mm with a 0.03 mm near-wall cell. Custom prism layer settings for leaflets remained unchanged.

- Base cell size of 1 mm.

- Upstream and downstream mesh extrusion parameters were adjusted to include more cell layers so that the cells have an aspect ratio of approximately one.
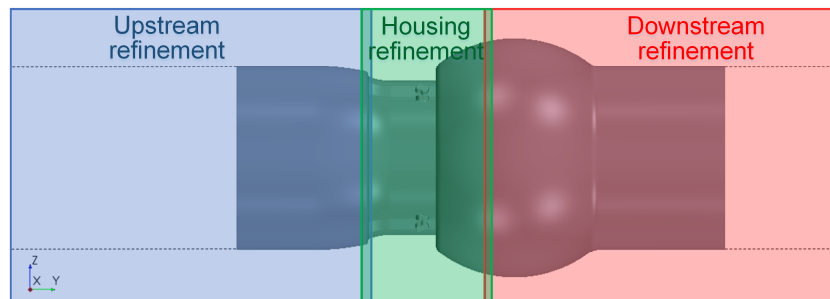

Figure 110:   LES mesh refinement regions

The LES mesh was generated using ten nodes at the CHPC. The hardware is the same as previously described. It took just over four hours to create the LES mesh, which had a total of 110 898 716 cells. These mesh conditions are larger than the Taylor microscale specifications, so to conduct a LES analysis, even more cells will be required. The model did not include overset mesh regions to accommodate leaflet motion, which will further increase the total cell count. Based on this, it was concluded that LES is not currently a feasible method to solve the problem.

E.4   Prescribed Motion Simulations

The prescribed kinematics CFD model's mesh specifications are listed in Table 22.

Table 22:   Prescribed motion CFD mesh properties

Mesh property	Upstream region	Valve refinement region	Downstream refinement region	Downstream region
Maximum cell size [mm]	1.2	0.8	1.0	1.2
No. of prism layers	10	10	10	10
Total prism layer thickness [mm]	0.75	0.4	0.75	0.75
Thickness of near-wall prism layer [mm]	0.03	0.0025 (housing) 0.000125 (leaflets)	0.018	0.018
Mesh extrusion properties [mm]	140 (average cell size 1.87)	-	-	60 (average cell size 1.62)

The maximum velocity magnitude of the fluid is plotted in Figure 111. The results confirm that the solution was periodically stable. Figure 112 and Figure 113 show the velocity and RSS results at various time points during the cardiac cycle.
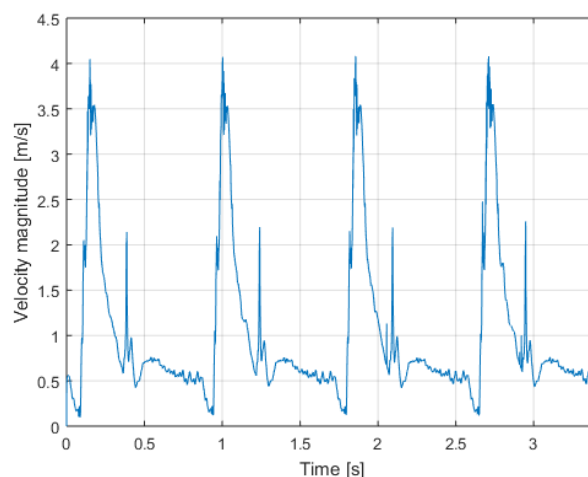

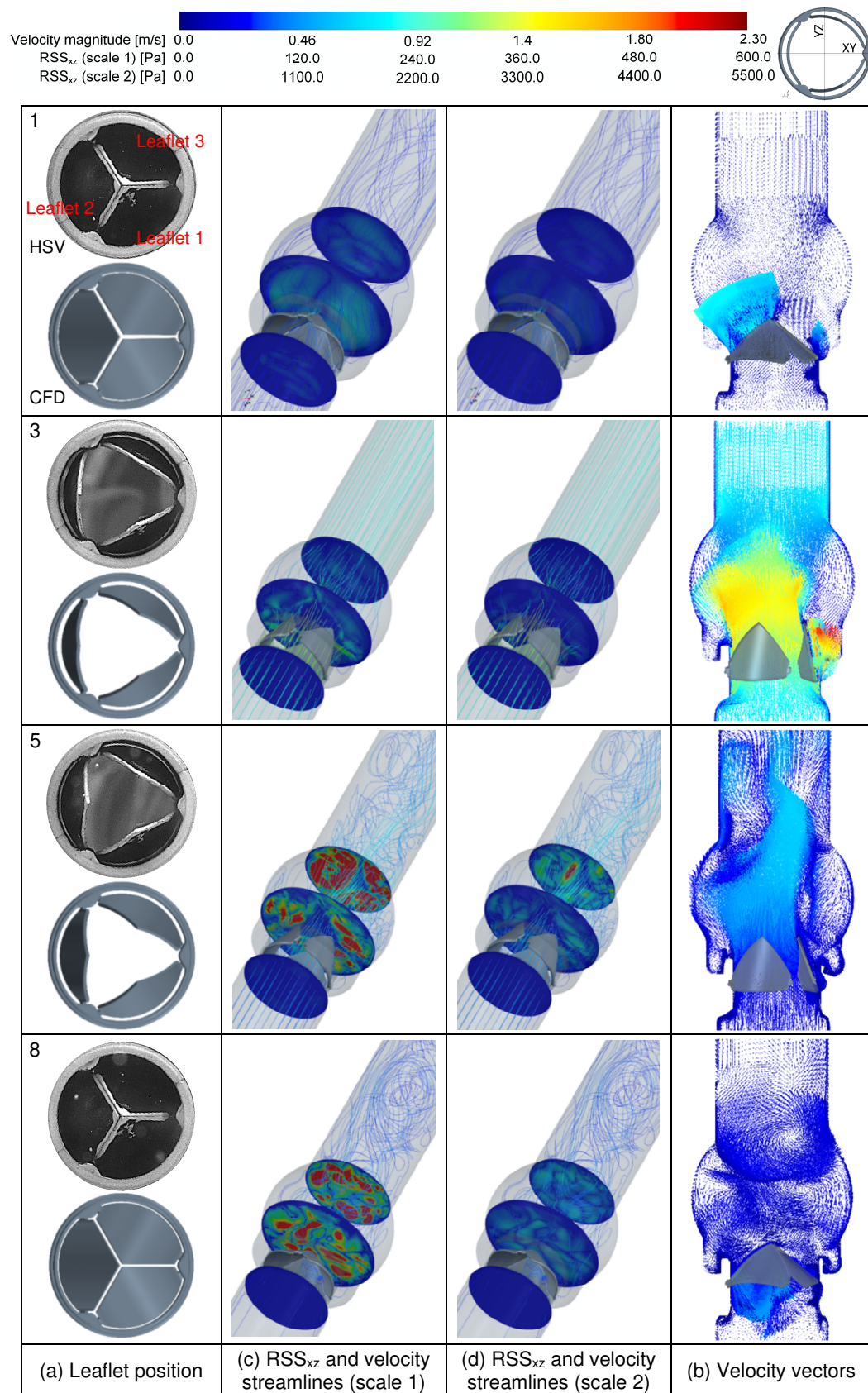**Figure 111:   Velocity magnitude over four cardiac cycles**

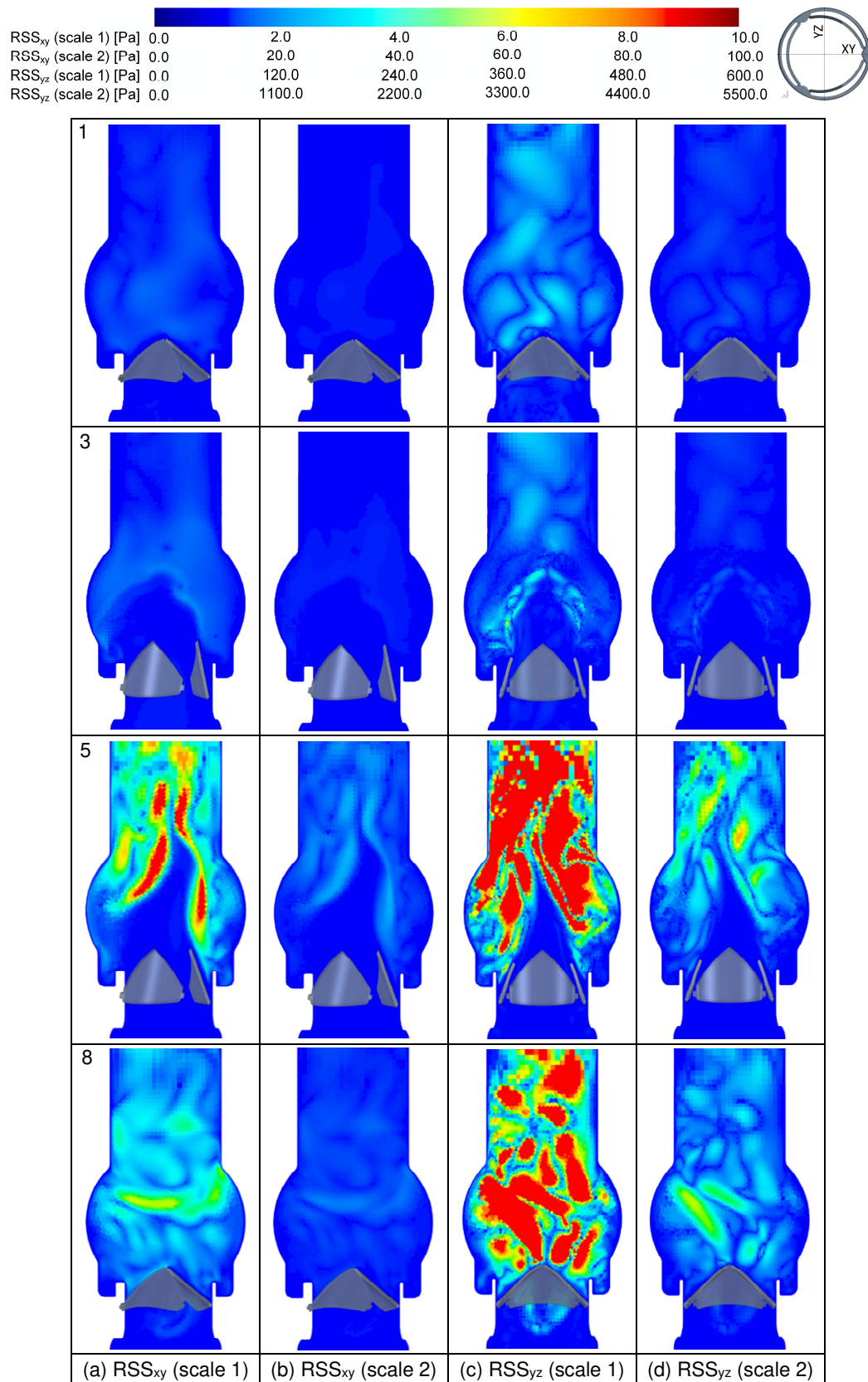Figure 112:   Leaflet position, velocity and maximum RSS$_{xz}$ CFD results (2)

Figure 113: Maximum RSS_xy and RSS_yz CFD results (2)

The pressure results on the YZ plane and the velocity results on the XY plane are presented in Figure 114 and Figure 115 respectively.
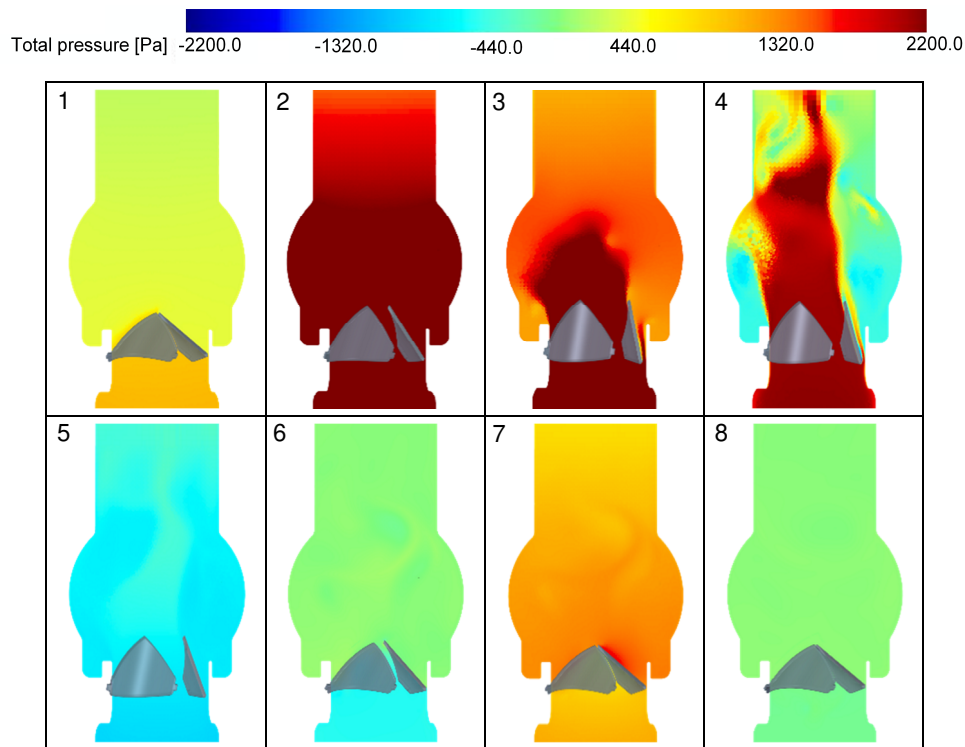

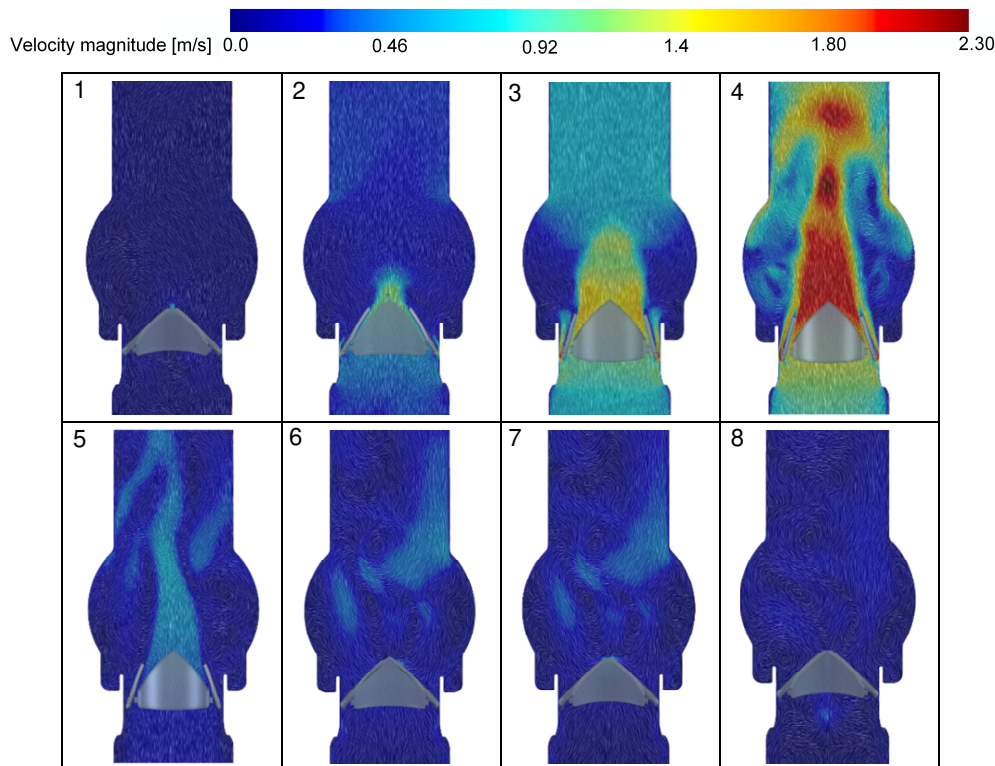**Figure 114:   Pressure field on the ZY plane over one cardiac cycle**

Figure 115:   Velocity field on the XY plane over one cardiac cycle